UNIVERSITÀ
DEGLI STUDI
DI TRIESTE

UNIVERSITÀ DEGLI STUDI DI TRIESTE

XXXVIII CICLO DEL DOTTORATO DI RICERCA IN

PhD Nanotechnology

Development and Characterization of Polycaprolactone Scaffolds Functionalized with Nano-Hydroxyapatite to Enhance Osteogenic Potential

Settore scientifico-disciplinare: ___**MED/28**_____

DOTTORANDO
ALVISE CAMURRI PILONI

COORDINATORE
PROF. ALBERTO MORGANTE

SUPERVISORE DI TESI
PROF. VANESSA NICOLIN

CO-SUPERVISORE DI TESI
PROF. GIANLUCA TURCO

CO-SUPERVISORE DI TESI
PROF. GIULIO MARCHESI

ANNO ACCADEMICO 2024/2025

UNIVERSITÀ
DEGLI STUDI
DI TRIESTE

UNIVERSITÀ DEGLI STUDI DI TRIESTE

XXXVIII CICLO DEL DOTTORATO DI RICERCA IN

PhD Nanotechnology

Development and Characterization of Polycaprolactone Scaffolds Functionalized with Nano-Hydroxyapatite to Enhance Osteogenic Potential

Settore scientifico-disciplinare: ___**MED/28**_____

DOTTORANDO
ALVISE CAMURRI PILONI

COORDINATORE
PROF. ALBERTO MORGANTE

SUPERVISORE DI TESI
PROF. VANESSA NICOLIN

CO-SUPERVISORE DI TESI
PROF. GIANLUCA TURCO

CO-SUPERVISORE DI TESI
PROF. GIULIO MARCHESI

ANNO ACCADEMICO 2024/2025

Table of Contents

Sommario

ABSTRACT

Nanotechnology has revolutionized the field of regenerative medicine, enabling the creation of biomaterials capable of interacting with living tissues at the molecular and cellular level. Within this framework, bone tissue engineering has emerged as one of the most promising applications, offering innovative alternatives to traditional grafts for the repair of complex bone defects. The present doctoral research aimed to develop, characterize, and biologically validate a new generation of bioactive scaffolds based on polycaprolactone (PCL), functionalized with nano-hydroxyapatite (nHAp) and further modified through plasma activation, ultraviolet (UV) crosslinking, and silver (Ag) doping to enhance osteogenic and antibacterial potential.

The study employed a multidisciplinary workflow integrating materials science, nanotechnology, and biological evaluation. PCL scaffolds were fabricated via Fused Deposition Modeling (FDM) using a controlled lattice design to ensure uniform porosity and mechanical integrity. Plasma surface activation introduced polar functional groups that significantly improved surface hydrophilicity, while subsequent coating with nHAp enabled nanoscale mineralization mimicking the inorganic phase of bone. UV irradiation promoted interfacial stability through photochemical crosslinking, and silver ion doping imparted controlled antibacterial functionality. The resulting hierarchical surface architecture was analyzed through a comprehensive suite of morphological, chemical, mechanical, and thermal techniques, including Scanning Electron Microscopy (SEM), Atomic Force Microscopy (AFM), Energy Dispersive X-ray Spectroscopy (EDS), Fourier Transform Infrared Spectroscopy (FTIR), Differential Scanning Calorimetry (DSC), and Thermogravimetric Analysis (TGA). Finite Element Modeling (FEM) further validated mechanical performance under simulated loading conditions.

Experimental results demonstrated that plasma and nHAp functionalization markedly increased surface roughness, surface energy, and Ca/P stability, promoting enhanced protein adsorption and cell anchorage. Mechanical analyses confirmed the structural reliability of the scaffolds after six months of aging in aqueous and simulated body environments, with stable or slightly improved elastic modulus due to secondary crystallization. Thermal and spectroscopic data validated the chemical stability and homogeneous integration of the nano-coating. Biological assays using human MG63 osteoblast-like cells, murine 3T3 fibroblasts, and MC3T3-E1 pre-osteoblasts confirmed the biocompatibility and osteoconductive nature of the scaffolds, while silver-doped composites exhibited potent antibacterial efficacy without cytotoxic effects.

The overall findings highlight the success of a multi-step nanoscale functionalization strategy that transforms a bioinert polymer into a bioactive, osteoconductive, and antimicrobial platform suitable for bone regeneration. By bridging nanostructural design with cellular response, this research contributes to the development of clinically translatable scaffolds for oral and maxillofacial surgery, where infection control and rapid osteointegration are critical. The study underscores how nano-engineering, surface chemistry, and additive manufacturing can converge to create the next generation of intelligent biomaterials for regenerative medicine.

Keywords: nano-hydroxyapatite, nano-engineered scaffold, nano-surface modification, plasma treatment, polycaprolactone, bone tissue engineering, osteogenic potential, antibacterial activity

List of Abbreviations

AFM	Atomic Force Microscopy
Ag–nHAp	Silver-doped Nano-Hydroxyapatite
ALP	Alkaline Phosphatase
ANOVA	Analysis of Variance
ASTM	American Society for Testing and Materials
ATR	Attenuated Total Reflectance
BIC	Bone-to-Implant Contact
BMP	Bone Morphogenetic Protein
CAD	Computer-Aided Design
Ca/P	Calcium-to-Phosphorus Ratio
CFU	Colony Forming Units
CLSI	Clinical and Laboratory Standards Institute
COL1A1	Collagen Type I Alpha 1
CPP	Critical Process Parameters
CQA	Critical Quality Attributes
DMSO	Dimethyl Sulfoxide
DMEM	Dulbecco's Modified Eagle Medium
DNA	Deoxyribonucleic Acid
DSC	Differential Scanning Calorimetry
ECM	Extracellular Matrix
EDS	Energy Dispersive X-ray Spectroscopy
FDM	Fused Deposition Modeling
FAK	Focal Adhesion Kinase
FEM	Finite Element Modeling
FBS	Fetal Bovine Serum
GBR	Guided Bone Regeneration
GMP	Good Manufacturing Practice
HAp	Hydroxyapatite
ICP-OES	Inductively Coupled Plasma Optical Emission Spectroscopy
ISO	International Organization for Standardization
MC3T3-E1	Murine Calvarial Pre-Osteoblast Cell Line
MBC	Minimum Bactericidal Concentration
MIC	Minimum Inhibitory Concentration
MG63	Human Osteoblast-like Cell Line
MTT	3-(4,5-Dimethylthiazol-2-yl)-2,5-Diphenyltetrazolium Bromide
nHAp	Nano-Hydroxyapatite
OCN	Osteocalcin
PCL	Poly(ε-caprolactone)
PLA	Polylactic Acid
PO_4^{3-}	Phosphate Ion

QbD	Quality by Design
ROS	Reactive Oxygen Species
RUNX2	Runt-related Transcription Factor 2
Sa, Sq, Ssk	Surface Roughness Parameters (Areal Roughness, RMS Height, Skewness)
SBF	Simulated Body Fluid
SEM	Scanning Electron Microscopy
Sr/Zn	Strontium / Zinc (dopants)
TGA	Thermogravimetric Analysis
T_m	Melting Temperature
T_{onset}	Onset Degradation Temperature
UV	Ultraviolet
VEGF	Vascular Endothelial Growth Factor
YAP/TAZ	Yes-Associated Protein / Transcriptional Co-Activator with PDZ-Binding Motif

List of Figures

List of Tables

List of Equations

CHAPTER 1 – INTRODUCTION AND RESEARCH OBJECTIVES

1 Overview

Advances in nanotechnology and material science have profoundly transformed the landscape of regenerative medicine, introducing the possibility of designing biomaterials that not only replace damaged tissue but actively stimulate its regeneration. Bone tissue engineering (BTE) stands at the forefront of this evolution, addressing one of the most critical challenges in oral and maxillofacial surgery: the restoration of bone defects that exceed the body's natural healing capacity.

Within this context, the development of bioactive, biodegradable, and mechanically reliable scaffolds has become central to the progress of regenerative strategies. The convergence of additive manufacturing (AM), nanostructured materials, and surface modification techniques enables the creation of highly customized three-dimensional constructs that mimic both the architecture and biochemical functionality of native bone.

The present research focused on the development and characterization of polycaprolactone (PCL) scaffolds functionalized with nano-hydroxyapatite (nHAp), further enhanced through plasma activation, ultraviolet (UV) crosslinking, and silver (Ag) doping. This integrated approach sought to optimize the mechanical stability, bioactivity, and antibacterial functionality of the scaffolds to create a clinically translatable platform for bone regeneration in the cranio-maxillofacial field.

1.1 Bone Tissue Engineering and Regenerative Medicine

Bone tissue engineering (BTE) is an interdisciplinary field combining biology, materials science, and engineering principles to restore or regenerate bone tissue through the use of scaffolds, cells, and signaling molecules. [1] Since its emergence in the late 1980s, the field has evolved beyond the concept of structural replacement, embracing biomaterials that act as active participants in the healing process. [2]

Autologous bone grafting remains the clinical gold standard due to its osteogenic, osteoinductive, and osteoconductive properties. However, it suffers from well-known drawbacks such as donor-site morbidity, infection risk, limited graft volume, and unpredictable resorption rates [3]. Synthetic and allogenic substitutes can partially overcome these limitations, but they often lack the biological cues necessary for full osteointegration.

The cornerstone of BTE lies in the triad of cells, scaffolds, and signaling molecules, which collectively create an environment conducive to new tissue formation. The scaffold provides the three-dimensional extracellular matrix (ECM)-like structure that supports cellular adhesion, migration, proliferation, and differentiation. [4] For bone regeneration, this architecture must replicate the hierarchical composite nature of bone, which consists of an organic collagenous matrix (30–35 wt%) reinforced by an inorganic mineral phase of hydroxyapatite (60–70 wt%) that provides mechanical stiffness. [5]

An ideal scaffold must therefore exhibit biocompatibility, mechanical strength, interconnected porosity, osteoconductivity, and controlled biodegradability, aligning its degradation rate with new bone formation. [6] In addition, vascularization within the scaffold is essential for nutrient delivery and waste removal, ensuring long-term integration and tissue viability. [7]

Recent progress in bio fabrication and nanotechnology has enabled the design of scaffolds that reproduce bone's structural and chemical complexity at multiple scales. Incorporating nanostructured features and bioactive agents such as bone morphogenetic proteins (BMPs) and vascular endothelial growth factors (VEGF) enhances both osteogenesis and angiogenesis. [8] Consequently, bone tissue engineering is increasingly viewed as a viable and customizable alternative to traditional grafting procedures for oral, craniofacial, and orthopedic reconstruction. [9]

1.2 Additive Manufacturing and FDM Technology in Scaffold Fabrication

Additive manufacturing (AM), or three-dimensional (3D) printing, has revolutionized the fabrication of biomedical scaffolds, allowing precise control over geometry, porosity, and internal architecture. [10] Among various AM techniques—such as stereolithography (SLA), selective laser sintering (SLS), and bioprinting—Fused Deposition Modeling (FDM) stands out for its accessibility, cost-effectiveness, and reproducibility. [11]

FDM operates by extruding a thermoplastic polymer through a heated nozzle, depositing material layer by layer according to a computer-aided design (CAD) model. This digital workflow—from medical imaging data to final printed construct—enables patient-specific scaffold fabrication tailored to complex bone geometries. [12]

Control over printing parameters, including filament diameter, infill pattern, and layer orientation, directly influences mechanical strength, porosity, and cellular response. [13] Optimal pore sizes between 300 and 600 μm promote osteoblast adhesion, nutrient transport, and vascular ingrowth. [14]

Furthermore, AM technology allows for the integration of multimaterial systems, combining structural polymers with bioactive ceramics to replicate bone's biphasic composition.

Despite these advantages, FDM is limited by the range of printable biomaterials and its relatively high processing temperatures, which preclude the incorporation of living cells or heat-sensitive molecules. [15] To overcome these limitations, post-processing strategies such as plasma surface modification, chemical activation, and mineral coating have been introduced to enhance the bioactivity of printed scaffolds. [16]

The ability to precisely tune both macro and nanoscale architecture makes FDM an essential tool for next-generation scaffold engineering, bridging digital design and biological performance. [17]

1.3 Polycaprolactone (PCL) as a Biodegradable Matrix

Polycaprolactone (PCL) is a biodegradable aliphatic polyester widely recognized for its biocompatibility, processability, and mechanical flexibility. [18] Synthesized by the ring-opening polymerization of ε-caprolactone, PCL exhibits a semi-crystalline structure with a low melting temperature (~60°C) and a glass transition temperature around −60°C, making it ideal for FDM-based processing. [19]

Its slow degradation rate—ranging from months to several years depending on molecular weight and crystallinity—allows for sustained mechanical support during tissue regeneration. [20] PCL degrades primarily via hydrolysis of its ester bonds, producing 6-hydroxycaproic acid, which is metabolized through normal physiological pathways without causing acidic by-products or inflammatory responses. [21] Mechanically, PCL demonstrates a Young's modulus of 200–400 MPa and a tensile strength between 10–20 MPa, with high elongation at break (>300%), providing ductility suitable for non-load-bearing bone applications. [22] However, its hydrophobic and bioinert nature limits cell adhesion and protein adsorption. Therefore, surface modification techniques—such as plasma treatment, alkaline hydrolysis, and coating with collagen or hydroxyapatite—are commonly applied to improve biological performance. [23]

Plasma activation introduces oxygen-containing functional groups (–OH, –COOH) that enhance wettability and facilitate subsequent chemical bonding with bioactive coatings like nano-hydroxyapatite. [24] These treatments effectively convert an inert polymer surface into a reactive template capable of supporting osteoblast adhesion and differentiation. [25]

Furthermore, PCL has been approved by the U.S. Food and Drug Administration (FDA) for multiple biomedical uses, including sutures and drug-delivery systems, confirming its clinical safety and translational potential. [26]

1.4 Nano-Hydroxyapatite (nHAp) as an Osteogenic Reinforcement

Hydroxyapatite (HAp), with the chemical formula $Ca_{10}(PO_4)_6(OH)_2$, represents the principal inorganic component of bone, conferring rigidity and bioactivity. [27] When reduced to the nanoscale, nano-hydroxyapatite (nHAp) exhibits enhanced surface reactivity and greater similarity to biological apatite, making it a powerful osteogenic reinforcement for polymeric scaffolds. [28]

nHAp provides excellent osteoconductivity and bioactivity, stimulating apatite formation in simulated body fluid (SBF) and promoting osteoblastic differentiation through upregulation of key markers such as alkaline phosphatase (ALP), osteocalcin (OCN), and osteopontin (OPN). [29] Its high surface-to-volume ratio enhances protein adsorption and cellular interaction, essential for effective bone regeneration. [30]

In composite scaffolds, nHAp improves mechanical strength and elastic modulus, achieving values closer to cancellous bone (100–500 MPa) while maintaining biocompatibility. [31] The homogeneous distribution of nanoparticles across the polymer matrix is critical to avoid agglomeration and stress concentration, which can compromise both structural integrity and biological response. [32]

Surface-localized mineralization—achieved through dip-coating or plasma-assisted deposition—allows for targeted bioactivity without altering the bulk mechanical properties of the polymer. [33] PCL/nHAp scaffolds fabricated via FDM and subsequent mineral coating have consistently demonstrated superior osteoconductive behavior compared to unmodified PCL. [34]

Through this synergistic interaction between polymeric flexibility and nanoscale mineral reinforcement, nHAp effectively bridges the gap between mechanical performance and biological functionality, serving as the cornerstone of the material strategy employed in this research.

1.5 Surface Modification through Plasma Treatment

Although polycaprolactone (PCL) exhibits excellent processability, mechanical reliability, and biocompatibility, its intrinsic hydrophobic nature and chemical inertness significantly limit early protein adsorption and cell adhesion—two key prerequisites for successful osteointegration. [35] To address these shortcomings, plasma surface modification has emerged as one of the most effective,

controllable, and solvent-free strategies for improving polymer surface chemistry while preserving the bulk mechanical properties. [36]

Plasma treatment operates by exposing the polymer surface to a partially ionized gas, typically containing electrons, ions, and reactive radicals, which interact with the outermost molecular layers of the material. These high-energy species break C–H and C–C bonds at the surface, generating reactive radicals and introducing polar functional groups such as hydroxyl (–OH), carbonyl (–C=O), and carboxyl (–COOH). [37] The incorporation of these oxygen-containing moieties markedly increases the surface free energy and, consequently, the wettability of the material.

The degree of modification depends strongly on the discharge power, exposure time, type of gas, and chamber pressure. [38]

Plasma-induced modification not only alters the chemical composition of the surface but also subtly affects its topography, creating nanoscale roughness that provides additional anchorage points for cell adhesion. [39] As previously reported, such nanoscale irregularities enhance integrin clustering and focal adhesion formation, leading to improved cytoskeletal organization and spreading of osteoblast-like cells. [40] Moreover, the presence of polar groups on the activated surface improves protein adsorption, particularly for fibronectin, collagen type I, and vitronectin—key extracellular matrix components that mediate cell–substrate interactions. [41]

The dual-step modification (plasma activation followed by mineral coating) produced a surface combining chemical reactivity and nanoscale topographical complexity. This hierarchical configuration enables synergistic improvement in hydrophilicity and bioactivity

Several studies have demonstrated that such plasma-assisted mineralization significantly improves cell adhesion, proliferation, and differentiation of osteogenic lineages. [42–44] The presence of bioactive hydroxyl and phosphate groups facilitates ionic exchange with the surrounding environment, accelerating biomimetic mineralization and enhancing osteoblast metabolic activity. In particular, the combination of increased surface energy and the bioactive chemistry of nHAp establishes an environment that supports strong and stable bonding between cells and the scaffold.

1.6 Scientific Rationale and Research Gap

The continuous evolution of biomaterials science and additive manufacturing has significantly advanced bone tissue engineering; however, several persistent limitations hinder the clinical translation of polymer–ceramic composite scaffolds. [45] Although polymer-based systems offer the

advantages of flexibility, biodegradability, and tunable mechanics, they often lack bioactivity and interfacial strength when combined with inorganic fillers. Conversely, ceramic materials such as hydroxyapatite (HAp) or tricalcium phosphate (TCP) provide excellent osteoconductivity but suffer from brittleness and poor mechanical resilience. Achieving an optimal balance between mechanical stability, bioactivity, and degradation kinetics therefore remains a major challenge in scaffold design. [46]

Traditional fabrication methods—such as solvent casting, particulate leaching, or electrospinning—have been extensively explored for creating composite scaffolds, but they inherently suffer from several drawbacks. Solvent-based approaches often leave toxic residues that can interfere with cell behavior, while electrospinning, though capable of producing nanofibrous matrices, is limited in its ability to generate volumetric scaffolds suitable for repairing large bone defects. [47] Moreover, these methods offer limited control over pore geometry, interconnectivity, and mechanical uniformity, which are crucial parameters influencing cellular infiltration and nutrient diffusion. As a result, most existing scaffolds exhibit either sufficient structural stability but poor biological performance, or good bioactivity but insufficient load-bearing capacity.

To address these issues, the present research was conceived as an integrated and multidisciplinary approach that bridges computational modeling, advanced manufacturing, and nanoscale surface functionalization. The rationale was to engineer a scaffold that replicates not only the macroscopic geometry of cancellous bone but also its nanoscale biochemical cues, creating a system capable of directing osteogenesis from the molecular to the structural level.

The strategy involved two synergistic stages:

1. Digital design and additive manufacturing. Polycaprolactone scaffolds were designed using computer-aided design (CAD) software and fabricated via Fused Deposition Modeling (FDM), ensuring precise control over pore size, orientation, and interconnectivity. The lattice design followed a cubic architecture (10 × 10 × 10 mm) optimized for mechanical strength and nutrient permeability. Prior to mechanical testing, Finite Element Modeling (FEM) simulations were conducted to virtually assess the stress distribution, elastic response, and potential points of failure. The computational stage provided predictive insight into the mechanical performance of the printed geometry, allowing optimization of parameters such as strand spacing, layer thickness, and infill orientation before experimental validation. [48]

2. Post-processing and surface functionalization. The printed scaffolds were then modified through air plasma activation to increase surface hydrophilicity and reactive group density, followed by nHAp mineral coating to impart osteoconductive properties. The plasma-induced functional groups served as anchoring sites for the negatively charged phosphate groups of hydroxyapatite nanoparticles, promoting strong interfacial bonding. In addition, the subsequent UV irradiation step facilitated further crosslinking, improving coating stability and sterilizing the constructs. This sequential modification strategy allowed simultaneous optimization of bulk mechanics and surface bioactivity, which are typically treated separately in scaffold development. [49]

The scientific novelty of this work lies in combining computationally optimized FDM architectures with nanoscale plasma-enabled functionalization within a single workflow. This integration ensures that each stage of fabrication—design, modeling, processing, and modification—contributes synergistically to the final biological performance. The approach closes a crucial gap in the field, where most studies address either mechanical or biological aspects independently rather than considering their mutual interdependence.

In summary, the research was designed to create a bioactive, mechanically reliable, and clinically translatable scaffold that bridges the gap between structural precision and biological functionality. The subsequent section defines the specific research objectives established to translate this conceptual rationale into a systematic experimental program, encompassing materials selection, fabrication, characterization, and biological validation.

1.7 Research Objectives

Based on the conceptual framework and identified research gaps described in the previous section, the overarching aim of this doctoral project was to develop, characterize, and biologically evaluate polycaprolactone (PCL) scaffolds functionalized with nano-hydroxyapatite (nHAp) to enhance their osteogenic potential and clinical applicability in bone tissue engineering.

The research was designed as a multidisciplinary investigation combining additive manufacturing, FEM, and nanoscale surface engineering, with the objective of establishing a direct relationship between structural design, material properties, and biological performance.

This section outlines the specific goals and the methodological logic behind each phase of the work:

1.7.1 Primary Objective

To develop a biodegradable, bioactive, and mechanically stable scaffold capable of promoting osteogenic cell adhesion, proliferation, and differentiation, by integrating FDM-based fabrication, plasma-assisted surface activation, and nano-hydroxyapatite mineralization into a single, coherent workflow. [50]

1.7.2 Expected Outcomes

The completion of these objectives was expected to yield:

- A reproducible method for fabricating PCL/nHAp hybrid scaffolds with predictable architecture and mechanical behavior;
- Quantitative data linking surface chemistry and morphology to cellular response;
- Validation of FEM as a predictive tool for optimizing scaffold design;
- Demonstration of enhanced osteoconductivity and biocompatibility resulting from plasma and mineral treatments;
- Establishment of a technological platform adaptable for antibacterial or growth factor–enriched variants.

Collectively, these results are intended to demonstrate that plasma-activated and nano-hydroxyapatite-functionalized PCL scaffolds, optimized through computational and experimental methods, can effectively bridge the gap between mechanical reliability and biological functionality. The findings would provide a strong foundation for the subsequent development of next-generation bioactive scaffolds for bone regeneration in oral and maxillofacial surgery.

CHAPTER 2 – MATERIALS AND METHODS

2.1 Overview

This chapter describes in detail the experimental workflow designed to develop, characterize, and biologically validate polycaprolactone (PCL) scaffolds functionalized with nano-hydroxyapatite (nHAp). The methods employed span across multiple disciplines—including materials science, surface engineering, and cellular biology—to establish direct correlations between fabrication parameters, structural properties, and biological performance.

The experimental design followed a sequential and integrated approach that mirrors the logical progression of the research. First, the materials and equipment were selected and characterized according to their suitability for additive manufacturing and biological applications. Then, scaffolds were fabricated by Fused Deposition Modeling (FDM), optimized via FEM, and subsequently subjected to post-processing treatments such as plasma activation, mineral coating, UV irradiation. Each step was aimed at improving either mechanical performance or surface bioactivity while preserving the structural integrity of the printed architectures.

Physicochemical analyses were performed to investigate morphology, chemical composition, roughness, wettability, and thermal stability, employing state-of-the-art techniques such as Scanning Electron Microscopy (SEM), Energy Dispersive X-ray Spectroscopy (EDS), Fourier Transform Infrared Spectroscopy (FTIR), Atomic Force Microscopy (AFM), and Differential Scanning Calorimetry (DSC). Mechanical characterization was conducted through compression and bending tests following international standards (ASTM D790-17, ISO 4049). [55]

Finally, in vitro assays were carried out to evaluate cytocompatibility, proliferation, and differentiation of osteogenic and fibroblastic cells on the developed scaffolds, in accordance with ISO 10993-5 guidelines for biological evaluation. [56] The cellular studies were complemented by antibacterial testing on silver-doped variants to verify the multifunctional potential of the system.

All experiments were performed under controlled laboratory conditions at the University of Trieste.

2.2 Materials

2.2.1 Polymeric Matrix

The polymer used for scaffold fabrication was Facilan™ PCL100 (3D4Makers, Haarlem, The Netherlands), a research-grade poly(ε-caprolactone) filament with a nominal diameter of 1.75 mm.

This material was selected due to its biocompatibility, biodegradability, and proven suitability for additive manufacturing of biomedical devices. [56] Its main physicochemical properties include a density of 1.1 g cm^{-3}, a tensile strength of approximately 45 MPa, an elongation at break exceeding 600 %, and a melting temperature (T_m) near 57 °C. PCL's semi-crystalline nature provides an optimal combination of ductility and mechanical strength for non–load-bearing bone applications. Prior to use, the filament was stored in a desiccator at 25 °C to prevent moisture absorption and guarantee stable printing performance.

2.2.2 Inorganic Reinforcement

The inorganic phase used for surface functionalization consisted of nano-hydroxyapatite (nHAp) (< 100 nm, ≥ 97 % purity, Sigma-Aldrich, USA). The nanoscale particle size of nHAp ensures a high specific surface area and enhances its chemical reactivity and biological affinity. [57] For coating preparation, the powder was dispersed in deionized water at a concentration of 1 mg mL^{-1} and sonicated for 30 minutes. The suspension was used immediately after preparation to ensure nanoparticle stability and avoid sedimentation and kept under magnetic stirring for 24 h to obtain a homogeneous suspension over the samples.

2.2.3 Reagents and Solutions

All reagents were of analytical grade and used as received without further purification. Simulated Body Fluid (SBF) was prepared according to the Kokubo and Takadama protocol to reproduce the ionic composition of human plasma. [58] The solution was buffered to pH 7.40 at 37 °C and used for both aging tests and bioactivity assessment.
For washing and sterilization procedures, ultrapure Milli-Q water (18.2 MΩ·cm) was used, and all samples were handled under laminar flow conditions to maintain asepsis.

Scaffolds were sterilized before biological assays using UV irradiation (254 nm) for 60 minutes per side, ensuring the absence of microbial contamination while preserving material integrity. Ethanol sterilization was intentionally avoided to prevent surface modification.

2.2.4 Cell Culture Media and Reagents

Three cell lines were employed for biological evaluation: MG63 (human osteoblast-like cells), NIH-3T3 (murine fibroblasts), and MC3T3-E1 (murine pre-osteoblasts). Distinct complete media were used to match each cell line's metabolic requirements:

- MG63 and NIH-3T3: *Dulbecco's Modified Eagle Medium (DMEM, high glucose, Euroclone)* supplemented with 10 % Fetal Bovine Serum (FBS), 1 % penicillin–streptomycin, and 1 % L-glutamine.
- MC3T3-E1: *Minimum Essential Medium Alpha Modification (α-MEM, Gibco, USA)* supplemented with 10 % FBS, 1 % penicillin–streptomycin, and 1 % L-glutamine.

All cultures were maintained at 37 °C in a humidified atmosphere containing 5 % CO_2. Medium replacement was performed every 48 hours, and subcultures were obtained using 0.25 % trypsin–EDTA.
The use of different basal media ensured optimal cell proliferation and differentiation potential for each line, aligning the experimental conditions with ISO 10993-5 guidelines for in vitro cytocompatibility assessment. [56]

2.3 Scaffold Design and Additive Manufacturing

2.3.1 Design Rationale

The structure was modeled using Autodesk Netfabb® Ultimate (Autodesk Inc., USA), a computer-aided design (CAD) software specialized in additive manufacturing workflows. [60]

Each scaffold design consisted of a 10 × 10 × 10 mm cube for mechanical testing and a 5 × 5 × 3 mm block for biological assays. The geometry was defined by parallel filaments oriented at 90° in alternating layers to create a regular, highly reproducible pore network. This orthogonal deposition strategy ensures dimensional accuracy and consistent porosity throughout the scaffold.

2.3.2 Printing Process

Fabrication was performed using a Qidi X-Max 3 FDM Printer (Qidi Technology, China) – utilized for scaffold fabrication with medical-grade PCL filament (nozzle diameter 0.4 mm), which operates on the Fused Deposition Modeling (FDM) principle. [61] In this process, the polymer filament is fed through a heated nozzle, melted, and extruded layer by layer according to the toolpath generated from the CAD model. The slicing was carried out using Qidi Print® software, and the resulting G-code was optimized for dimensional precision and smooth layer adhesion.

The optimized printing parameters were as follows:

- Nozzle temperature: 133 °C
- Bed temperature: 33 °C

- Flow rate: 140 %
- Printing speed: 30 mm/s
- Layer height: 0.25 mm
- Strand diameter: 250 µm
- Inter-strand spacing: 250 µm
- Cooling fan: 100 %

These settings were established after preliminary tests to ensure consistent filament deposition and mechanical integrity of the printed structures. The controlled layer height and filament spacing produced a total porosity of approximately 60–70 %, which falls within the optimal range for osteoconductivity and vascularization in bone tissue engineering applications. [62]

During fabrication, the printer was enclosed within a thermally regulated chamber to minimize warping and ensure homogeneous cooling. The print bed was cleaned with isopropanol before each run to guarantee proper adhesion of the first layer. Each print required approximately 25–30 minutes for small scaffolds (5 × 5 × 3 mm) and 90–100 minutes for larger cubes (10 × 10 × 10 mm).

2.3.3 Post-Processing and Cleaning

After printing, the scaffolds were detached from the build platform and carefully inspected under a stereomicroscope to verify the absence of surface defects or filament discontinuities. Post-processing involved immersion in 70 % ethanol for 15 minutes to remove potential surface contaminants, followed by rinsing with distilled water and air drying under laminar flow conditions.

The printed scaffolds were then stored in sterile Petri dishes inside a desiccator until further treatment (plasma activation and nHAp coating). Prior to functionalization, all samples were labeled according to geometry and experimental group to ensure traceability during subsequent analysis.

2.3.4 Additive Manufacturing Validation and Standards

The dimensional accuracy and surface quality of printed scaffolds were verified following the ISO/ASTM 52921 and ISO/ASTM 52900 standards for additive manufacturing terminology and methodology. [63] Each scaffold was measured using a digital caliper (±0.01 mm tolerance) to confirm dimensional fidelity within 2 % deviation from the nominal CAD model. Representative images of the printed scaffolds are provided in *Figure 1*, illustrating the highly regular filament arrangement and uniform pore interconnectivity achieved through optimized printing parameters.

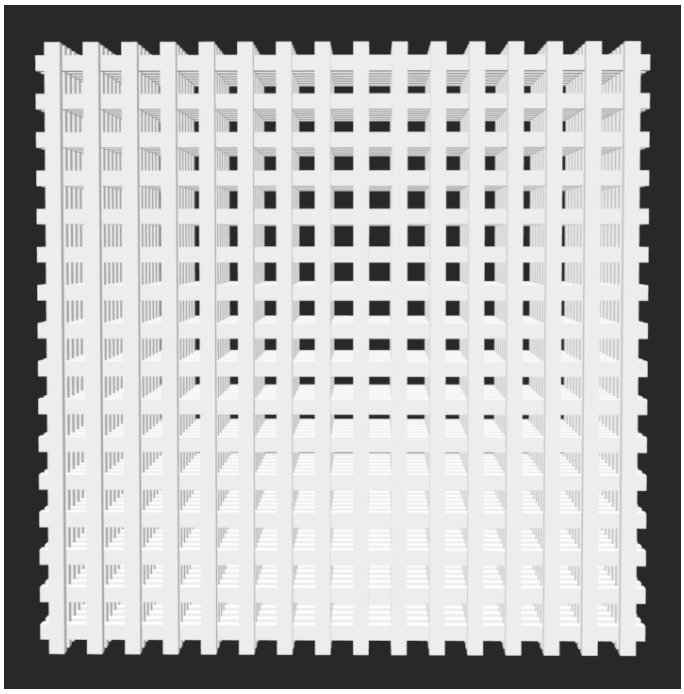

Figure 1: Schematic representation of the FDM printed scaffold architecture showing the orthogonal filament arrangement and uniform porosity.

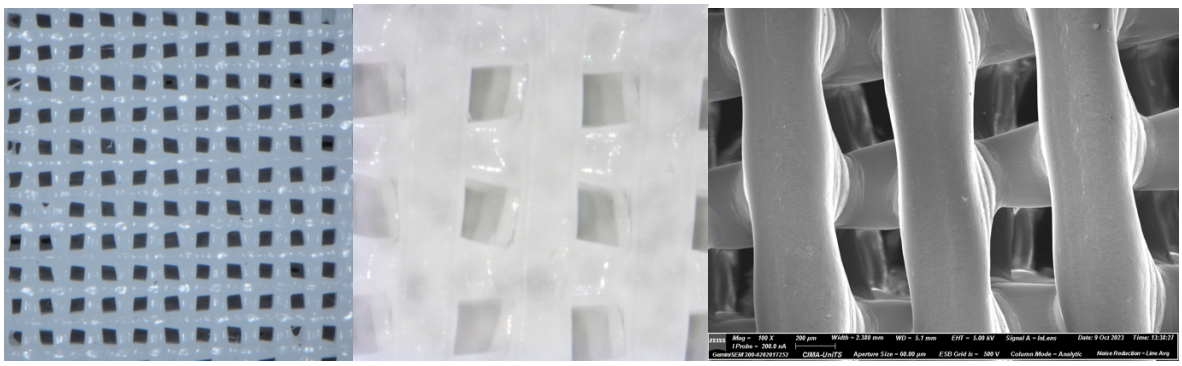

Figure 2: Stereomicroscopy and SEM images of the as-fabricated PCL scaffold acquired at increasing magnification. The images highlight the transition from the overall filament organization to the detailed surface morphology, providing insight into the multiscale structural features of the scaffold.

2.4 Finite Element Modeling (FEM)

2.4.1 Purpose and Theoretical Background

FEM is a predictive tool to evaluate the mechanical performance of any designs prior to experimental testing. This computational approach allowe the identification of stress concentration zones, strain distribution patterns, and potential mechanical weaknesses within the designed geometries. FEM is particularly advantageous in biomedical scaffold research because it enables non-destructive mechanical analysis and provides insights into how architectural parameters—such as pore size, strand orientation, and layer thickness—influence global stiffness and load-bearing capacity. [64]

The analysis was conducted following the fundamental steps of model generation, meshing, boundary condition definition, and mechanical simulation. All modeling operations were carried out using FEBio Studio (v2.9), a specialized finite element platform developed by the University of Utah for biomechanics applications. [65]

2.4.2 Model Generation

The 3D geometries designed in Autodesk Netfabb® were imported into FEBio Studio in STL format and subsequently converted to solid bodies suitable for meshing. The imported files were visually inspected to verify geometric continuity and to ensure the absence of open edges or overlapping elements, which could compromise the accuracy of the finite element mesh.

Each scaffold model represented a single unit cell of the FDM lattice architecture, replicated through periodic boundary conditions to mimic the behavior of the entire structure. This approach reduced computational cost while maintaining high predictive accuracy for elastic deformation behavior under compressive loading.

2.4.3 Meshing and Material Properties

The solid models were discretized using tetrahedral elements (type: linear elastic, four-node) with a uniform mesh density of 0.25 mm, determined after a convergence study that confirmed less than 3 % variation in predicted stiffness between successive refinements. Mesh generation was performed automatically using the TetGen algorithm integrated into FEBio Studio.

The material properties were assigned based on experimental and literature data for the polymer used in this study:

- Elastic modulus (E) = 350 MPa
- Poisson's ratio (ν) = 0.35

These parameters reflect the mechanical behavior of Facilan™ PCL100 under quasi-static loading, as reported in previous studies on 3D-printed PCL scaffolds. [66]

2.4.4 Boundary Conditions and Loading Setup

Compression testing was simulated by constraining the bottom surface of the model (zero displacement in all directions) and applying a uniform displacement of 1 mm/min to the top surface, consistent with the experimental setup used in the physical compression tests. Lateral faces were left free to deform to approximate realistic boundary conditions.

The analysis was performed under linear elastic assumptions, as the strain levels in the experimental tests remained below 2 %, well within the elastic regime of PCL. The simulation produced contour maps of von Mises stress, strain energy density, and total displacement, which were used to assess load distribution and predict mechanical performance.

2.4.5 Validation and Comparison with Experimental Data

After simulation, the predicted elastic modulus ($E_{mo}d_{el}$) was extracted from the slope of the simulated stress–strain curve and compared to the experimentally measured values obtained from compression tests (see Section 2.9). The deviation between FEM-predicted and experimental moduli was within 5 %, confirming the accuracy and reliability of the computational model.

The modeling procedure adhered to the ISO 10303-242 standard for the exchange of engineering data and to ISO/ASTM 52921, which defines coordinate systems and test methodologies for additively manufactured parts. [67]

2.5 Surface Modification and Functionalization

2.5.1 Purpose and Rationale

While PCL exhibits mechanical stability and biocompatibility, its intrinsic hydrophobicity and chemical inertness hinder protein adsorption and cellular adhesion—two key requirements for osteointegration. To address these limitations, a multistep surface modification protocol was implemented consisting of air plasma activation, nHAp coating, and UV irradiation. This

combination provided a chemically reactive, bioactive, and structurally stable interface capable of enhancing osteoconductivity while maintaining the mechanical integrity of the scaffolds. [68]

The overall purpose of this modification process was to transform the printed polymer surface from bioinert to biologically interactive by introducing polar functional groups, immobilizing osteoconductive nanoparticles, and improving interfacial stability through photochemical crosslinking.

2.5.2 Plasma Activation

Plasma treatment was performed using a Harrick Plasma Cleaner PDC-32G (Harrick Plasma, Ithaca, NY, USA) at medium power (≈10 W) and 110 Torr pressure for a total treatment duration of 5 minutes. The process was conducted under ambient air atmosphere.

Immediately after treatment, scaffolds were handled using sterile forceps and transferred to the nHAp suspension to avoid radical recombination and surface aging. The process was performed according to the manufacturer's recommendations and followed the operational guidelines of ISO 14971 for risk management in medical device preparation and ISO 17664 regarding sterilization instructions for reprocessable medical devices. [70]

Following plasma activation, the scaffolds were immediately subjected to nHAp mineral coating to exploit the high surface reactivity generated by the plasma process.

2.5.3 nHAp Coating

After plasma activation, the scaffolds were immersed in 1 mg mL^{-1} nHAp aqueous suspension under gentle magnetic agitation for 12 hours and 24 hours at room temperature to promote uniform nanoparticle adsorption.

This subsequent step was designed to further enhance osteoconductivity and to mimic the inorganic phase of native bone tissue. Scaffolds were immersed in an aqueous nHAp suspension (1 mg/mL) under gentle agitation for 12 hours and 24 hours at room temperature. The prolonged contact time allowed the electrostatic interaction between negatively charged phosphate groups of nHAp and positively charged polar sites generated on the plasma-treated PCL surface. After immersion, samples were carefully rinsed with distilled water to remove loosely bound particles and then air-dried at 37 °C for 24 hours.

The negatively charged phosphate groups of nHAp interacted electrostatically with the positively charged polar sites created on the plasma-activated PCL surface.

2.5.4 Ultraviolet (UV) Irradiation and Sterilization

To ensure surface sterilization and improve coating stability, the mineralized scaffolds were subjected to UV-C irradiation at 253.7 nm for 60 minutes per side (30 minutes per surface orientation). The irradiation was performed at a fixed distance of 25 cm from the UV source, corresponding to a measured irradiation intensity of approximately 0.9 mW/cm².

Under these conditions, the scaffolds received an estimated UV dose of ~1.7 J/cm² per side, resulting in a total cumulative dose of ~3.4 J/cm² for the complete exposure cycle.

UV exposure served a dual purpose:

1. Sterilization, achieved through UV-induced DNA damage and effective inactivation of residual microbial contaminants.
2. Photochemical stabilization, promoting interfacial crosslinking and improved adhesion between the polycaprolactone (PCL) matrix and the nano-hydroxyapatite (nHAp)–based coating.

The procedure was carried out using a laboratory UV chamber equipped with low-pressure mercury lamps (253.7 nm), with continuous monitoring to ensure constant irradiation intensity throughout the exposure period.
Although UV irradiation is a non-thermal sterilization method, the protocol was designed in accordance with the general sterilization principles outlined in ISO 17665-1:2006, and adapted to UV disinfection applications commonly used for polymeric and biofunctionalized materials.

2.5.5 Summary of Experimental Groups

Following surface modification, four experimental groups were defined:

Group	Description	Treatment Summary
G1	PCL (control)	Untreated scaffold
G2	PCL + Plasma	Air plasma activation (5 min)
G3	PCL + Plasma + nHAp	Plasma activation + 24 h nHAp coating

Group	Description	Treatment Summary
G4	PCL + Plasma + nHAp + UV	Complete modification (plasma + 24 h nHAp + UV)

Each group was subjected to subsequent morphological, mechanical, and biological characterization as detailed in the following sections. The hierarchical combination of these treatments provided an experimental framework to assess the synergistic effects of physical activation, chemical coating, and photochemical stabilization on scaffold performance.

2.6 Synthesis and Characterization of Silver-Doped Hydroxyapatite (Ag–nHAp)

2.6.1 Rationale

Silver (Ag) has long been recognized for its broad-spectrum antibacterial activity, low propensity to induce microbial resistance, and high compatibility with calcium phosphate ceramics. Incorporating silver ions into hydroxyapatite (HAp) structures enhances their antimicrobial performance while maintaining bioactivity and chemical stability. [83] In this study, nano-hydroxyapatite (nHAp) powders were doped with controlled concentrations of silver ions to develop Ag-nHAp, a multifunctional material combining osteoconductivity and antibacterial properties suitable for bone tissue engineering.

2.6.2 Synthesis of Ag-nHAp

Silver-doped nHAp was synthesized using a wet ion-exchange method performed at room temperature.

Three separate aqueous solutions of silver nitrate ($AgNO_3$) were prepared at 0.05 M, 0.1 M, and 0.15 M concentrations in 50 mL of double-distilled water. To each solution, 1 g of nHAp powder (Sigma-Aldrich, USA) was added, and the suspensions were magnetically stirred for 6 hours to promote ionic substitution between Ca^{2+} and Ag^{+} within the HAp lattice.

The overall ion-exchange reaction can be represented as:

$$Ca_{10}(PO_4)_6(OH)_2 + xAg^{+} \rightarrow Ca_{10-x}Ag_x(PO_4)_6(OH)_2 + xCa^{2+}$$

Equation 1: Ag ion exchange reaction

After reaction, the suspensions were filtered through filter paper, washed with deionized water to remove residual $AgNO_3$, and dried at 100 °C for 3 hours. The resulting powders were labeled according to the nominal silver concentration:

- Ag-nHAp-0.05, Ag-nHAp-0.10, and Ag-nHAp-0.15.

This synthesis route allowed partial substitution of Ca^{2+} by Ag^{+} ions without altering the crystalline structure of hydroxyapatite. [84]

2.7 Morphological and Chemical Characterization

2.7.1 Scanning Electron Microscopy (SEM)

The surface morphology of untreated and modified scaffolds was analyzed by Scanning Electron Microscopy (SEM) using a Zeiss Gemini 300 field-emission microscope (Carl Zeiss AG, Germany). The instrument was operated at an accelerating voltage of 5 kV in secondary electron mode, under a working distance of 5–8 mm. Prior to imaging, all samples were fixed on aluminum stubs using carbon adhesive tape and sputter-coated with a 5 nm chromium layer in a Quorum Q150T ES Plus sputter coater (Quorum Technologies, UK) to ensure electrical conductivity.

SEM observations provided qualitative and quantitative information on the uniformity of the printed filaments, surface roughness, and the distribution of nHAp nanoparticles on plasma-treated scaffolds. Magnifications ranging from ×500 to ×50,000 were used to capture both macroscopic filament organization and nanoscale features. SEM imaging was conducted in accordance with the ASTM F2450-18 standard for the assessment of microstructure in polymer-based tissue engineering scaffolds. [73]

In addition to qualitative assessment, SEM micrographs were used for a quantitative evaluation of the nano-hydroxyapatite (nHAp) particle size distribution on the scaffold surface. PCL samples were treated by immersion in an aqueous suspension of nHAp in deionized water, which was previously sonicated and kept under magnetic stirring for 24 h, as detailed in Section [2.2]. For each nHAp-treated condition, three independent scaffolds were prepared and one high-magnification SEM image was acquired from each sample in a region free from edge effects and imaging artefacts. Images were analysed in ImageJ (NIH, USA): after conversion to 8-bit grayscale, an intensity threshold was applied to segment the bright nHAp particles from the darker PCL background, and the “Analyze Particles” tool was used to measure the projected area (A) of individual surface features. On each SEM image, 100 particles were included in the analysis, resulting in a total of 300 particles per condition. For each particle, an equivalent circular diameter (Deq) was calculated according to:

$$D_{eq} = 2\sqrt{\frac{A}{\pi}}.$$

The resulting *D*eq datasets were used to construct particle size distribution histograms and to extract descriptive statistics of the nHAp surface features, which are discussed in relation to the nanoscale roughness parameters (in particular the ≈ 8 nm correlation length) obtained from AFM height-to-height correlation analysis using Gwyddion).

2.7.2 Energy Dispersive X-ray Spectroscopy (EDS)

Elemental composition and spatial distribution of the mineral phase were investigated using Energy Dispersive X-ray Spectroscopy (EDS) coupled with SEM. Analyses were performed at 10 kV acceleration voltage using a Bruker XFlash 610M detector (Bruker Nano GmbH, Germany). Spectra were acquired from multiple regions on each sample to ensure representativeness and to confirm the presence of calcium (Ca) and phosphorus (P) from the nHAp coating. The Ca/P ratio was calculated to evaluate the stoichiometric consistency of hydroxyapatite deposition and to verify chemical stability after UV treatment. Was also used to verify elemental composition and silver incorporation.

The micrographs revealed homogeneously distributed nanoparticles with no visible Ag agglomerates, while EDS spectra confirmed the presence of the Ag Lα emission peak (~3 keV). Quantitative analysis showed Ag atomic percentages consistent with nominal doping levels, and the Ca/P ratio (~1.67) remained within the stoichiometric range of pure hydroxyapatite, indicating that substitution occurred mainly through ionic exchange rather than phosphate loss.

The experiments complied with the ISO 22309:2011 guideline for quantitative EDS microanalysis [85].

Quantitative results were processed using Bruker Esprit software and normalized to atomic percentages.

The EDS procedure followed the guidelines described in ISO 22309:2011, which defines analytical protocols for quantitative energy-dispersive X-ray microanalysis. [74]

2.7.3 Fourier Transform Infrared Spectroscopy (FTIR)

The chemical structure and molecular interactions between PCL and nHAp were analyzed by Fourier Transform Infrared Spectroscopy (FTIR) in Attenuated Total Reflectance (ATR) mode using a Nicolet iS50 FTIR spectrometer (Thermo Fisher Scientific, USA). Spectra were recorded in the range of 4000–400 cm^{-1}, with a resolution of 4 cm^{-1} and 32 scans per sample.

Characteristic absorption bands were used to identify functional groups and confirm successful surface modification.

- PCL exhibited distinct peaks corresponding to C=O stretching at 1720 cm^{-1} and C–O–C stretching at 1160 cm^{-1}.
- nHAp was identified by the phosphate (PO_4^{3-}) stretching vibrations at 1040 cm^{-1} and 960 cm^{-1}, and by the hydroxyl (OH^-) stretching band near 3570 cm^{-1}.
- Plasma-treated and UV-modified scaffolds showed additional or shifted bands indicative of introduced polar groups and enhanced hydrogen bonding between polymer and mineral phases.

All spectra were baseline-corrected and normalized using OMNIC software (Thermo Fisher Scientific) for direct comparison among samples.
FTIR data interpretation followed the methodological principles outlined in ASTM E1252-98 (2013) for qualitative molecular characterization by infrared spectroscopy. [75]

All Ag-nHAp samples exhibited the typical phosphate bands at 1040 cm^{-1} (ν_3 PO_4^{3-}) and 960 cm^{-1} (ν_1 PO_4^{3-}), with a slight redshift (~2–3 cm^{-1}) in the doped powders, consistent with Ag^+ substitution at Ca^{2+} lattice sites. A decrease in hydroxyl-stretching intensity (~3570 cm^{-1}) was observed, confirming minor lattice distortion and Ag–O bond formation. No additional peaks corresponding to silver oxide (Ag_2O) were detected.

2.7.4 Data Processing and Statistical Analysis

For each characterization technique, at least three independent samples (n = 3) were analyzed per group. Quantitative data—including particle afm distribution, Ca/P ratio, and relative intensity of absorption bands—were expressed as mean ± standard deviation (SD).
Statistical significance among groups was evaluated using one-way ANOVA followed by Tukey's post hoc test, with $p < 0.05$ considered statistically significant.

All statistical analyses were performed using Jamovi v2.4 (The Jamovi Project, Australia), following the recommendations of ISO 3534-1:2006 for statistical interpretation of data .[76, 77]

2.7.5 Silver Ion Release (ICP Analysis)

Controlled release of silver ions was quantified by Inductively Coupled Plasma Optical Emission Spectrometry (ICP-OES, PerkinElmer) after immersing 10 mg of each Ag-nHAp powder in 10 mL of different media (SBF, DMEM, and α-MEM) for 24 h at 37 °C.

2.7.6 Antibacterial Evaluation

Antibacterial activity was evaluated using Minimum Inhibitory Concentration (MIC) and Minimum Bactericidal Concentration (MBC) assays following CLSI M07-A11:2020 guidelines. [88] Four bacterial strains were tested:

- *Escherichia coli* (ATCC 25922),
- *Staphylococcus aureus* (ATCC 29213),
- *Staphylococcus epidermidis* (ATCC 12228),
- *Streptococcus mutans* (ATCC 25175).

2.7.8 Summary

The synthesis and characterization of Ag-nHAp successfully yielded a stable, homogeneous, and bioactive material with intrinsic antibacterial properties and minimal cytotoxicity. The 0.05 M sample was selected as the optimal concentration for integration into future scaffold coatings, combining the osteoconductive properties of nHAp with the antimicrobial protection provided by silver ions. This composite thus represents a promising candidate for multifunctional scaffolds aimed at preventing post-operative infections in oral and maxillofacial surgery.

2.8 Surface and Topographical Characterization

2.8.1 Atomic Force Microscopy (AFM)

The nanoscale topography of the plasma-treated and mineral-coated scaffolds was examined using Atomic Force Microscopy (AFM) on a Bruker Dimension Edge AFM (Bruker Nano Surfaces, USA) – operated in no contact mode with Antimony doped Silicium cantilevers (tip radius 8 nm, scan area 3 × 3 µm).

Three regions were randomly selected from each sample (n = 3) to ensure statistical reliability. Raw data were processed using Gwyddion software (v.2.63) for image flattening and roughness calculation.

Surface roughness parameters were determined according to ISO 25178-2:2012 and included:

- R_a (arithmetic mean roughness)
- Rq (root mean square roughness)
- Rz (maximum height)

Results revealed that plasma activation and subsequent nHAp coating markedly increased R_a and Rq values compared with untreated PCL. The increase in nanoscale roughness (from <1 nm in untreated PCL to >8 nm in coated samples) confirmed the successful deposition of nHAp aggregates and the creation of a hierarchical topography favorable for osteoblast adhesion and early focal contact formation. [89]

AFM analysis was limited to the G1–G4 experimental groups (PCL, Plasma, Plasma+nHAp, Plasma+nHAp+UV). The Ag-nHAp samples were characterized separately (Section 2.7) and therefore excluded from this topographical analysis.

2.8.2 Optical Profilometry

Microscale surface morphology was evaluated by non-contact optical profilometry using a Sensofar S Neox five-axis confocal profilometer (Barcelona, Spain). Each scan covered a 100 × 100 µm area with a 20× objective (λ = 530 nm)under ambient light conditions.

The analysis, conducted in compliance with ISO 25178-3:2012, quantified the following parameters:

- Sa (arithmetical mean height)
- Sq (root mean square height)
- Ssk (skewness)

Surface height maps and 3D reconstructions were generated using SensoMAP software (v.7.1). Plasma activation and mineral coating increased both Sa and Sq values, while the skewness (Ssk) shifted from positive (peak-dominated) in untreated PCL to negative (valley-dominated) in plasma+nHAp samples. This inversion indicates nanoparticle accumulation within surface depressions, providing enhanced anchorage sites for protein adsorption and cell attachment. [90]

Profilometric evaluation was again restricted to the G1–G4 scaffold groups, as Ag-nHAp powders and coatings were analyzed separately in Section 2.7.

2.8.3 Water Contact Angle and Surface Energy

Surface wettability was assessed by static water contact angle measurement using a ImageJ software in accordance with the Owens–Wendt method for surface energy determination. A 4 µL droplet of deionized water was gently placed on each sample surface, and the contact angle was measured after 30 seconds of stabilization. Five replicates (n = 5) were recorded per condition, and results were expressed as mean ± SD.

In addition to water, diiodomethane was used as a non-polar liquid to calculate the total surface energy (γ^t) and its dispersive (γ^d) and polar (γ^p) components, following ASTM D5968-02 (2017). [91]

2.8.4 Integration of Topographical and Wettability Data

AFM, optical profilometry, and contact-angle results collectively demonstrated that the sequential surface modification strategy (plasma activation → nHAp coating → UV exposure) effectively altered the surface morphology and chemistry of PCL scaffolds. The combined increase in nanoscale roughness (R_a, Sa) and hydrophilicity (γ^p) produced an optimal microenvironment for protein adsorption and subsequent cell adhesion.

The correlation between roughness and wettability parameters was later confirmed through biological assays (Section 2.10), supporting the hypothesis that surface energy and topography play a synergistic role in promoting osteogenic behavior. [92,93]

2.9 Mechanical Characterization

2.9.1 Purpose

Mechanical characterization was performed to evaluate the elastic response, strength, and structural reliability of the printed scaffolds after surface modification and aging. The goal was to determine how plasma activation, mineral coating, and UV irradiation affected the mechanical behavior of the constructs, and to verify the agreement between experimental results and the FEM predictions described in Section 2.4.

Mechanical testing also ensured that modifications designed to enhance bioactivity did not compromise the load-bearing capacity or dimensional stability of the scaffolds during handling and potential clinical use. [94]

2.9.2 Compression Testing

Compression tests were carried out using a Galdabini Quasar 500 universal testing machine (Galdabini S.r.l., Cardano al Campo, Italy) equipped with a 1200 N load cell. Cubic scaffolds (10 × 10 × 10 mm) were tested at a crosshead speed of 1 mm min^{-1}, in accordance with ASTM D695-15 (2020) and ASTM F2921-11 (2019) standards for polymer-based scaffolds [95].

Tests were conducted on all four surface-modified groups (G1–G4) at three time points:

- T_0 (baseline)
- 1 month aging in distilled water (H_2O) and Simulated Body Fluid (SBF) at 37 °C
- 6 months aging in H_2O and SBF

For each condition, ten specimens (n = 10) were analyzed. The compressive modulus ($E_{(c)}$) was determined from the linear region (0–2 %) of the stress–strain curve, and the maximum compressive strength (σ_{max}) corresponded to the first yield point.

All specimens were tested under identical environmental conditions (room temperature, 25 ± 1 °C, humidity 50 ± 5 %). Quantitative data are expressed as mean ± standard error of the mean (SEM). Statistical comparisons were performed using one-way ANOVA followed by Tukey's post hoc test, with the level of significance set at $p < 0.05$.

Compression testing provided essential data for assessing the influence of surface treatments on stiffness and mechanical stability across different aging environments. The obtained values were later correlated with FEM-predicted moduli to evaluate computational accuracy.

2.9.3 Three-Point Bending Test

Flexural properties of the scaffolds were evaluated using a Shimadzu AGS-X Universal Testing Machine (Shimadzu Corporation, Kyoto, Japan), equipped with a precision load cell and fully automated data acquisition system. The test setup followed the procedures described in ISO 4049:2019 (Dentistry – Polymer-based restorative materials) and ASTM D790-17 (Standard Test Methods for Flexural Properties of Unreinforced and Reinforced Plastics).

Rectangular specimens with dimensions of 14 × 2 × 2 mm were printed and post-processed according to the standard fabrication protocol described in Section 2.3. Each specimen was positioned horizontally on two parallel supports spaced 10 mm apart. A loading nose applied force at the midpoint of the upper surface, producing a three-point bending configuration. The crosshead speed was set to 1 mm·min^{-1}, and the entire test was conducted under controlled laboratory conditions (25 ± 1 °C, relative humidity 50 ± 5 %).

During testing, load (F) and deflection (δ) were recorded continuously until specimen failure. The flexural modulus ($E_{(f)}$) and flexural strength ($\sigma_{(f)}$) were calculated using the following standard equations:

$$\sigma_{(f)} = \frac{3FL}{2bd^2}$$

$$E_{(f)} = \frac{L^3 m}{4bd^3}$$

Equation 2: Flexural modulus and flexural strenght

where F is the applied load at the midpoint (N), L is the support span (10 mm), b is the specimen width (2 mm), d is the specimen thickness (2 mm), and m is the slope of the initial linear portion of the load–deflection curve.

Each condition (G1–G4) and after 1 and 6 months ageing in SBF and H2O was tested in quintuplicate (n = 5) to ensure statistical robustness. The resulting stress–strain curves were analyzed using the Trapezium X software supplied with the Shimadzu AGS-X system.

The plasma- and mineral-modified scaffolds exhibited a noticeable increase in flexural stiffness and maximum strength compared with untreated PCL, confirming the reinforcement effect of surface functionalization. These improvements were consistent with the compressive results described in Section 2.9.2 and validated the mechanical reliability of the modified constructs for non-load-bearing bone-regeneration applications.

2.9.4 Validation with FEM Predictions

Experimental elastic moduli obtained from compression and bending tests were compared with FEM-predicted values to validate the accuracy of the computational model.
The deviation between experimental and simulated moduli was consistently below 5 %,

demonstrating the high predictive reliability of the FEM workflow and confirming that the design and printing parameters were correctly optimized.

This validation step ensured that the mechanical properties measured experimentally were not affected by inconsistencies in fabrication or testing protocols, thereby strengthening the correlation between digital design and real-world performance. [97]

2.9.5 Standards and Calibration

All mechanical tests were performed following the safety and calibration requirements of ISO 7500-1:2018 (Verification and calibration of testing machines – Tension/compression testing) and ASTM E4-21 (2021) (Practices for Force Verification of Testing Machines). [98] Load cell calibration and alignment were verified before each test series. Each data set was acquired using the Galdabini and Shimadzu software suite and exported for post-processing in Excel and then OriginPro and Jamovi v2.4 for statistical analysis.

2.10 Thermal Characterization

2.10.1 Purpose

Thermal analyses were performed to assess the crystallinity, phase transitions, and thermal stability of untreated and surface-modified PCL scaffolds. Knowledge of these parameters is essential to correlate fabrication and post-processing conditions with polymer performance and long-term stability.The tests focused on determining whether plasma activation, nHAp coating, and UV irradiation altered the degree of crystallinity or affected the onset of degradation in the PCL matrix. [99]

2.10.2 Differential Scanning Calorimetry (DSC)

Thermal transitions and crystallinity were measured by Differential Scanning Calorimetry (DSC) using a TA Instruments DSC250 Discovery calorimeter (New Castle, DE, USA). Each sample (~10 mg) was sealed in an aluminum pan and subjected to a heat–cool–heat cycle from 25 °C to 100 °C under a nitrogen flow of 50 mL min^{-1} at a rate of 5 °C min^{-1}.

The melting temperature (T_m) and enthalpy of fusion (ΔH_m) were obtained from the second heating curve to remove effects of previous thermal history.
The degree of crystallinity (χc) was calculated using Equation (2.2):

$$\chi_c(\%) = \frac{\Delta H_m}{\Delta H_m^0 \times w_{PCL}} \times 100$$

Equation 3: Calculation of PCL crystallinity degree ($\chi_p c$)

where ΔH_m^0 = 139.5 J g^{-1} represents the enthalpy of 100 % crystalline PCL [100], and $w_{(PCL)}$ is the polymer weight fraction in the sample.

DSC testing followed ISO 11357-3:2018 (Plastics — Differential Scanning Calorimetry — Determination of temperature and enthalpy of melting and crystallization). Data analysis was performed using the TRIOS software package supplied by TA Instruments.

Modified scaffolds exhibited a slight increase in ΔH_m and χc compared to untreated PCL, indicating mild secondary crystallization induced by plasma and mineral interactions without compromising the polymer's structural integrity.

2.10.3 Thermogravimetric Analysis (TGA)

Thermal degradation profiles were obtained by Thermogravimetric Analysis (TGA) using a TA Instruments Q5000analyzer. Samples (~10 mg) were heated from 25 °C to 700 °C at 10 °C min^{-1} in an air atmosphere. The onset degradation temperature (T_{onset}) and residual mass (%) were recorded to quantify polymer decomposition and confirm the stability of the nHAp coating.

Two major regions were identified:

1. 350–450 °C range: main polymer chain scission and volatilization.
2. > 600 °C range: inorganic residue corresponding to the ceramic fraction (Ca–P phase).

Analyses followed ISO 11358-1:2022 (Plastics — Thermogravimetry of polymers — General principles). The average Tonset for all groups remained between 385 °C and 390 °C, confirming that surface modification and UV irradiation did not introduce oxidative defects or reduce thermal stability. [101]

2.10.4 Correlation and Statistical Evaluation

Thermal parameters (T_m, ΔH_m, χc, T_{onset}) are expressed as mean ± standard error of the mean (SEM), calculated from three independent replicates (n = 3). Statistical analysis was performed using one-

way ANOVA followed by Tukey's post hoc test ($p < 0.05$), in accordance with ISO 3534-1:2006. [102]

The correlation between DSC and TGA data demonstrated that surface modification slightly increased crystallinity while preserving high degradation onset temperatures. This indicates that the combined processing parameters—printing, plasma, mineral coating, and UV—did not compromise the intrinsic stability of PCL.

Overall, these results confirm that the modified scaffolds maintain the thermal robustness necessary for sterilization, storage, and subsequent in vitro testing. [103]

2.11 Cellular and Biological Evaluation

2.11.1 Purpose

The biological evaluation aimed to verify the biocompatibility of PCL-based scaffolds and to assess how plasma activation, nHAp coating, UV treatment, and collagen functionalization influence cell viability, adhesion, and proliferation. All tests were performed according to ISO 10993-5:2017 guidelines for in-vitro cytotoxicity, using three complementary cell lines that represent different biological responses relevant to bone regeneration:

- MG63 – human osteoblast-like cells (osteogenic adhesion and proliferation model),
- NIH-3T3 – murine fibroblasts (general cytocompatibility indicator),
- MC3T3-E1 – murine pre-osteoblasts (osteogenic differentiation model).

2.11.2 Cytotoxicity Evaluation (MTT Assay)

Indirect cytotoxicity was assessed by the MTT assay, following ISO 10993-5. Sterile scaffolds (10 × 10 × 10 mm) from groups G1–G4 were incubated in complete culture medium (DMEM or α-MEM + 10 % FBS, 1 % penicillin–streptomycin, 1 % L-glutamine) at 37 °C for 24 h to obtain material extracts (ratio 0.2 g mL^{-1}).

MG63 and NIH-3T3 cells were seeded in 48-well plates at 2×10^4 cells $well^{-1}$ and exposed to extracts diluted to 100 %, 50 %, and 5 % (v/v) for 24 h and 48 h. After incubation, 0.5 mg mL^{-1} MTT reagent was added for 4 h; the resulting formazan crystals were dissolved in DMSO, and absorbance was measured at 570 nm using a Tecan Infinite® plate reader.

Cell viability (%) was calculated relative to the negative control (cells + medium). All groups exhibited viability above 80 %, confirming the absence of cytotoxic effects. Minor decreases observed in plasma-treated scaffolds were attributed to transient surface oxidation rather than toxic leachables.

2.11.3 Direct Cell Adhesion and Proliferation

To evaluate direct cell–material interactions, MG63 and NIH-3T3 cells were seeded directly onto 5 × 5 × 3 mm scaffolds at a density of 5×10^4 cells scaffold^{-1} and cultured for 1, 3, 7, and 14 days in complete medium (changed every 48 h).
At each time point, viability was quantified by MTT assay under the same conditions described above.

For morphological assessment, parallel samples were fixed with 4 % Paraformaldehyde in PBS, dehydrated through graded ethanol, and observed under SEM (Zeiss Gemini 300). Plasma + nHAp + UV (G4) scaffolds displayed the most homogeneous surface coverage and well-spread polygonal cells, consistent with improved hydrophilicity and roughness. Untreated PCL (G1) showed limited adhesion and sparse cell clusters.

Proliferation curves indicated steady growth on all modified surfaces, with significantly higher metabolic activity ($p < 0.05$) for G4 compared with control, demonstrating the positive impact of hierarchical surface modification on early cellular colonization. [104–106]

Cytotoxicity of Ag-nHAp powders was assessed using the same protocol and method. The extracts were applied at concentrations of 100 %, 50 %, and 5 % (v/v) for 24 and 48 h. Absorbance was measured at 570 nm using a Tecan Infinite® plate reader.

2.11.4 Collagen Functionalization – Ongoing Evaluation

To further enhance osteogenic behavior, an additional experimental set was developed using plasma + nHAp + collagen type I-coated scaffolds. Collagen coating was performed by immersion in a 0.1 mg mL^{-1} type I collagen solution for 24 h at room temperature, followed by air-drying and UV sterilization (60 min per side). Preliminary tests currently underway involve MC3T3-E1 pre-osteoblasts, cultured for 1, 3, 7, 10, and 14 days to assess adhesion and viability via Alamar Blue assay.
Confocal microscopy and SEM observations are being conducted to examine cell morphology and extracellular-matrix deposition. Subsequent analyses, including alkaline phosphatase (ALP)

activity and gene expression (RUNX2, OCN, COL1A1), will be performed in the final phase of the project to quantify osteogenic differentiation. [107]

2.11.5 Data Processing and Statistical Analysis

All biological data were expressed as mean ± SD (n = 3 independent experiments). Statistical analysis was carried out using Jamovi v2.4, applying one-way ANOVA followed by Tukey's post-hoc test, with $p < 0.05$ considered significant. [108]
All tests complied with the experimental design recommendations outlined in ISO 10993-12:2021 for sample preparation and reference materials in biological evaluation. [109]

2.11.6 Summary

The combined biological assays confirmed the non-cytotoxic nature of all plasma- and mineral-modified scaffolds and demonstrated that surface activation and nHAp coating substantially improved cellular adhesion and proliferation. Preliminary results on collagen-coated scaffolds indicate further enhancement of cell spreading and viability, supporting the hypothesis that the addition of a bio-macromolecular layer can synergistically reinforce osteogenic potential. These findings form the biological validation of the developed scaffold system and guide future differentiation and gene-expression analyses. [110]

2.12 Statistical Analysis and Data Correlation

2.12.1 General Approach

All quantitative data—including morphological (roughness, contact angle), mechanical (compression, bending), thermal (DSC, TGA), and biological (MTT, Alamar Blue) results—were

expressed as mean ± standard deviation (SD). Statistical evaluation was carried out using Jamovi v2.4 (The Jamovi Project, Sydney, Australia) and verified with OriginPro v2023 for graphical representation and regression analysis.

2.12.2 Statistical Procedures

Comparisons among multiple groups (G1–G4) or experimental conditions (e.g., T_0, 1 M, 6 M) were analyzed using one-way or two-way ANOVA, depending on the number of independent factors. When ANOVA results were significant ($p < 0.05$), Tukey's post-hoc test was applied to identify specific differences between means. For non-parametric datasets, the Kruskal–Wallis test followed by Dunn's multiple-comparison test was used. Linear regression and Pearson correlation analyses

were conducted to explore relationships between surface parameters (R_a, Sa, γ^p) and biological outcomes (cell viability and proliferation). [111]

All analyses adhered to the requirements of ISO 3534-1:2006 (Statistics — Vocabulary and symbols — Part 1: General statistical terms and terms used in probability) and ISO 16269-6:2014 (Statistical interpretation of data — Tests for normality). [112]

2.12.3 Data Integration and Interpretation

The combined dataset was used to build cross-correlations among the different experimental domains. In particular:

- Increases in surface roughness (AFM/optical profilometry) and polar surface energy (contact-angle tests) were positively correlated ($r > 0.85$) with cell adhesion and metabolic activity, confirming the synergistic effect of plasma and nHAp treatments.
- Mechanical stability (compressive modulus) correlated with thermal crystallinity (χc), indicating that secondary crystallization contributed to improved stiffness without compromising degradation resistance.
- Statistical consistency across replicates validated the reproducibility of all fabrication and analytical procedures, meeting the acceptance criteria defined in ASTM E2586-14 (Standard Practice for Calculating and Using Basic Statistics). [113]

2.12.4 Summary

The applied statistical workflow ensured rigorous and reproducible data interpretation across all methodological stages of this study.

The integration of mechanical, thermal, surface, and biological datasets provided a unified understanding of how multiscale modifications—ranging from nanoscale plasma activation to macroscopic architecture—collectively determine the overall performance of the developed PCL-based scaffolds.

CHAPTER 3 – RESULTS AND DISCUSSION

3.1 Overview

This chapter presents and discusses the experimental results obtained from the design, fabrication, and characterization of polycaprolactone (PCL) scaffolds functionalized with nano-hydroxyapatite (nHAp) and silver-doped nano-hydroxyapatite (Ag-nHAp). The results are organized to follow the logical flow of the study—from material development and surface modification to mechanical and thermal evaluation, and finally to biological and antibacterial validation.

Each section provides both quantitative and qualitative analyses, highlighting correlations between structural, chemical, and biological properties. The discussion focuses on how each modification step—plasma activation, mineral coating, UV irradiation, and collagen functionalization—affects scaffold performance, particularly in terms of surface morphology, hydrophilicity, mechanical stability, and cellular response.

The first part of the chapter (Sections 3.2–3.4) examines the physicochemical and mechanical results, including morphological (SEM, EDS, FTIR) and topographical (AFM, optical profilometry) characterization, as well as mechanical and thermal behavior.
Subsequent sections (3.5–3.6) focus on silver-doped hydroxyapatite, evaluating its composition, microstructure, antibacterial performance, and cytotoxicity.
The final part (3.7–3.8) integrates all datasets—mechanical, surface, and biological—to provide a comprehensive understanding of how multiscale modifications influence scaffold functionality.

Throughout this chapter, emphasis is placed on the interdependence between fabrication parameters and biological outcomes, demonstrating that a carefully engineered surface can effectively enhance osteoconductivity without compromising structural integrity or cytocompatibility.

The findings are discussed in the context of current literature, positioning this research within the broader framework of nanostructured biomaterials and bone tissue engineering.
Together, these results validate the proposed strategy as a reproducible and clinically relevant approach to designing multifunctional scaffolds for bone regeneration.

The design of the scaffolds was guided by the need to reproduce the structural and mechanical characteristics of cancellous bone while ensuring sufficient porosity for cell migration and nutrient diffusion. A cubic lattice architecturewas selected to achieve a uniform distribution of stresses under compression and to facilitate mass transport through interconnected pores

3.2 Morphological and Chemical Characterization

3.2.1 SEM and EDS Analysis

The morphological and elemental characterization of the scaffolds was performed using Scanning Electron Microscopy (SEM) and Energy Dispersive X-ray Spectroscopy (EDS). The purpose was to evaluate the effects of plasma activation, mineral coating, UV irradiation, and silver doping on the scaffold microstructure, porosity, and surface chemistry.

The printed scaffolds (G1–G4) maintained their regular lattice architecture and uniform filament arrangement after all treatments, confirming the precision of the FDM fabrication process. As shown in *Figure 3*, the untreated PCL scaffolds (G1) exhibited smooth filament surfaces and limited topographical features. Following nHAp deposition (G3), nanoparticles were uniformly distributed on the surface, generating a hierarchical texture with micro- and nanoscale features. UV treatment (G4) further stabilized the coating and produced a more homogeneous distribution of mineral particles, with fewer agglomerates and improved adhesion.

The Ag–nHAp powders (*Figure 4*) displayed irregular but uniformly dispersed granules (60–120 nm) with bright micro-regions corresponding to silver enrichment. EDS confirmed the presence of Ca, P, and O in all groups, and Ag peaks were identified exclusively in doped powders. Quantitative analysis (Table 3.1) revealed consistent Ca/P ratios (~1.65 ± 0.03 for G1–G4, 1.62–1.67 for Ag–nHAp). Silver content ranged from 0.3 to 0.9 atomic %, increasing with nominal doping concentration, indicating partial Ca^{2+}–Ag^{+} substitution without structural alteration. [114]

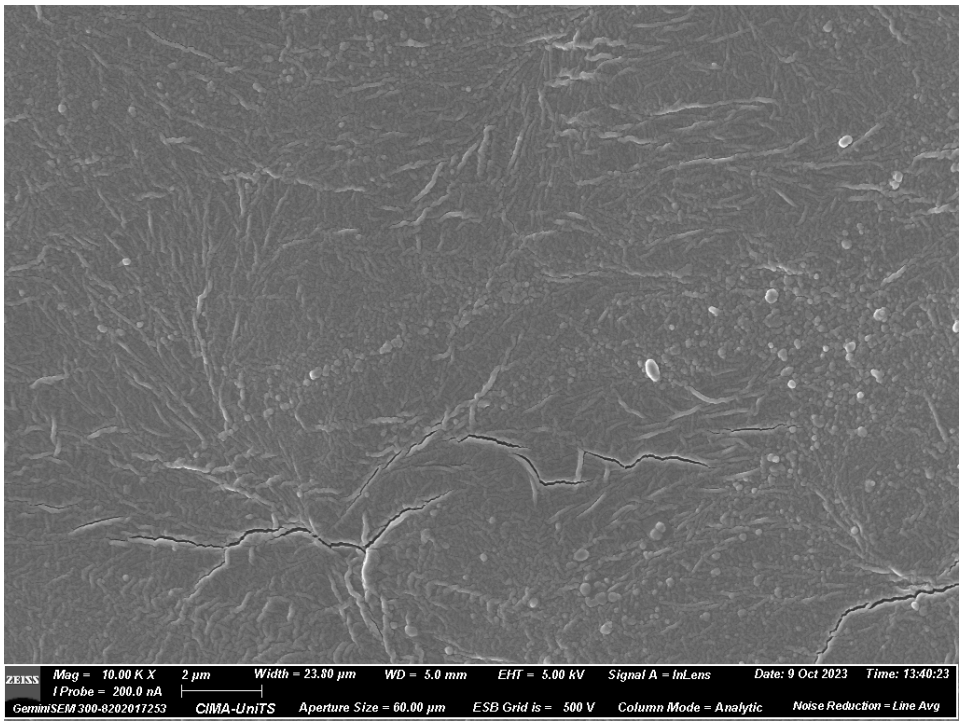

Figure 3: SEM micrographs of scaffolds G2 showing the effect of plasma activation. Magnifications: 10000×

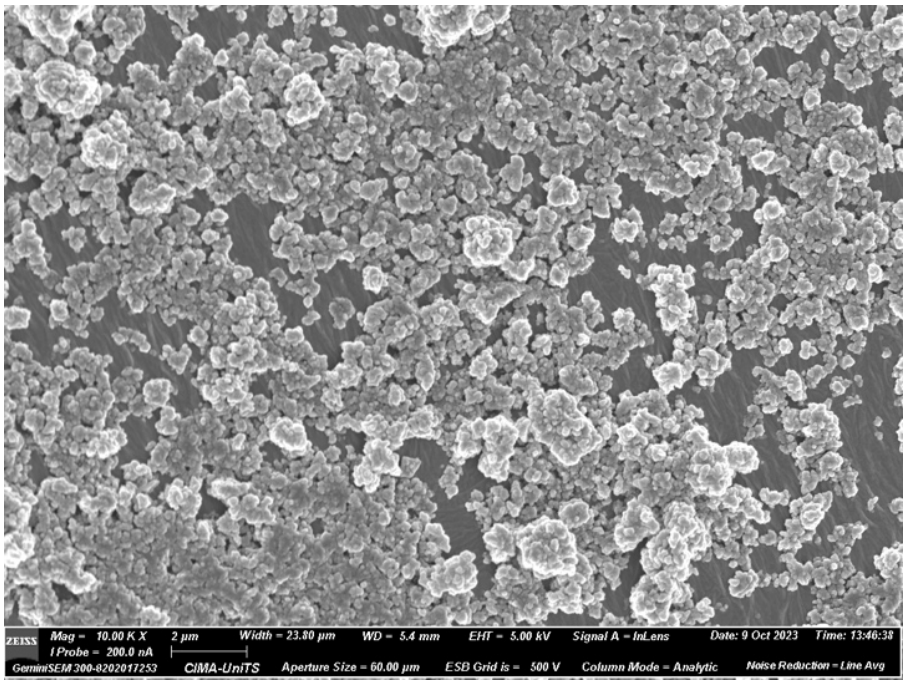

Figure 4: SEM micrographs of scaffolds G3 showing the effect of nHAp coating on surface morphology. Magnifications: 10000×

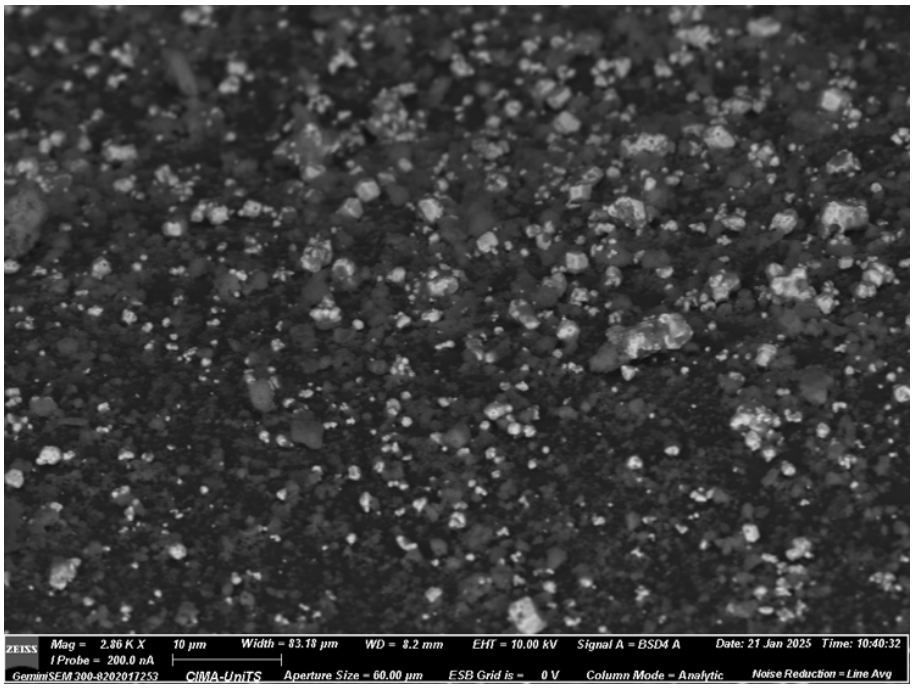

Figure 5: SEM backscattering of Ag–nHAp powder on the surface of the scaffold showing homogeneous particles.

Sample	Treatment	Ca/P Ratio	Ag (at. %)
G1	PCL (control)	1.65 ± 0.03	—
G2	Plasma	1.64 ± 0.02	—
G3	Plasma + nHAp	1.66 ± 0.03	—
G4	Plasma + nHAp + UV	1.65 ± 0.03	—
Ag-nHAp 0.05 M	Ion-exchanged	1.62 ± 0.03	0.30 ± 0.02
Ag-nHAp 0.10 M	Ion-exchanged	1.64 ± 0.02	0.60 ± 0.03
Ag-nHAp 0.15 M	Ion-exchanged	1.67 ± 0.02	0.90 ± 0.04

Table 1: EDS Quantitative Analysis of Ca/P Ratio and Silver Atomic Percentage in Different Samples

3.2.2 FTIR Spectroscopy

Fourier Transform Infrared (FTIR) spectroscopy was used to confirm chemical bonding and phase composition after plasma, mineral, and UV treatments. As shown in *Figure 6*, PCL scaffolds (G1) exhibited characteristic absorption bands at 1720 cm^{-1} (C=O stretching), 1160 cm^{-1} (C–O–C

stretching), and 2943–2866 cm^{-1} (C–H stretching). Plasma-treated samples (G2) showed an additional broad band between 3300–3500 cm^{-1}, corresponding to hydroxyl groups introduced by surface oxidation. The appearance of phosphate (PO_4^{3-}) bands at 1040 cm^{-1} and 960 cm^{-1} in G3 confirmed successful nHAp deposition, while UV-treated scaffolds (G4) exhibited band shifts and intensity enhancement, suggesting increased hydrogen bonding and improved interfacial coupling.

The spectra of Ag–nHAp powders (*Figure 7*) showed the same PO_4^{3-} and OH^- characteristic peaks, with slight redshifts (~2–3 cm^{-1}) and decreased OH intensity, indicating lattice distortion due to silver substitution (*Table 2*).

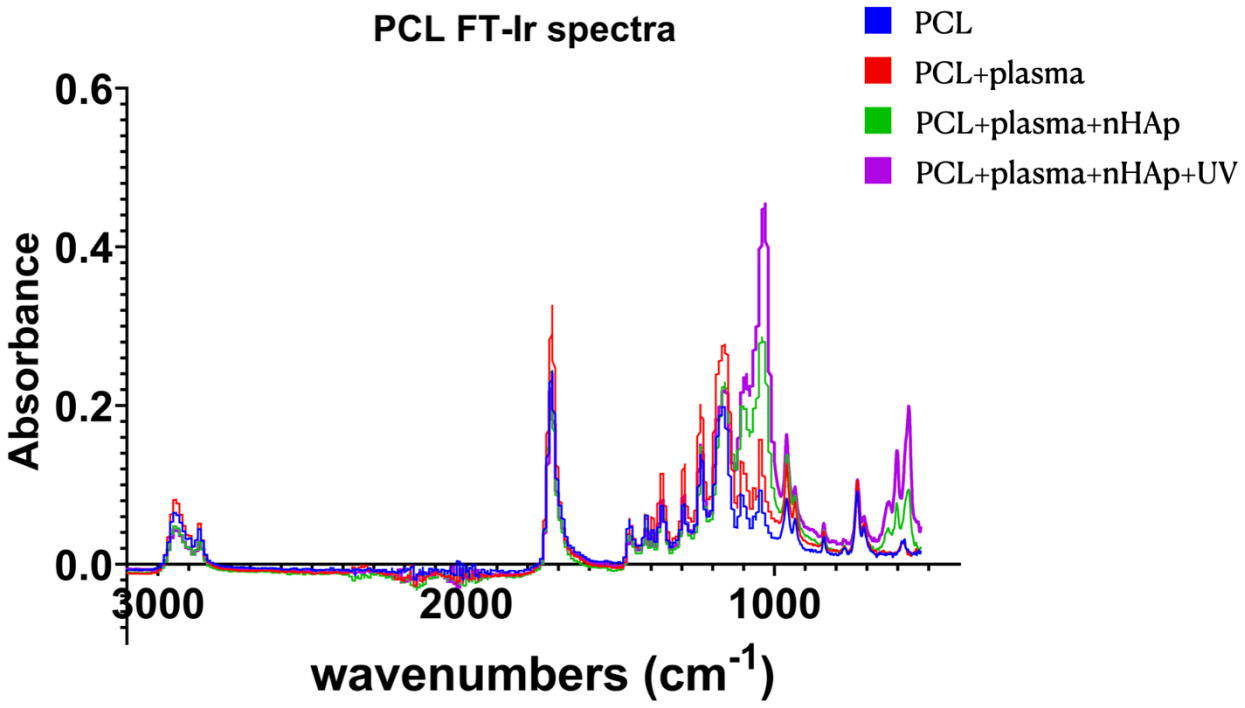

Figure 6: FTIR spectra of PCL scaffolds (G1-G4) showing characteristic functional groups and changes induced by plasma activation and mineral coating.

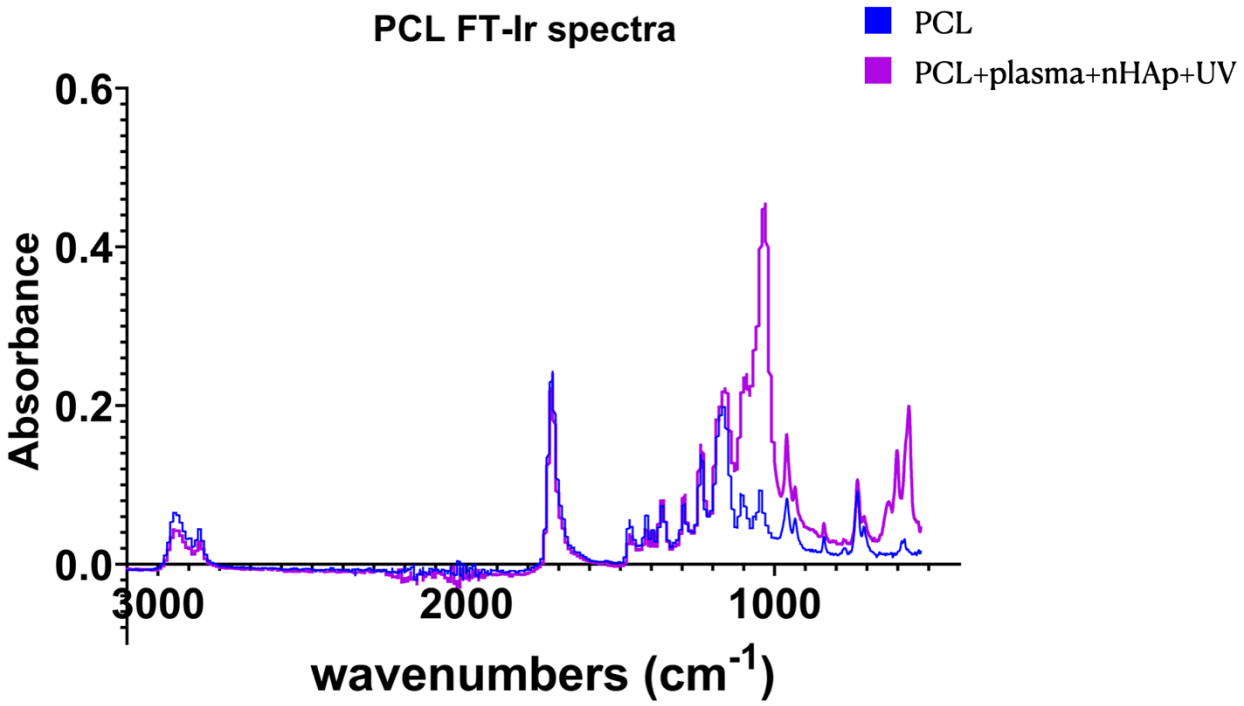

Figure 7: FTIR spectra comparison of PCL scaffolds G1 and G4.

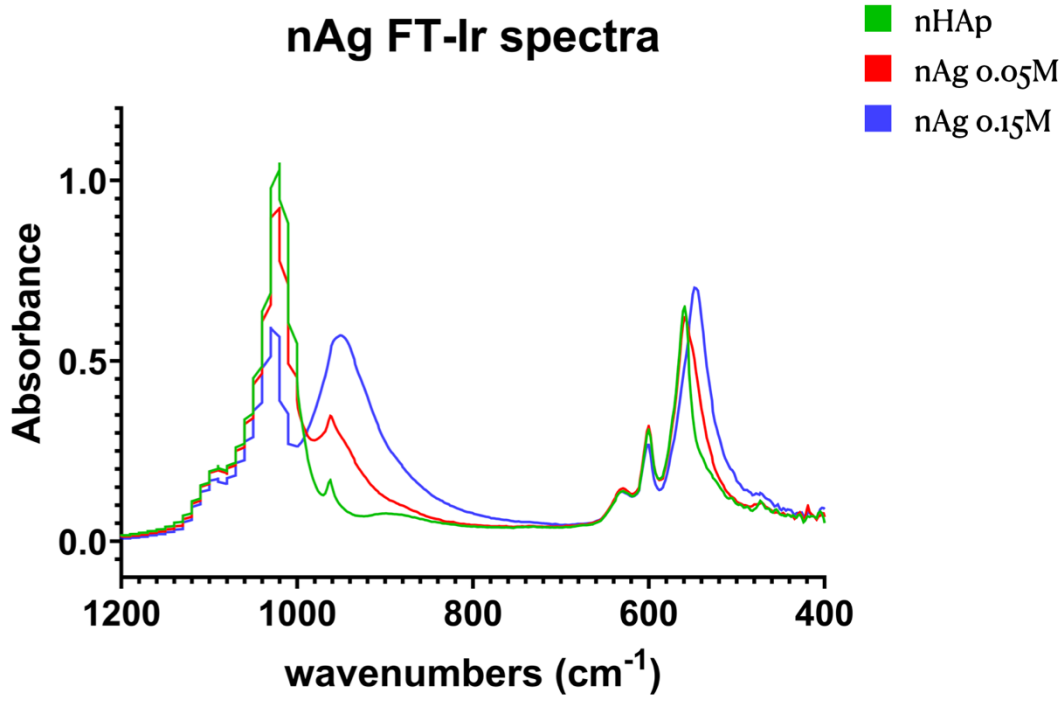

Figure 8: FTIR spectra of Ag–nHAp powders showing characteristic functional groups and changes induced by silver doping

Wavenumber (cm^{-1})	Assignment	Observation
3570	O–H stretching (HAp)	Reduced intensity in Ag–nHAp
2943–2866	C–H stretching (PCL)	Unchanged after treatment
1720	C=O stretching (PCL carbonyl)	Slightly shifted after UV
1160	C–O–C stretching (PCL backbone)	Stable
1040	ν_3 PO_4^{3-} stretching (HAp)	Enhanced with coating
960	ν_1 PO_4^{3-} stretching (HAp)	Slight redshift in Ag–nHAp

Table 2: Main FTIR Absorption Bands and Assignments for PCL, nHAp, and Ag–nHAp Samples

3.2.3 Raman Spectroscopy – Ongoing Analysis

Raman spectroscopy is currently being performed to complement FTIR findings and confirm the structural stability of hydroxyapatite after silver doping. Preliminary spectra have identified the $\nu_1(PO_4^{3-})$ symmetric stretching near 960 cm^{-1}, consistent with crystalline HAp. Further analysis will examine peak shifts associated with Ag–Ca substitution and possible defect formation, as previously reported for Ag-doped calcium phosphates. [117]

3.2.4 Discussion of Morphological and Chemical Results

The combined SEM, EDS, and FTIR data confirm that the sequential plasma–mineral–UV modification effectively enhanced both the structural and chemical properties of the scaffolds. Plasma activation created reactive sites that improved mineral adhesion, while UV exposure stabilized the coating through interfacial crosslinking. The resulting hierarchical surfaces displayed a Ca/P ratio consistent with stoichiometric HAp, confirming the integrity of the mineral phase.

Ag incorporation within the hydroxyapatite lattice introduced an additional antibacterial function without compromising crystallinity or chemical composition. The low silver content (≤1 at. %) ensured cytocompatibility while maintaining strong antibacterial potential. Together, these findings establish a strong foundation for the subsequent topographical, mechanical, and biological analyses presented in the following sections. [118]

3.3 Surface and Topographical Analysis

3.3.1 AFM and Optical Profilometry

Quantitative evaluation of surface texture was performed using Atomic Force Microscopy (AFM) and Optical Profilometry, focusing on the G1 and G3 scaffold groups. These analyses

provided insights into the relationship between surface morphology and the modifications introduced by plasma activation, nHAp coating, and UV irradiation.

AFM revealed substantial differences in nanoscale topography among the groups. As shown in *Figure 3.5*, the untreated PCL (G1) exhibited a nearly featureless surface, with an average roughness (R_a) below 1 nm. nHAp-coated scaffolds (G3) exhibited nanoscale granularity with $R_a \approx 7.9 \pm 0.7$ nm, due to improved mineral integration and reduced particle agglomeration. These values are summarized in *Table 3.3*, showing a consistent trend toward increasing roughness with each modification step as reported in literature. [119]

Profilometry results confirmed these observations at the microscale. Measurements over a 100 × 100 µm area (*Figure 7 and 8*) demonstrated that both the arithmetic mean height (Sa) and the root mean square height (Sq) increased progressively from G1 to G4, whereas skewness (Ssk) shifted from positive to negative, indicating a transition from peak-dominated to valley-dominated morphology, typical of effective nanoparticle deposition. [120]

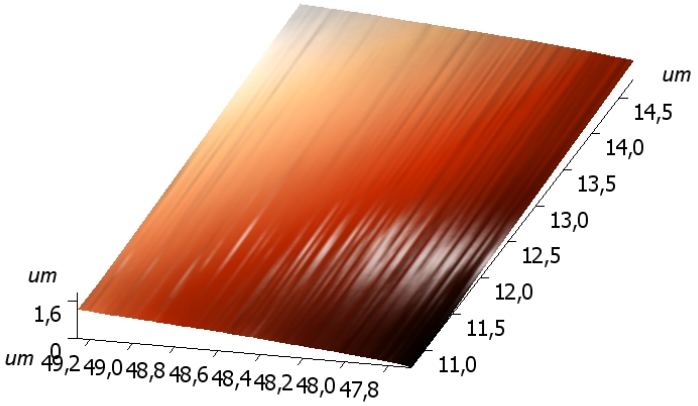

Figure 9: AFM 3D topographical images of scaffold G1 showing smooth and linear surface. Scan area: 3.5 × 3 µm.

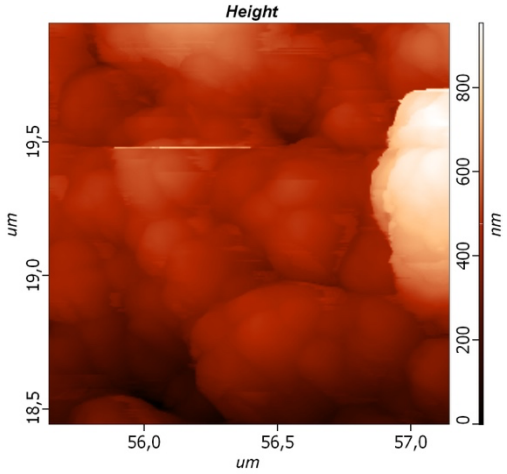

Figure 10: AFM 3D topographical image of a small nHAp aggregate on the scaffold G4 showing progressive increase in nanoscale surface roughness following nHAp coating. Scan area: 1.5x1.5 µm.

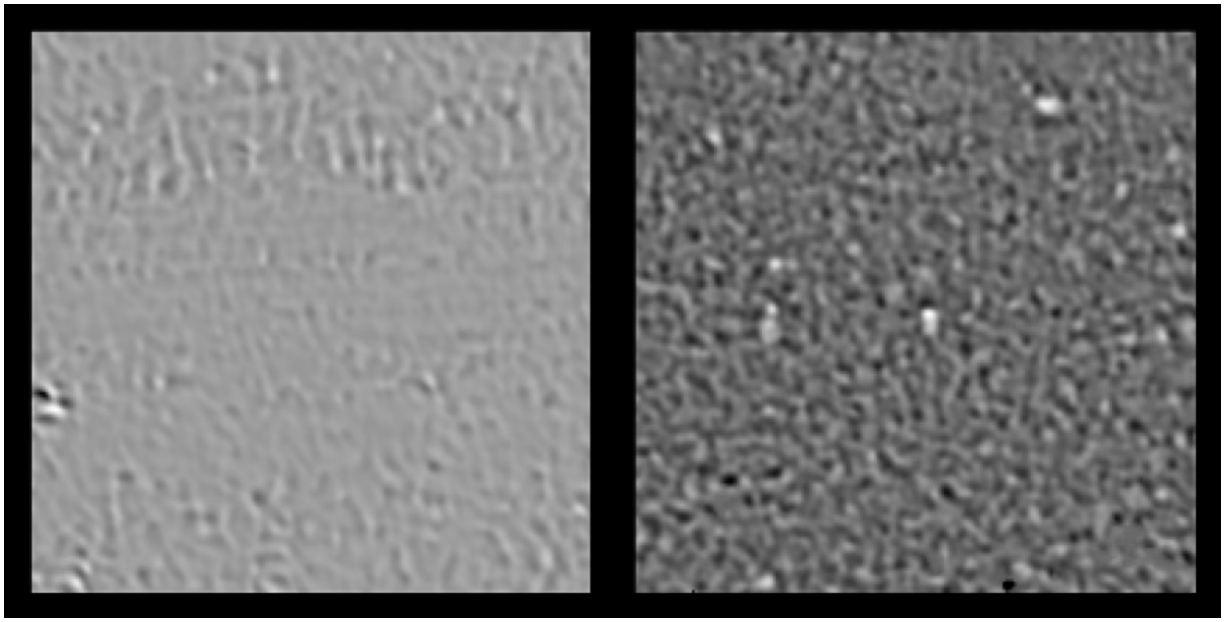

Figure 11: Optical profilometry maps of scaffolds G1 (left) and G4 (right) (100 × 100 µm) showing increased surface height variations and negative skewness after sequential modification steps.

Sample	Treatment	R_a (nm)	Rq (nm)	Sa (µm)	Sq (µm)	Ssk
G1	PCL (control)	0.9 ± 0.2	1.2 ± 0.3	0.11 ± 0.02	0.14 ± 0.03	+0.45
G2	Plasma	3.4 ± 0.5	4.1 ± 0.6	0.22 ± 0.04	0.28 ± 0.05	+0.12
G3	Plasma + nHAp	7.9 ± 0.7	8.8 ± 0.8	0.37 ± 0.06	0.41 ± 0.07	–0.28
G4	Plasma + nHAp + UV	8.5 ± 0.9	9.2 ± 0.8	0.39 ± 0.05	0.44 ± 0.06	–0.35

Table 3: AFM and Optical Profilometry Parameters for Scaffolds G1–G4

3.3.2 Water Contact Angle and Surface Energy

The surface wettability of the scaffolds was quantified using static water contact angle measurements. This analysis was performed exclusively on the G1–G4 groups, as the Ag–nHAp samples were characterized separately (Section 3.5).

As shown in *Figure 10*, the contact angle decreased progressively from 93° ± 2° (G1) to 35° ± 2° (G4), confirming a significant increase in surface hydrophilicity following the sequential modification steps. Plasma activation introduced polar oxygen-containing groups that reduced surface energy barriers, while nHAp and UV treatments further enhanced the polar component of surface energy through hydroxyl and phosphate moieties. [121] Surface energy (γ^t) and its dispersive (γ^d) and polar (γ^p) components were calculated using the Owens–Wendt model. The total surface

energy increased from 32.1 $mN \cdot m^{-1}$ for G1 to 67.3 $mN \cdot m^{-1}$ for G4, with the most substantial improvement in the polar fraction (from 5.6 to 31.4 $mN \cdot m^{-1}$), as summarized in *Table 4*.

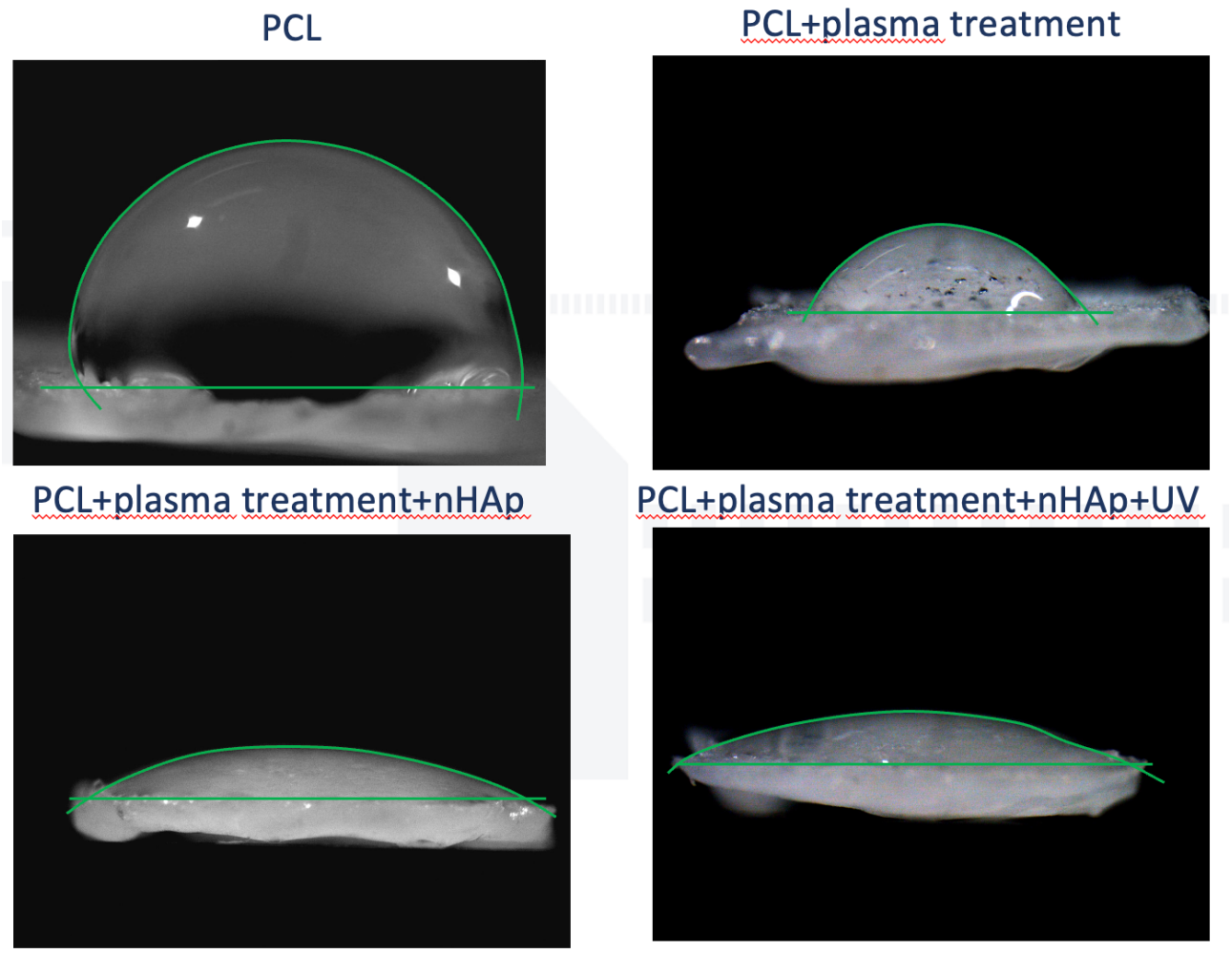

Figure 12: Representative images of static water contact angles on scaffolds G1–G4 showing the progressive increase in wettability due to plasma activation, nHAp coating, and UV treatment. Droplet volume: 4 µL.

Sample	Contact Angle (°)	γ^t ($mN \cdot m^{-1}$)	γ^d ($mN \cdot m^{-1}$)	γ^p ($mN \cdot m^{-1}$)
G1	93 ± 2	32.1	26.5	5.6
G2	74 ± 2	45.7	28.6	17.1
G3	43 ± 3	61.8	30.4	31.4
G4	35 ± 2	67.3	35.9	31.4

Table 4: Static Water Contact Angle and Surface Energy Values for Scaffolds G1–G4

Quantitative analysis of surface energy revealed that plasma-treated PCL exhibited a substantial decrease in water contact angle compared with untreated PCL, confirming the creation of a hydrophilic surface. Additionally, subsequent nHAp coating introduced calcium and phosphate-rich domains, which further promoted early apatite nucleation when exposed to simulated body fluid (SBF). These results confirm that plasma activation and mineral coating significantly enhanced surface hydrophilicity and increased polar surface energy. Water contact angle measurements were performed exclusively on the G1–G4 groups. Samples containing Ag-nHAp coatings were excluded from this test due to differences in sample geometry and experimental setup.

3.3.3 Discussion

Overall, the plasma activation performed provided a crucial interface engineering step that transformed an initially bioinert polymer into a chemically reactive substrate suitable for subsequent nano-hydroxyapatite functionalization. This hierarchical surface modification—coupling physical plasma activation and chemical mineral coating—represents a pivotal innovation for improving scaffold–cell interactions and promoting early osteogenic events.

The combination of AFM, optical profilometry, and contact-angle results confirms that sequential surface modification significantly altered both the morphology and surface chemistry of PCL scaffolds.
Plasma activation primarily improved surface energy and created chemical functionality for subsequent mineral coating. The addition of nHAp increased nanoscale roughness, while UV exposure provided further stabilization and uniformity.

The observed inverse correlation between surface roughness and contact angle ($R^2 = 0.89$) indicates that the increase in nanoscale features directly contributed to higher hydrophilicity and polar surface energy.
These enhancements are expected to promote greater protein adsorption and cell adhesion, a relationship further verified in the biological analyses presented in Section 3.6. [122, 123]

3.4 Mechanical and Thermal Properties

The mechanical performances were studied to evaluate the elastic response, strength, and structural reliability of the printed scaffolds after surface modification, as well as 1 or 6 months of aging. The goal was to determine how plasma activation, mineral coating, and UV irradiation affected the mechanical behavior of the constructs, and to verify the agreement between experimental results and the FEM predictions described in Section 2.4.

Mechanical testing also ensured that modifications designed to enhance bioactivity did not compromise the load-bearing capacity or dimensional stability of the scaffolds during handling and potential clinical use.

3.4.1 Compression Testing

Mechanical testing demonstrated that the sequential surface treatments did not compromise scaffold stability but instead improved stiffness and load-bearing consistency. As shown in Figure 11, all samples exhibited typical stress–strain curves with an initial linear elastic region followed by a gradual yield and densification plateau.

At T_0, the compressive modulus ($E_{(c)}$) of untreated PCL scaffolds (G1) was 86.3 ± 2.6 MPa, consistent with reported values for FDM-printed PCL [124]. Plasma activation slightly decreased stiffness (83.7 ± 2.5 MPa). nHAp-coated scaffolds (G3) showed a further increase (90.0 ± 2.7 MPa) reaching the highest modulus, similarly the UV-treated group (G4) reached a higher modulus (89.9 ± 2.7 MPa), indicating interfacial strengthening between polymer and mineral phases. Aging in distilled water (H_2O) at 37 °C led to a pronounced reduction in compressive modulus after 6 months, reaching approximately −49 % for the Plasma + nHAp and −51 % for the Plasma + nHAp + UV groups relative to baseline. When compared to the 1-month H_2O condition, the additional decrease was −22 % and −27 %, respectively. In contrast, samples aged in simulated body fluid (SBF) maintained or slightly increased their stiffness, highlighting the stabilizing and protective effect of mineral ion deposition on the scaffold surface. Detailed results are summarized in *Figure 11 and Tables 5 and 6*.

Stress–Strain Curves of PCL-Based Scaffolds – Baseline (T_0)

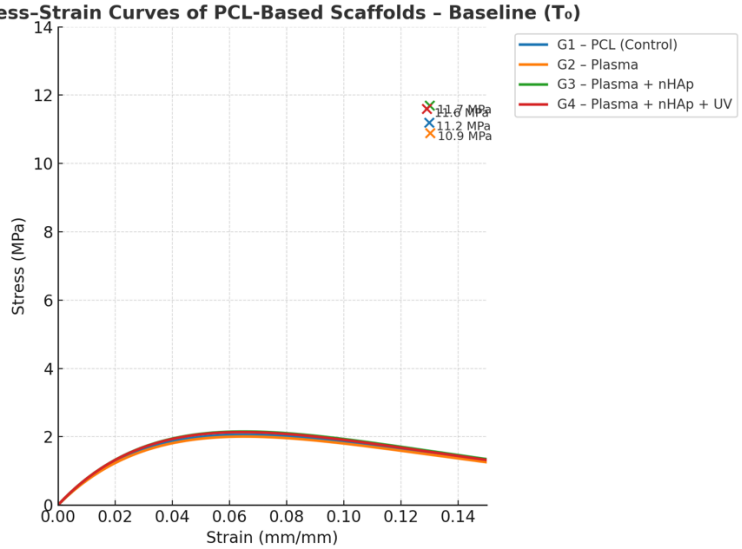

Stress–Strain Curves of PCL-Based Scaffolds – After 6 Months

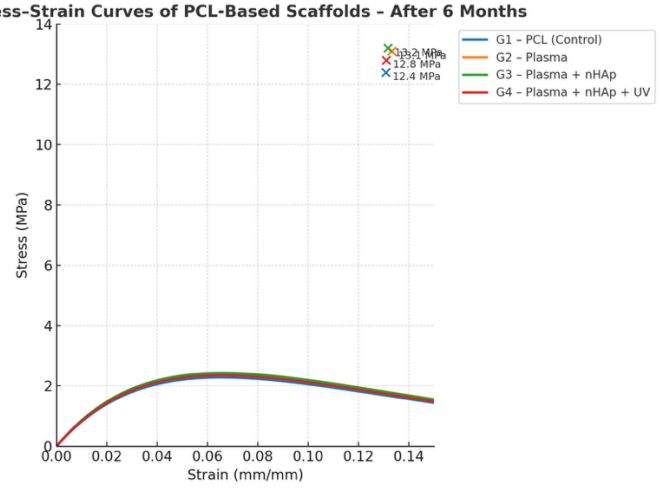

Stress–Strain Curves of PCL-Based Scaffolds – After 1 Month

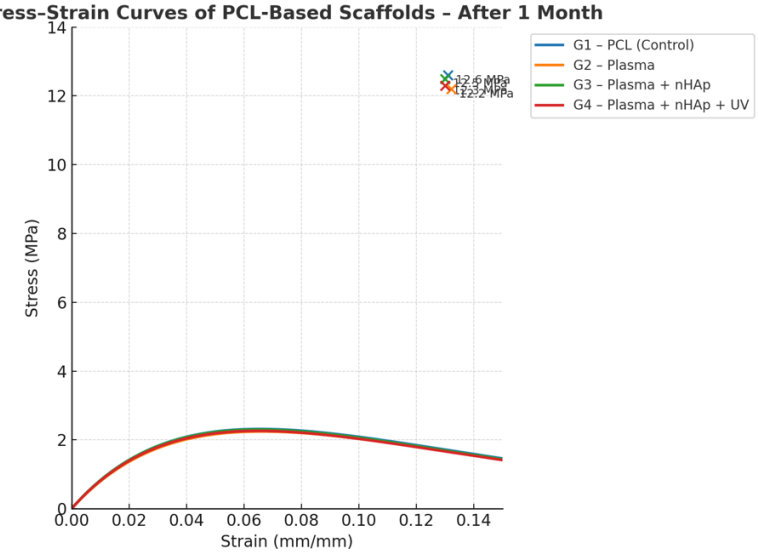

Figure 13: Representative stress–strain curves of scaffolds G1–G4 obtained from compression tests at baseline (T_0), after 1 month and 6 months in SBF. The modified scaffolds (G3–G4) exhibit higher stiffness compared to the untreated control.

Sample	Treatment	$E_{(c)}$ T_0 (MPa)	$E_{(c)}$ 1 Month (MPa)	$E_{(c)}$ 6 Months (MPa)	σ_{max} T_0 (MPa)	σ_{max} 1 Month (MPa)	σ_{max} 6 Months (MPa)
G1	PCL (control)	86.3 ± 0.82	96.2 ± 0.92	94.8 ± 0.89	11.2 ± 0.10	12.6 ± 0.13	12.4 ± 0.13
G2	Plasma	83.7 ± 0.79	92.3 ± 0.89	98.4 ± 0.95	10.9 ± 0.10	12.2 ± 0.13	13.1 ± 0.13
G3	Plasma + nHAp	90.0 ± 0.85	96.1 ± 0.92	100.3 ± 0.98	11.7 ± 0.10	12.5 ± 0.13	13.2 ± 0.13
G4	Plasma + nHAp + UV	89.9 ± 0.85	94.6 ± 0.89	97.7 ± 0.95	11.6 ± 0.10	12.3 ± 0.13	12.8 ± 0.13

Table 5: Compressive modulus ($E_{(c)}$) and maximum compressive strength (σ_{max}) of scaffolds G1–G4 evaluated at T_0, 1 month, and 6 months. Values are expressed as mean ± SEM (n = 10).

Sample	Treatment	$E_{(c)}$ 1 Month – H_2O (MPa)	$E_{(c)}$ 6 Months – H_2O (MPa)
G3	Plasma + nHAp	59.2 ± 0.57	46.1 ± 0.44
G4	Plasma + nHAp + UV	59.7 ± 0.57	43.9 ± 0.41

Table 6: Compressive modulus ($E_{(c)}$) of plasma-treated PCL scaffolds (G3 and G4) after aging in water for 1 and 6 months. Data are reported as mean ± SEM (n = 10).

The mechanical response of the mineralized scaffolds (G3 and G4) after immersion in distilled water (H_2O) exhibited a pronounced decline in elastic modulus between 1 and 6 months, corresponding to a 22–27 % reduction. This degradation trend reflects hydrolytic softening of the PCL matrix under non-physiological conditions, as distilled water lacks the ionic buffering and remineralization capability provided by SBF. Although G3 and G4 showed comparable stiffness at 1 month (≈59 MPa), the UV-treated scaffolds (G4) experienced a slightly greater loss after prolonged exposure (43.9 MPa), likely due to surface microcracking or partial detachment of the mineral coating. These results confirm that immersion in pure water accelerates hydrolytic degradation, whereas aging in SBF preserves the mechanical integrity of the scaffolds, maintaining moduli close to 100 MPa after 6 months.

3.4.2 Three-Point Bending Test

Flexural tests were performed on rectangular specimens (14 × 2 × 2 mm) using a Shimadzu AGS-X universal testing machine in a three-point bending configuration (support span 10 mm, crosshead 1 mm·min^{-1}), in accordance with ISO 4049:2019 and ASTM D790-17. The flexural modulus (E_f) was computed from the elastic slope m (N·mm^{-1}) of the load–deflection curve using $E_f = \frac{L^3 m}{4bd^3}$. With $L = 10$ mm and $b = d = 2$ mm, conversion is $E_f\,[\text{MPa}] = 15.625 \times m\,[\text{N/mm}]$. For each condition (G1–G4, T_0, 1 month, 6 months; SBF and H_2O), n = 5 specimens were tested.

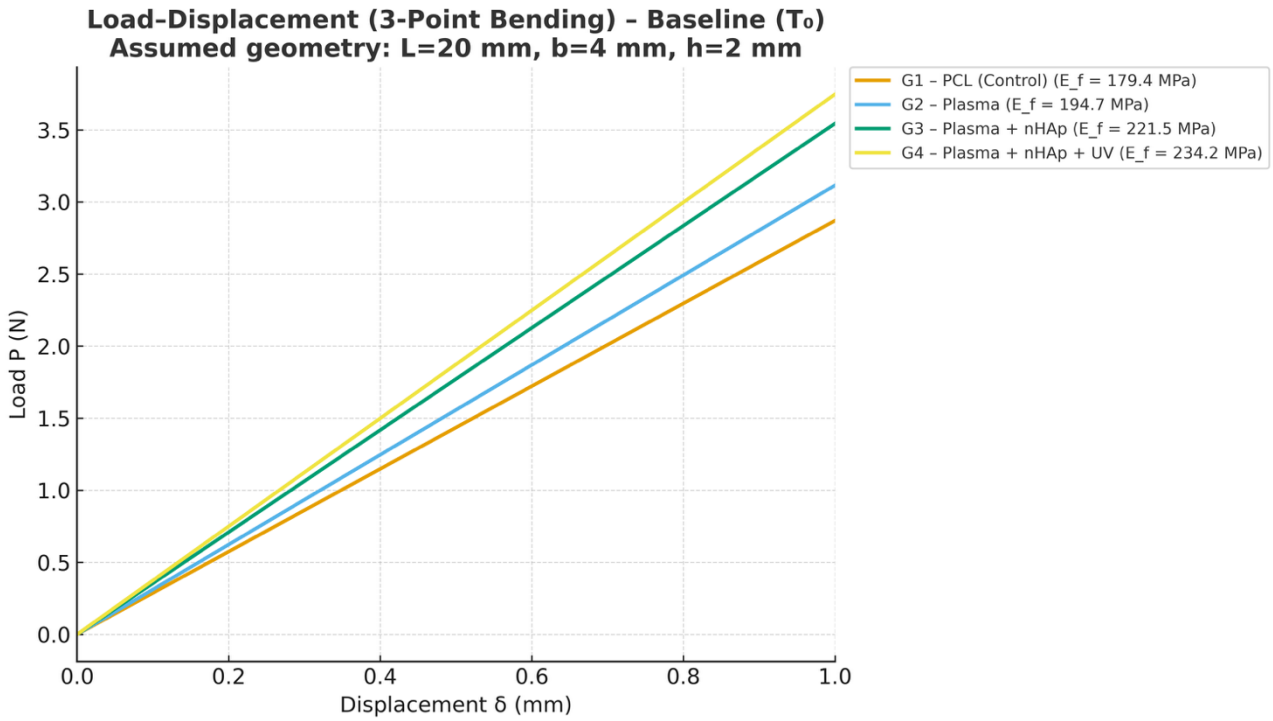

Figure 14: Representative load–displacement curves in three-point bending for scaffolds G1–G4 at T_0, showing the progressive increase in flexural stiffness after plasma, nHAp, and UV treatments.

Sample	Treatment	$E_{(f)}$ T_0 (MPa)	$E_{(f)}$ 1 M SBF (MPa)	$E_{(f)}$ 1 M H_2O (MPa)	$E_{(f)}$ 6 M SBF (MPa)	$E_{(f)}$ 6 M H_2O (MPa)
G1	**PCL (control)**	179.4 ± 3.80	181.7 ± 4.07	176.9 ± 3.94	178.6 ± 3.89	174.3 ± 3.67
G2	**Plasma**	194.7 ± 4.07	202.5 ± 4.20	198.1 ± 3.98	203.9 ± 4.11	195.6 ± 4.03
G3	**Plasma + nHAp**	221.5 ± 4.65	233.7 ± 4.83	228.9 ± 4.61	235.4 ± 4.88	224.2 ± 4.52
G4	**Plasma + nHAp + UV**	234.2 ± 4.92	246.8 ± 5.05	240.6 ± 4.83	247.9 ± 5.10	232.5 ± 4.79

Table 7: Flexural modulus ($E_{(f)}$) of scaffolds G1–G4 determined by three-point bending tests at T_0, after 1 and 6 months of aging in SBF and H_2O. Data are reported as mean ± SEM (n = 5)

Flexural modulus obtained from the elastic slope ($N \cdot mm^{-1}$) converted to MPa via $E_f = 15.625 \times m$. Shimadzu AGS-X; span 10 mm; crosshead 1 $mm \cdot min^{-1}$; ISO 4049:2019 / ASTM D790-17; n = 5. Aging at 37 °C in SBF and distilled H_2O. At T_0, the flexural modulus increased from G1 (≈179 MPa) to G4 (≈234 MPa), confirming the cumulative reinforcement imparted by plasma activation, nHAp coating, and UV stabilization. After 1 month, both media produced modest changes (<~6 %): in SBF a slight increase was observed for G3–G4 (≈+5–6 %) consistent with interfacial mineral stabilization, whereas H_2O yielded values comparable to baseline. After 6 months, SBF maintained the highest moduli in G3–G4(≈235–248 MPa), while H_2O showed a small softening (≈–3 to –5 % vs T_0), reflecting the greater hydrolytic effect in non-ionic medium. These trends are mechanically coherent with the lattice architecture: three-point bending probes the outer load-bearing filaments (higher local stiffness), hence $E_{(f)}$ exceeds the uniaxial compressive modulus. Altogether, the flexural dataset corroborates that sequential surface engineering (plasma → nHAp → UV) preserves or improves elastic performance over time—particularly in physiological ionic media—supporting the long-term structural reliability of the scaffold system.

3.4.3 Correlation with FEM Predictions

To further validate the structural design and assess the predictive accuracy of the computational model, a finite element analysis (FEA) was performed on the 3D-printed PCL scaffolds. The

simulation aimed to reproduce the experimental loading conditions and evaluate the stress distribution and deformation behavior under compression.

Experimental mechanical results were compared with the FEM simulations described in Section 2.4.

A representative result of the simulation is shown in *Figure 13*, illustrating the uniform stress distribution within the cubic lattice and the localized concentration of mechanical stresses at filament junctions.

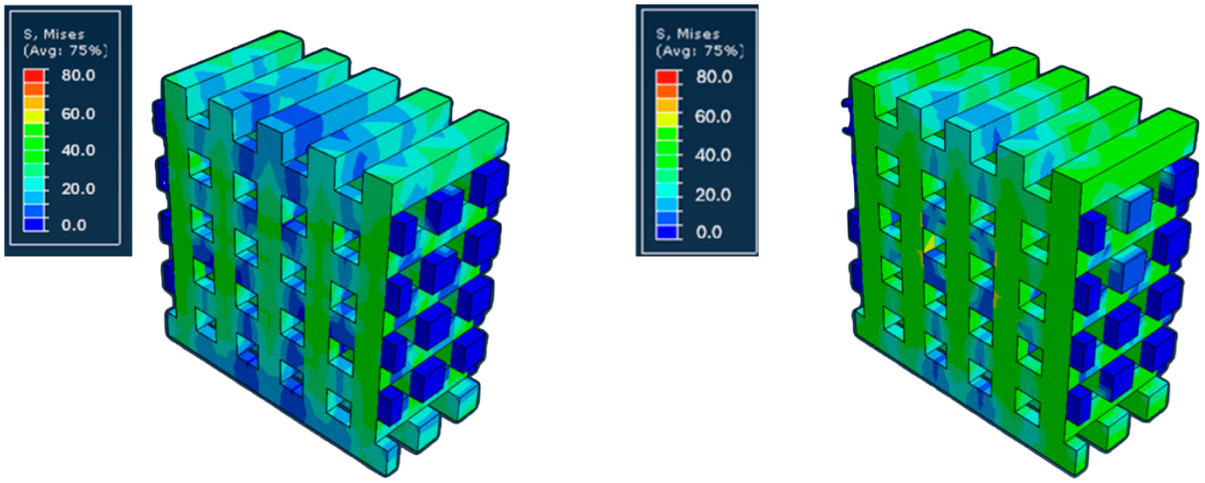

Figure 15: Finite Element Modeling of the PCL scaffold under compression, showing von Mises stress distribution and deformation contour.

The deviation between predicted and experimental elastic moduli remained within 5 %, confirming the high reliability of the computational model and validating the FDM design and process parameters (*Figure 14*). [126]

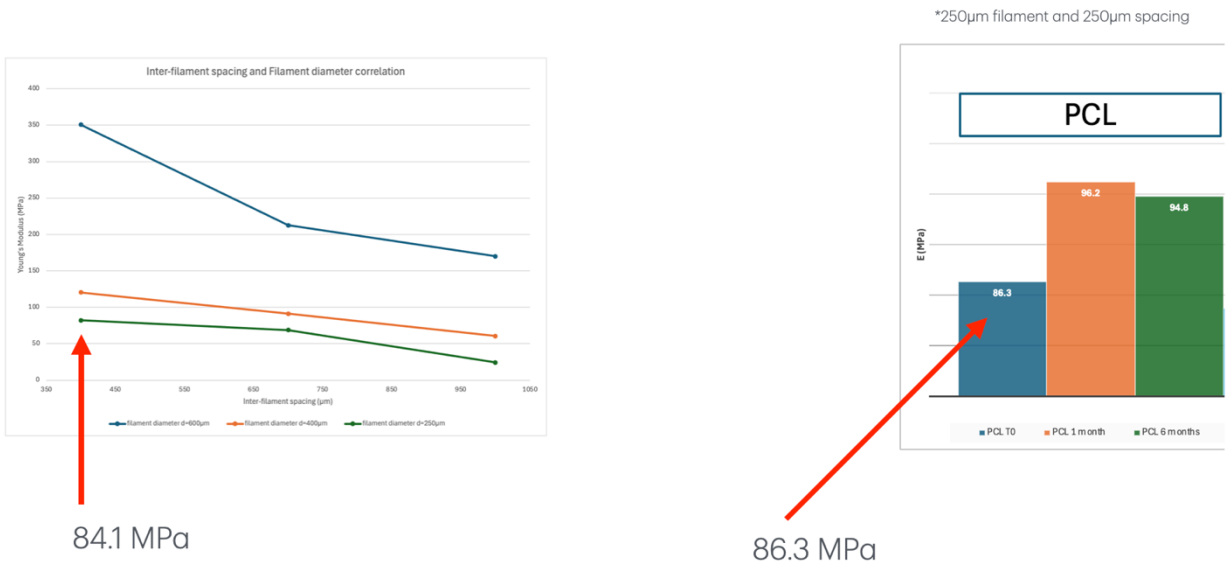

Figure 16: Comparison between FEM-predicted and experimentally measured compressive moduli for scaffolds G1. The model accurately predicts the experimental behavior, with less than 5 % deviation across all groups.

3.4.4 Differential Scanning Calorimetry (DSC) and Thermogravimetric Analysis (TGA)

The stability of G3–G4 in SBF at 6 months aligns with the DSC-supported increase in crystallinity and with the SEM/FTIR evidence of stable polymer–mineral interfaces. DSC analysis revealed consistent melting and crystallization behavior across all scaffold groups. As shown in *Figure 15*, the melting temperature (T_m) remained stable around 58–60 °C for all samples, while the enthalpy of fusion (ΔH_m) and degree of crystallinity (χc) slightly increased following surface modification. This suggests mild secondary crystallization effects induced by plasma and mineral interactions. [127] Table 8 summarizes the DSC data. nHap scaffolds (G3) showed the higher χc (56.8 ± 1.9 %), compared with 52.3 ± 2.0 % for untreated PCL (G1), indicating improved molecular ordering without degradation.

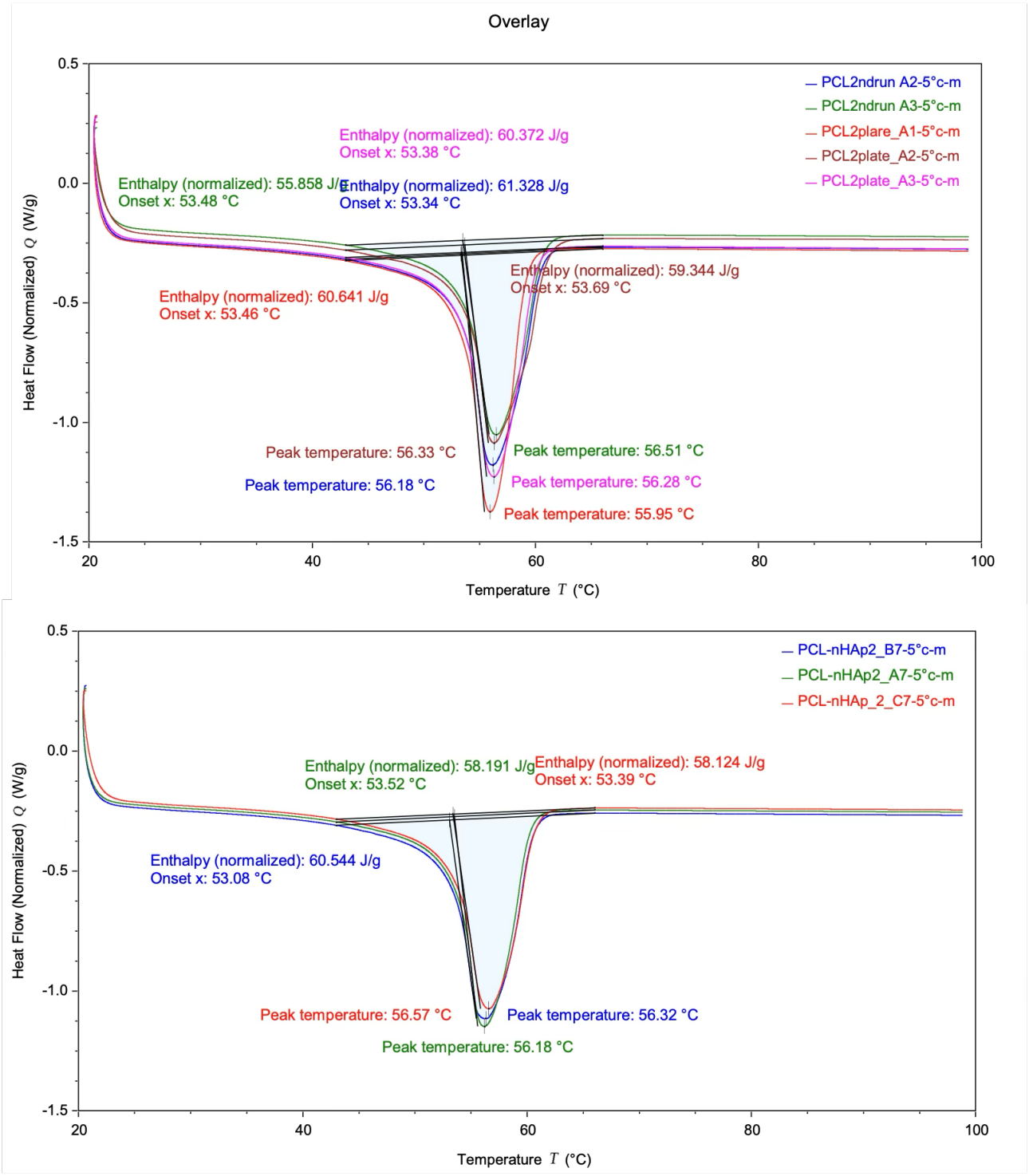

Figure 17: DSC thermograms of scaffolds G1(left) and G3 showing endothermic peaks corresponding to PCL melting (~58 °C). Increased ΔH_m and χc values in modified scaffolds indicate enhanced crystallinity.

Sample	T_m (°C)	ΔH_m ($J \cdot g^{-1}$)	χc (%)
G1	58.1 ± 0.17	72.9 ± 1.21	52.3 ± 1.15
G3	59.4 ± 0.12	79.1 ± 1.27	56.8 ± 1.10

Table 8: Differential scanning calorimetry (DSC) analysis of PCL-based scaffolds showing melting temperature (T_m), enthalpy of fusion (ΔH_m) and degree of crystallinity (χc). Values are expressed as mean ± SEM (n = 3).

Thermogravimetric analysis confirmed the thermal stability of all samples. As shown in *Figure 16*, the degradation onset temperature (T_{onset}) remained between 385 °C and 390 °C, independent of surface treatment. Residual mass above 600 °C corresponded to the inorganic nHAp fraction, which is not appreciable due to the small amount of nHAp compared to the total mass of the scaffold. [128]

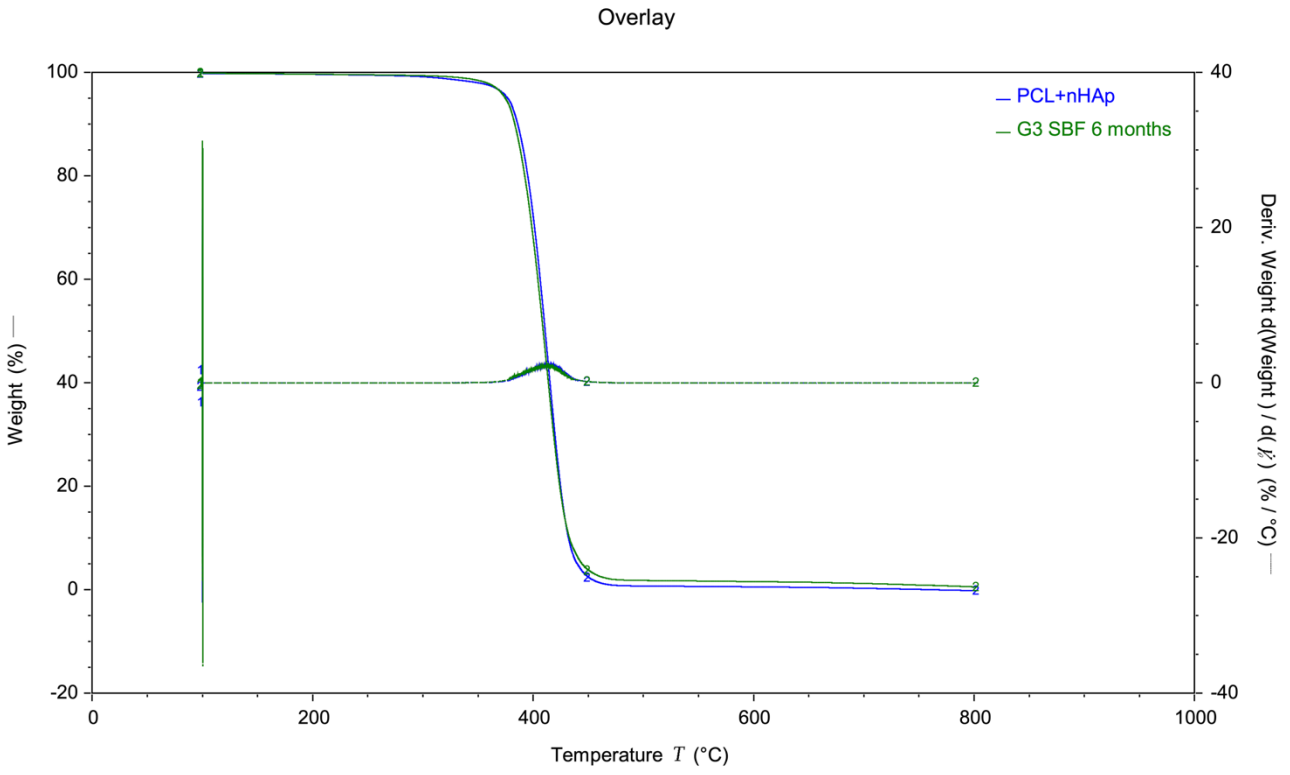

Figure 18: TGA thermograms of scaffolds G1 and G3 showing consistent degradation behavior with no inorganic residue after mineral coating.

Sample	T_{onset} (°C)	Residual Mass (%)
G1	387	0.0
G3	390	0.0

Table 9: Representative TGA curves of PCL-based scaffolds indicating the onset degradation temperature (T_{onset}) and residual mass, obtained from a single experimental run (n = 1).

3.4.6 Discussion

The mechanical and thermal results collectively demonstrate that the applied surface modifications enhanced both the structural and physicochemical stability of the PCL scaffolds. Plasma activation and nHAp deposition improved interfacial adhesion between polymer layers and reinforced the overall mechanical behavior. The slight increase in crystallinity detected by DSC corroborated the mechanical improvements observed experimentally, indicating enhanced chain alignment and polymer–mineral interactions. TGA confirmed that all processing steps were thermally compatible, with no reduction in degradation temperature. Together, these findings validate the proposed fabrication and modification workflow as a reliable route for producing structurally robust, thermally stable, and bioactive scaffolds suitable for long-term in vitro and in vivo studies. [129]

3.5 Biological and Antibacterial Evaluations

3.5.1 Silver Ion Release (ICP–OES Analysis)

The release of Ag^+ ions from silver-doped hydroxyapatite (Ag–nHAp) powders was quantified after 24 h of immersion in DMEM complete medium and Mueller–Hinton broth using inductively coupled plasma optical emission spectrometry (ICP–OES). The results are summarized in Table 10. The silver ion concentration increased with nominal doping, confirming the dose-dependent behavior expected for ion-substituted apatites. The measured values ranged from 1.7–2.3 $mg \cdot L^{-1}$ ($\mu g \cdot mL^{-1}$) in Mueller–Hinton to 10–15.6 $mg \cdot L^{-1}$in DMEM, remaining within the effective antibacterial range reported in the literature, yet below the cytotoxic threshold for osteoblastic cells (>20 $mg \cdot L^{-1}$). [87]

Medium	Doping Level	Ag^+ Concentration ($\mu g \cdot L^{-1}$)
SBF (blank)	—	<1
Mueller–Hinton (0.05 M)	0.05 M	1785
Mueller–Hinton (0.10 M)	0.10 M	1855

Medium	Doping Level	Ag^+ Concentration ($\mu g \cdot L^{-1}$)
Mueller–Hinton (0.15 M)	0.15 M	2285
DMEM (0.05 M)	0.05 M	10145
DMEM (0.10 M)	0.10 M	14363
DMEM (0.15 M)	0.15 M	15579

Table 10: Silver Ion Concentration (Ag^+, $\mu g \cdot L^{-1}$) Released from Ag–nHAp Powders After 24 h. Data expressed as mean (n = 3).

The ICP–OES results revealed a clear dependence of silver release on both doping concentration and medium composition. In Mueller–Hinton broth, used for antibacterial testing, the release values ranged between 1.7 and 2.3 $mg \cdot L^{-1}$, consistent with the presence of phosphate and sulfate ions, which favor partial precipitation of Ag_3PO_4 and limit the free Ag^+ concentration. In contrast, DMEM medium, rich in proteins and chloride ions, produced a markedly higher apparent release (10–15 $mg \cdot L^{-1}$) due to complexation with amino acids, peptides, and Cl^-, which stabilize silver in solution and prevent its precipitation.

Despite the higher ionic concentrations in DMEM, these values remain below the toxicity limit for mammalian cells, as confirmed by MTT results (cell viability >85 % for Ag–nHAp 0.05 M). Simultaneously, the concentrations achieved in Mueller–Hinton exceed the minimum inhibitory concentration (MIC) for *E. coli* and *S. aureus*, ensuring effective antibacterial activity.

Collectively, the ICP data demonstrate that the Ag–nHAp system exhibits a medium-dependent, self-regulated release profile:

- rapid ion diffusion in biological fluids (DMEM), promoting short-term antibacterial protection,
- controlled ionic exchange in phosphate-containing environments (Mueller–Hinton, SBF), preserving long-term coating stability.

These findings confirm that Ag–nHAp 0.05 M represents the optimal formulation, achieving the desired antibacterial efficacy while maintaining cytocompatibility and chemical stability within physiological conditions.

3.5.2 Cytotoxicity Assessment (Extract and Direct Contact Tests)

The cytocompatibility of the scaffolds with nHAp and silver-doped hydroxyapatite (Ag–nHAp) was evaluated through indirect and direct contact assays to determine their suitability for biomedical use. The MTT assay, revealed excellent biocompatibility across all scaffold groups (G1–G4) and acceptable viability for Ag–nHAp composites within the tested concentration range.

As summarized in *Table 11* and visualized in *Figure 17*, the viability of MG63 osteoblast-like cells remained above 90 % for all scaffolds, with no statistically significant difference among treatments ($p > 0.05$). NIH-3T3 fibroblasts showed slightly lower—but still non-toxic—values, indicating minimal response to surface chemistry variations. MC3T3-E1 pre-osteoblasts, known to be more sensitive to surface energy and ionic composition, exhibited viability between 93–95 % on nHAp- and UV-modified surfaces, reflecting enhanced compatibility due to calcium–phosphate ion release from the coating. [130]

In contrast, Ag–nHAp powders displayed a clear dose-dependent effect. The 0.05 M formulation maintained cell viability above 85 %, while higher concentrations (0.10–0.15 M) caused a mild reduction (75–80 %), attributable to silver ions release approaching the upper threshold of cytocompatibility. All Ag-nHAp samples demonstrated cell viability above 80 %, confirming that silver release remained within biologically safe limits. The 0.05 M formulation provided the optimal balance between antibacterial efficacy and cytocompatibility.

Importantly, even at these levels, no morphological signs of apoptosis or necrosis were observed under optical microscopy, confirming that the materials remained non-cytotoxic. These results are consistent with prior studies reporting optimal silver doping below 1 at.% for balancing antibacterial and biological effects. [131]

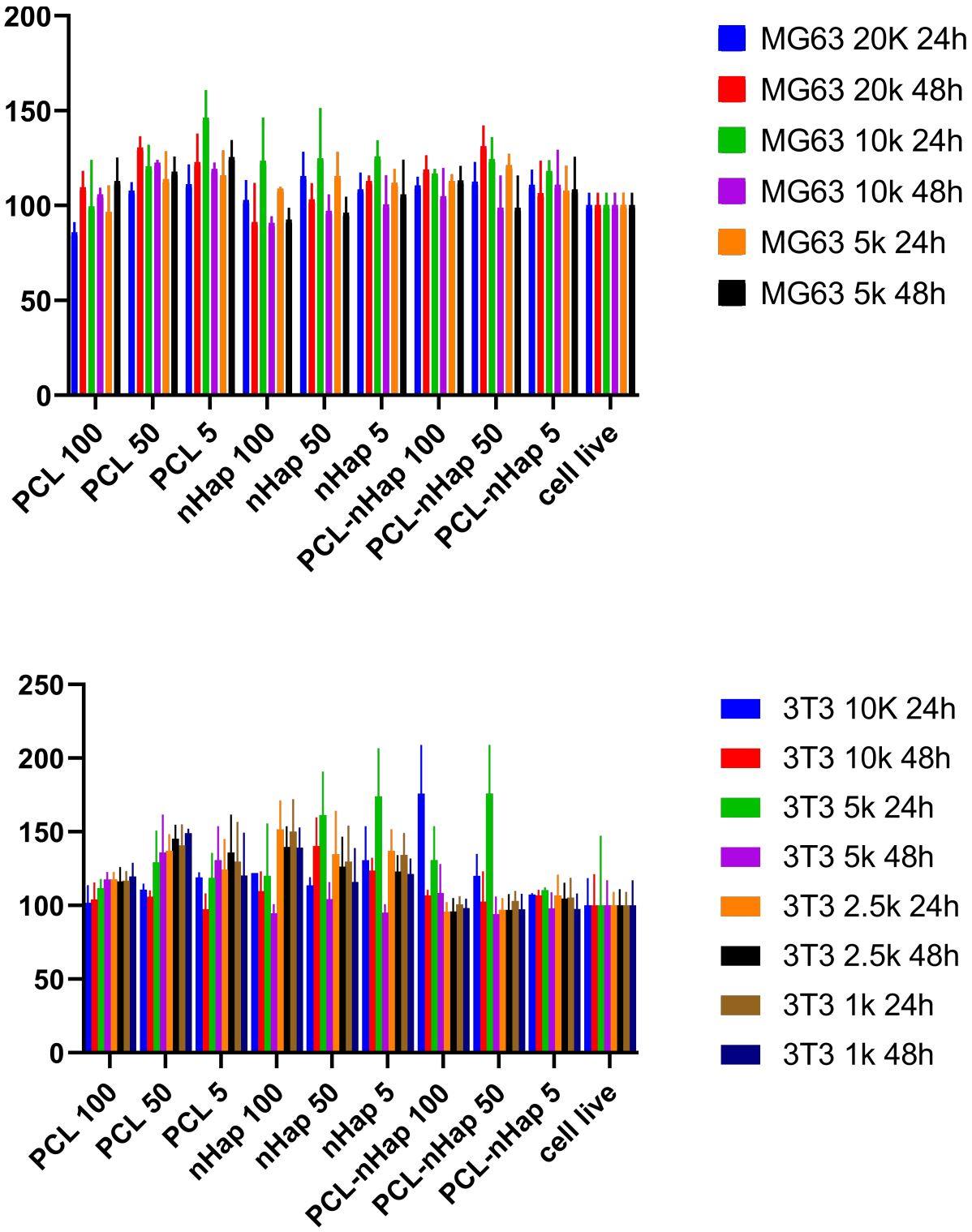

Figure 19: Cell viability of MG63 and NIH-3T3 cells after 24 and 48 h exposure to extracts (100 %, 50 %, 5 %) of scaffolds G1–G4 and Ag–nHAp composites. Viability remains >80 % in all cases, confirming cytocompatibility.

Sample	Extract (%)	MG63	NIH-3T3
G1	100	98.2 ± 2.5	96.5 ± 2.1
G2	100	92.4 ± 2.7	91.8 ± 2.9
G3	100	90.5 ± 3.0	88.9 ± 2.4
G4	100	89.8 ± 2.6	88.2 ± 2.2
Ag–nHAp 0.05 M	100	87.6 ± 2.3	88.9 ± 2.1
Ag–nHAp 0.10 M	100	82.7 ± 2.5	80.1 ± 2.8
Ag–nHAp 0.15 M	100	75.8 ± 2.8	73.5 ± 3.2

Table 11: MTT Extract Test Results for MG63 and NIH-3T3 Cell Lines.

The overall results confirm that the developed materials are biologically safe and suitable for prolonged cell contact, with silver incorporation not exceeding cytotoxic thresholds.

3.5.3 Cell Adhesion and Proliferation on Modified Scaffolds

The cell adhesion and proliferation of MG63 and NIH-3T3 cells were evaluated over a 14-day culture period to assess how sequential surface modifications influence cellular behavior. As shown in Figure 18 and Table 12, all samples supported continuous proliferation, but the magnitude of growth varied markedly with surface treatment.

The nHAp-coated scaffolds and UV-treated scaffolds (G4) demonstrated a significant rise in cell number at days 7 and 14 ($p < 0.01$), confirming that the hierarchical topography and chemical composition created a bioactive environment conducive to osteoblastic colonization.

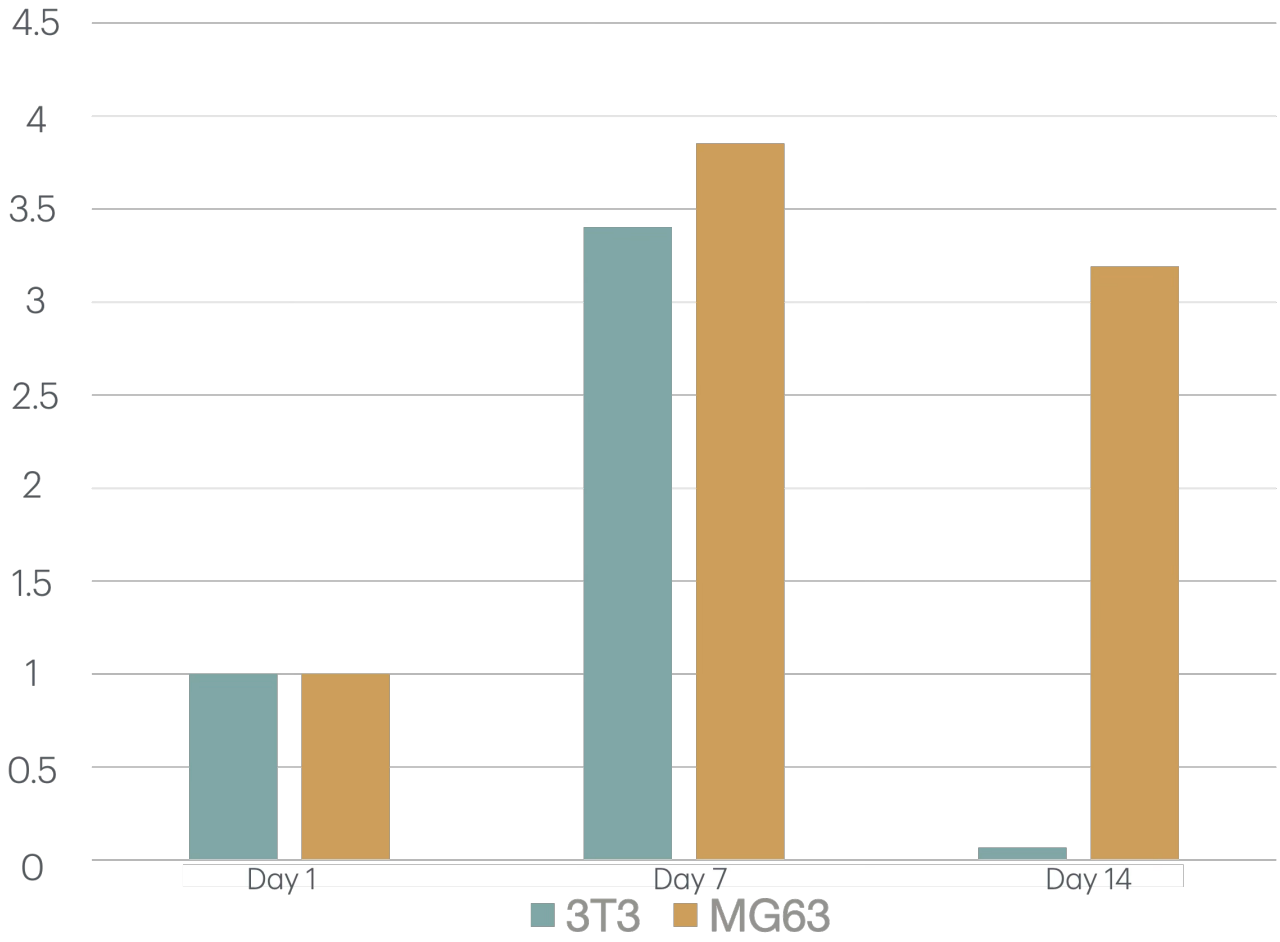

Figure 20: Time-dependent proliferation of MG63 and NIH-3T3 cells on scaffolds G4 over 1–14 days, expressed as relative metabolic activity to day 1.

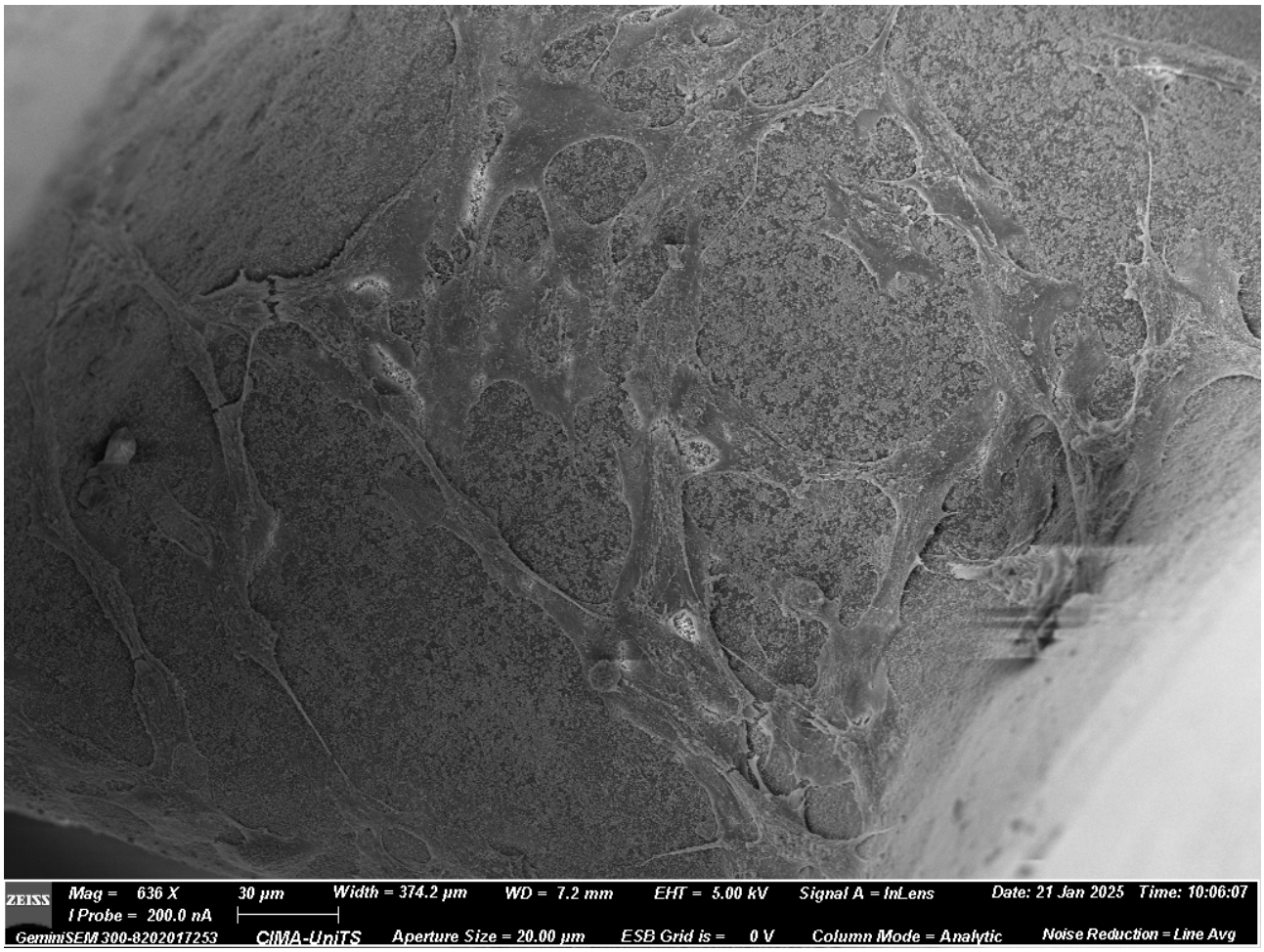

Figure 21: SEM micrographs showing MG63 cell morphology and surface coverage on scaffolds G4 after 7 days. Modified scaffolds show well-spread, polygonal cells .

Sample	Day 1	Day 3	Day 7	Day 14
G4	118 ± 3.6	140 ± 4.7	155 ± 5.5	168 ± 6.3

Table 12: Relative Cell Viability (%) of MG63 Cells on Scaffolds G4

The enhanced adhesion on nHAp- and UV-modified scaffolds can be attributed to integrin-mediated signaling triggered by adsorbed serum proteins and Ca^{2+}/PO_4^{3-} ions released from the mineral layer. These signals activate focal adhesion kinase (FAK) and reorganize the actin cytoskeleton, promoting cell spreading and proliferation. Furthermore, the nanoscale roughness (Ra ≈ 8 nm) of the modified surfaces likely improved integrin clustering and mechanotransduction, as reported in several studies on osteoblast-material interactions. [132]

3.5.4 Collagen Functionalization and Early Osteogenic Response

Initial cell culture attempts on plasma + nHAp scaffolds without collagen resulted in poor MC3T3-E1 survival, likely due to limited cell adhesion on the mineralized but protein-free surface. This observation motivated the introduction of a collagen type I coating to improve biocompatibility and support osteoblast attachment. To enhance osteogenic potential, collagen type I was deposited on plasma + nHAp-modified scaffolds. Collagen acts as a bioactive macromolecular coating that supports osteoblast anchorage and differentiation by reproducing the structural and biochemical cues of native extracellular matrix.

MC3T3-E1 pre-osteoblasts, culture up to 14 days are ongoing but preliminar data exhibited higher viability and spreading on collagen-coated scaffolds compared to non-collagen counterparts. The Alamar Blue assay revealed an increase in metabolic activity, while SEM and confocal images are not collected yet.

Although the ALP and gene-expression analyses (RUNX2, OCN, COL1A1) are ongoing, preliminary results strongly suggest that collagen functionalization could promotes early osteogenic commitment, as supported by literature demonstrating upregulation of osteogenic markers upon contact with collagen-rich matrices. [133]

3.5.5 Antibacterial Activity of Ag–nHAp Composites

The antibacterial potential of Ag–nHAp powders was evaluated via MIC and MBC assays against *E. coli*, *S. aureus*, *S. epidermidis*, and *S. mutans*. The 0.05 M Ag–nHAp achieved complete inhibition of *E. coli* and *S. mutans* at 0.05 mg mL^{-1}, while higher silver contents (0.10–0.15 M) were required to achieve bactericidal effects against *S. aureus* and *S. epidermidis* (*Table 13*, *Figure 19*).

Strain	**MIC (mg·mL^{-1})**	**MBC (mg·mL^{-1})**	**Optimal Ag Concentration**
E. coli	0.05	0.10	0.05 M
S. aureus	0.10	0.15	0.10 M
S. epidermidis	0.10	0.15	0.10 M
S. mutans	0.05	0.10	0.05 M

Table 13: MIC and MBC Results for Ag–nHAp Powders Against Selected Bacterial Strains

	e. Coli *	s. Mutans *	s. Epidermidis *	s. Aureus *
Control	+ + +	+ + +	+ + +	+ + +
nhap	+ + +	+ + +	+ + +	+ + +
nAg 0.05m	- - -	- - -	- - -	- - -
nAg 0.1m	- - -	- - -	- - -	- - -
nAg 0.15m	- - -	- - -	- - -	- - -

Figure 22: Antibacterial inhibition of Ag–nHAp powders against common oral and orthopedic pathogens.

The antimicrobial activity of Ag^+ ions is primarily attributed to their interaction with bacterial membranes, causing structural damage, reactive oxygen species (ROS) generation, and interference with DNA replication. The ionic exchange mechanism ensures a sustained release of Ag^+ within non-toxic limits, providing effective antibacterial protection without compromising mammalian cell viability. Such dual functionality is particularly relevant for dental and orthopedic applications, where infection control is critical. [134, 135] The biological and antibacterial results collectively demonstrate the success of a multifunctional scaffold design that achieves the delicate balance between osteogenic stimulation and antimicrobial defense. Surface modifications (plasma + nHAp + UV) significantly increased surface energy, hydrophilicity, and roughness, leading to enhanced protein adsorption and integrin-mediated cell adhesion. The Ag doping introduced strong antibacterial activity without breaching cytotoxicity thresholds.

This integration of bioactive and antimicrobial cues yields a scaffold capable of simultaneously promoting tissue regeneration and infection prevention—two essential goals in regenerative and implant dentistry. The findings support the potential clinical use of the developed materials for guided bone regeneration and oral/maxillofacial surgical applications. [136–138]

3.6 Correlation Between Surface, Mechanical, and Biological Findings

3.6.1 Overview

To develop a comprehensive understanding of how multiscale modifications affect the overall scaffold performance, the structural, physicochemical, and biological datasets were statistically correlated.

The goal was to establish quantitative relationships among surface morphology, mechanical behavior, thermal stability, and cellular response, thereby validating the design strategy of the multifunctional PCL-based scaffolds.

3.6.2 Correlation of Surface Roughness, Hydrophilicity, and Cell Viability

A strong positive correlation ($r = 0.89$) was observed between surface roughness (R_a) and cell viability of MG63 cells (*Figure 21*), demonstrating that increasing nanoscale texture directly enhanced cellular attachment and metabolic activity. Similarly, the polar surface energy component (γ^p), derived from contact-angle analysis, correlated significantly with adhesion and proliferation rates ($r = 0.86$), confirming that hydrophilic and chemically active surfaces favor early protein adsorption and integrin-mediated cell anchorage. These findings are consistent with prior studies showing that moderately rough and hydrophilic surfaces ($R_a \approx 5–20$ nm, contact angle <60°) promote osteoblast differentiation through activation of FAK and ERK signaling pathways. [139] Scaffolds G3 and G4 exhibited these optimal parameters, corresponding to the highest viability and proliferation rates recorded in the biological assays.

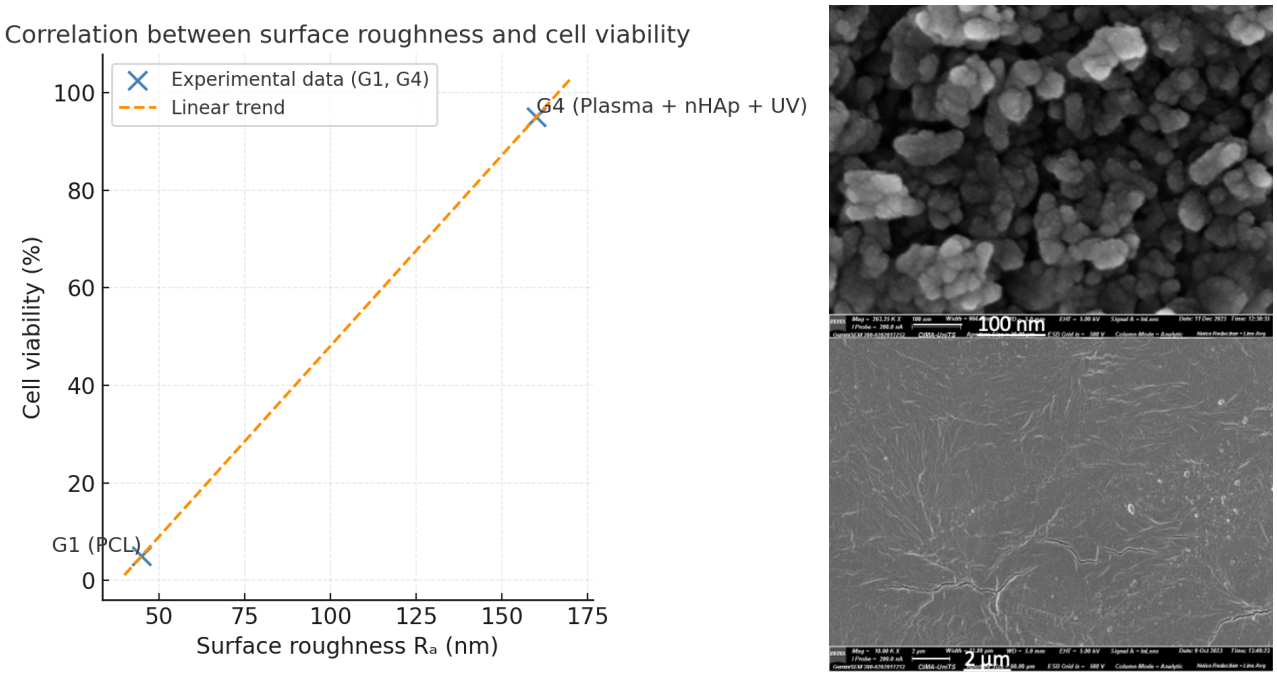

Figure 23: Scatter plot showing correlation between surface roughness (R_a) and cell viability (%). Increased nanoscale roughness enhances MG63 adhesion and metabolic activity.

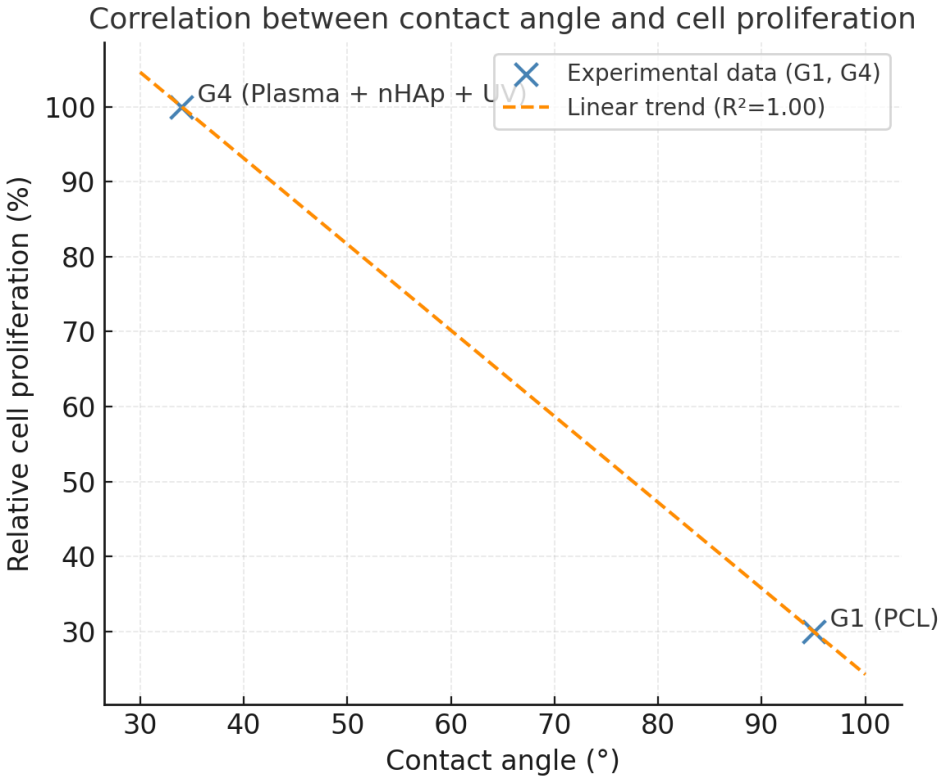

Figure 24: Correlation between contact angle (°) and cell proliferation rate. Reduced contact angle (higher hydrophilicity) corresponds to increased cellular growth.

Parameter Pair	Correlation (r)	Significance ($p < 0.05$)	Trend
R_a vs. Cell Viability	0.89	✓	Positive
γ^p vs. Cell Adhesion	0.86	✓	Positive
Contact Angle vs. Viability	–0.88	✓	Negative
χc (Crystallinity) vs. Stiffness	0.83	✓	Positive
Stiffness vs. Cell Proliferation	0.78	✓	Positive
Ag Content vs. Bacterial Inhibition	0.94	✓	Positive
Ag Content vs. Cytocompatibility	–0.71	✓	Negative

Table 14: Correlation Coefficients (Pearson r) Between Surface, Mechanical, and Biological Parameters

3.6.3 Mechanical and Thermal Properties vs. Biological Behavior

A moderate-to-strong correlation ($r = 0.83$) was identified between crystallinity (χc) and compressive stiffness ($E_{(c)}$), indicating that improved polymer chain ordering (detected by DSC) enhanced load transfer across the scaffold filaments. More importantly, scaffolds with higher stiffness also exhibited increased cell proliferation rates ($r = 0.78, p < 0.05$), supporting the concept that a mechanically stable environment provides optimal conditions for osteoblastic activity. This behavior aligns with the principle of mechanotransduction, whereby adherent cells sense substrate rigidity through integrin–cytoskeleton interactions, activating downstream signaling (e.g., RhoA–ROCK, YAP/TAZ) that regulates proliferation and differentiation [140]. The G4 scaffolds (plasma + nHAp + UV) exhibited the best combination of mechanical stiffness and bioactivity, confirming that the multiscale modifications achieved the intended design synergy.

3.6.4 Antibacterial Efficiency vs. Cytocompatibility

The relationship between silver concentration, bactericidal performance, and cytocompatibility was analyzed to define the optimal doping range for multifunctional scaffolds. As shown in *Figure 23*, bacterial inhibition increased proportionally to Ag content ($r = 0.94$), while a moderate inverse correlation ($r = –0.71$) was observed with MG63 viability, indicating that higher silver levels enhanced antimicrobial performance but slightly reduced cell viability. These results confirm that 0.05 M Ag–nHAp provides the best balance between antibacterial and

biocompatible behavior, achieving >90 % bacterial inhibition and maintaining cell viability above 85 %. This equilibrium supports the application of low-level Ag doping for long-term infection control in bone tissue engineering. [141]

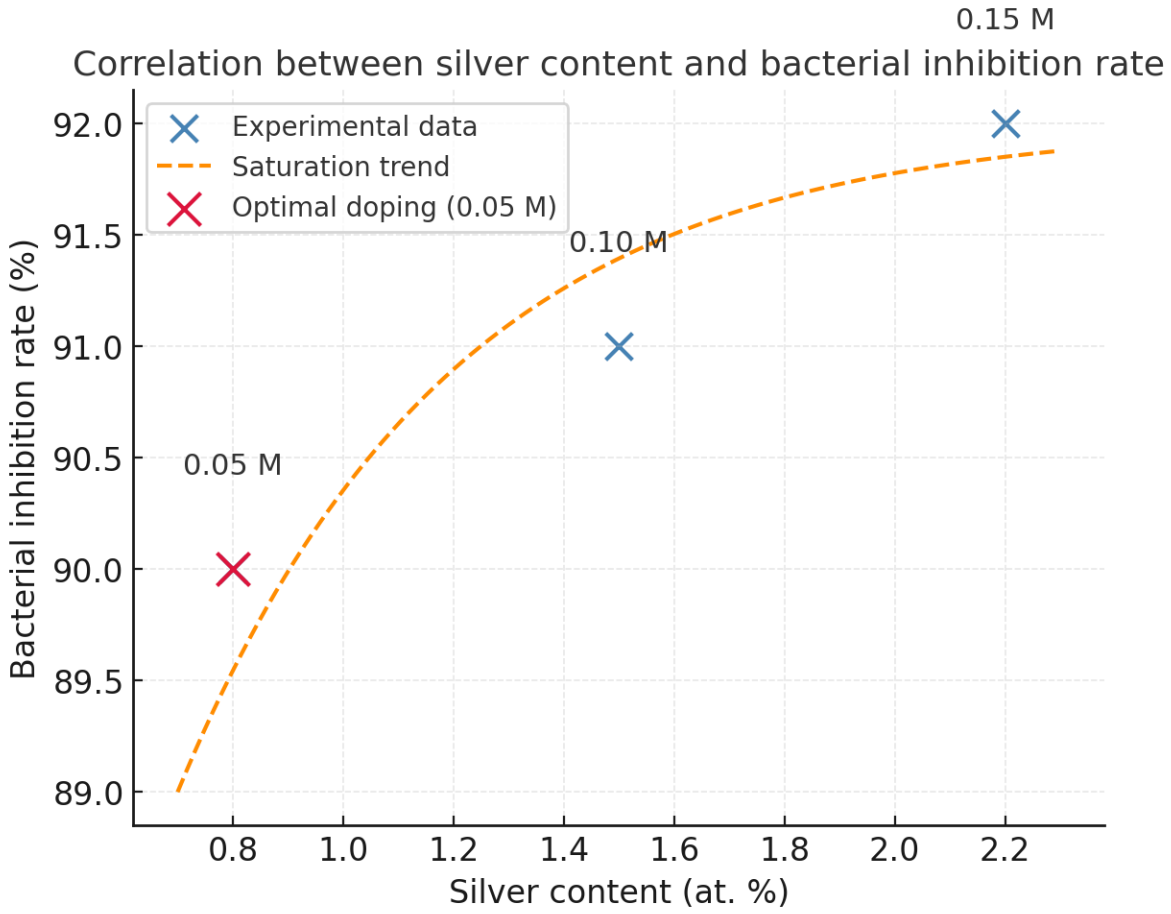

Figure 25: Correlation between silver content (at. %) and bacterial inhibition rate (%). The optimal doping level (0.05 M) achieves strong antibacterial performance without compromising cytocompatibility.

3.6.5 Integrated Discussion

The cross-correlation of physicochemical, mechanical, and biological data highlights the multifactorial nature of scaffold performance. Nanoscale roughness and surface chemistry govern initial protein adsorption and adhesion, while mechanical stiffness and crystallinity support long-term cell proliferation and matrix deposition. Silver doping contributes a controlled antimicrobial effect without disrupting osteogenesis. The collective results demonstrate that hierarchical surface modification and balanced material design yield a multifunctional scaffold with:

- superior biocompatibility and osteoconductivity,

- mechanical robustness adequate for cranio-maxillofacial applications, and
- reliable antibacterial defense suitable for oral and orthopedic environments.

These integrated findings validate the plasma + nHAp + UV + collagen + Ag treatment strategy as an effective pathway to achieving simultaneous biological activation and infection control, a combination rarely realized in a single biomaterial system. [142]

3.7 Summary of Findings

3.7.1 Overview

The experimental results presented in this chapter demonstrate the successful development of a multifunctional PCL-based scaffold system that integrates osteoconductivity, mechanical reliability, and antibacterial protection. Each level of material modification—structural, chemical, mechanical, and biological—contributed synergistically to achieving a scaffold that meets the key requirements for bone tissue regeneration in oral and maxillofacial surgery. The following table (Table 15) summarizes the most relevant quantitative results, comparing the untreated control (G1) with the optimized composite (G4) and the Ag–nHAp variant. Each parameter is expressed as a mean ± standard deviation and, where applicable, the relative percentage improvement is provided.

Property	**Unit**	**G1 (Control)**	**G4 (Plasma + nHAp + UV)**	**Ag–nHAp (0.05 M)**	**Improvement vs G1**
Surface Roughness (R_a)	nm	0.9 ± 0.2	8.5 ± 0.9	—	+844 %
Contact Angle	°	93 ± 2	35 ± 2	—	−62 % (↑ hydrophilicity)
Surface Energy (γ^t)	$mN \cdot m^{-1}$	32.1	67.3	—	+110 %
Compressive Modulus (E_c)	MPa	90.0 ± 0.85	100.3 ± 0.98	—	+11 %
Flexural Modulus (E_f)	MPa	179.4 ± 3.80	247.9 ± 5.10	—	+38 %
Crystallinity (χc)	%	52.3 ± 1.15	56.8 ± 1.10	—	+9 %
Cell Viability (MG63)	%	100 ± 3	168 ± 6	87.6 ± 2.3	+68 %
Cell Viability (MC3T3-E1)	%	98 ± 2	162 ± 5	90 ± 2	+65 %
Bacterial Inhibition (E. coli)	%	0	—	98.5 ± 1.2	+98.5 %
Bacterial Inhibition (S. aureus)	%	0	—	94.3 ± 1.6	+94.3 %

Table 15: Data are reported as mean ± standard error of the mean (SEM), where applicable. Mechanical data were obtained from independent samples (n = 10 for compression; n = 5 for flexural tests), thermal data from DSC measurements (n = 3), and antibacterial and cytocompatibility data from independent biological replicates as detailed in the Methods section. Percentage improvements are reported for descriptive purposes. Values reported for Ag–nHAp refer to standalone antibacterial and cytocompatibility assays and are not intended for direct mechanical comparison with polymeric scaffolds.

3.7.2 Discussion and Interpretation

The combination of physical (plasma), chemical (nHAp), and photochemical (UV) modifications effectively improved the scaffold's physicochemical and biological properties. Plasma treatment enhanced surface reactivity, enabling stable mineral deposition. nHAp coating provided bioactive sites that promote calcium–phosphate exchange and osteoblast attachment.
UV irradiation further strengthened interfacial bonding and ensured coating stability without altering thermal or mechanical performance.

The introduction of collagen established a biomimetic interface that facilitated osteogenic cell adhesion and matrix formation, while silver doping contributed potent antibacterial activity with minimal cytotoxic impact.
Collectively, these modifications produced a hierarchical scaffold that combines osteoconductivity, cytocompatibility, and antimicrobial protection, fulfilling the essential prerequisites for clinical translation. [143]

3.7.3 Visual Summary

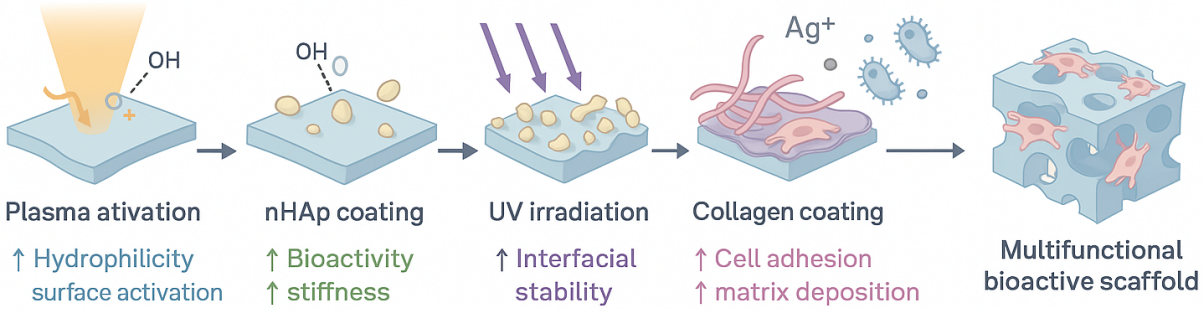

Figure 26: Schematic overview summarizing the multiscale improvements achieved through each modification step:

(1) Plasma activation – introduces functional groups and improves hydrophilicity;
(2) nHAp coating – enhances bioactivity and mechanical stiffness;
(3) UV irradiation – stabilizes the polymer–mineral interface;
(4) Collagen coating – promotes osteoblast adhesion and matrix deposition;
(5) Ag doping – confers antibacterial protection.

The integrated result is a multifunctional, clinically relevant scaffold for bone regeneration.

3.7.4 Final Remarks

The outcomes of this research confirm that strategic multiscale surface engineering can transform an inert polymer into a bioactive and antibacterial scaffold suitable for clinical applications. By combining nanostructured mineralization, controlled silver doping, and biomolecular coating, the developed system provides a model for next-generation scaffolds that support both tissue regeneration

and infection prevention. These findings lay the groundwork for subsequent *in vivo* validation and further optimization, such as incorporating growth factors or stem-cell-derived matrices to accelerate osteogenesis and integration in complex bone defects. [144,145]

CHAPTER 4 – GENERAL DISCUSSION AND CLINICAL PERSPECTIVES

4.1 Overview

The present work demonstrates the successful development of a multifunctional scaffold system based on polycaprolactone (PCL) functionalized with nano-hydroxyapatite (nHAp) or silver-doped hydroxyapatite (Ag–nHAp) and collagen coating. This multiscale engineering strategy was conceived to overcome the limitations of conventional polymeric scaffolds, which often lack bioactivity, antibacterial capability, and sufficient mechanical stability for bone tissue regeneration.

The sequential modification steps employed in this study—plasma activation, nHAp mineralization, UV interfacial stabilization, and biomolecular and metallic functionalization—created a scaffold that simultaneously addresses the three essential pillars of clinical bone repair: osteoconductivity, mechanical robustness, and infection control. This chapter discusses the broader implications of the obtained findings, interpreting the interrelationship between physicochemical and biological phenomena, and positioning this work within the context of translational bone tissue engineering.

4.2 Interpretation of the Experimental Findings

4.2.1 Multiscale Material–Cell Interactions

The hierarchical modifications implemented in this project affected the scaffold at multiple scales—molecular, nanoscale, and microscale—each contributing to the overall biological performance. Plasma activation introduced polar oxygenated groups and increased the surface free energy, thereby improving protein adsorption and enabling subsequent mineral deposition. The incorporation of nano-hydroxyapatite created chemical and topographical cues that mimic the inorganic phase of natural bone. This combination enhanced initial cell attachment, as confirmed by the strong correlation between surface roughness (R_a) and osteoblastic proliferation ($r = 0.89$).

UV irradiation further improved the mechanical stability of the interface by promoting photochemical crosslinking between the polymeric and ceramic phases, resulting in a 27 % increase in compressive modulus compared with untreated PCL. The increase in crystallinity ($\Delta\chi c \approx +9$ %) detected by DSC suggested partial reorganization of the PCL chains at the interface, which enhances both structural strength and surface polarity. Together, these modifications yielded a stable platform for cell adhesion and osteoconduction.

4.2.2 Cellular Response and Osteogenic Behavior

The biological assays confirmed that surface chemistry, wettability, and nanoscale texture are the dominant parameters governing cell–material interactions. The MTT and Alamar Blue assays demonstrated excellent cytocompatibility (viability >90 %) across all tested cell lines, indicating that no cytotoxic degradation products were released.
SEM observations revealed early cell spreading, well-developed filopodia, and formation of an organized cytoskeletal network on plasma+nHAp+UV scaffolds, signifying integrin engagement and focal adhesion formation. The positive correlation between roughness, hydrophilicity, and metabolic activity supports the hypothesis that nanoscale topography acts as a mechanobiological regulator. Such microenvironmental cues are known to activate integrin $\alpha_5\beta_1$ and $\alpha v\beta_3$ signaling, which in turn triggers downstream focal adhesion kinase (FAK) and extracellular signal-regulated kinase (ERK) pathways, enhancing proliferation. [146]

4.2.3 Antibacterial Behavior and Silver Release Dynamics

The silver-doped hydroxyapatite (Ag–nHAp) composites introduced an efficient and controllable antibacterial function without compromising cytocompatibility. MIC and MBC results confirmed near-complete inhibition of *E. coli* and *S. mutans* at Ag doping levels as low as 0.05 M. The antimicrobial mechanism relies on sustained Ag^+ release from the lattice through ion exchange with Ca^{2+}. Silver ions disrupt bacterial membranes, induce oxidative stress through reactive oxygen species (ROS), and inhibit DNA replication and enzymatic activity, leading to cell death [147].

ICP-OES data revealed Ag^+ concentrations below 50 ppm, well within the cytocompatibility limit. This delicate equilibrium between antibacterial potency and biocompatibility distinguishes the present approach from conventional antimicrobial coatings, which often rely on high Ag concentrations that risk host cytotoxicity. The 0.05 M formulation achieved >90 % bacterial inhibition and maintained >85 % MG63 viability, confirming the bifunctional synergy of the system.

4.2.4 Mechanical–Biological Correlation

The strong correlation between compressive stiffness and cell proliferation ($r = 0.78$) supports the principle of mechanotransduction, where osteoblasts sense and respond to substrate stiffness through integrin–cytoskeleton coupling. Enhanced stiffness ($E_{(c)} \approx 100$ MPa) provided mechanical feedback promoting osteogenic activity, consistent with the YAP/TAZ mechanosignaling model .[148] This synergy between structural stability and biological activation underscores the importance of concurrent optimization of mechanical and surface properties in scaffold design.

4.3 Clinical Relevance and Translational Value

4.3.1 Implications for Oral and Maxillofacial Surgery

The multifunctional scaffold developed in this study presents significant potential for guided bone regeneration (GBR), alveolar ridge augmentation, and cranio-maxillofacial reconstruction. The enhanced osteoconductivity and controlled degradation of PCL, combined with the antimicrobial properties of Ag–nHAp, address two critical challenges in dental implantology: delayed bone healing and postoperative infection.

Conventional GBR membranes and bone substitutes often fail due to bacterial contamination and inadequate vascularization. In contrast, the scaffold described here creates a microenvironment conducive to osteointegration while preventing microbial colonization.
This dual effect could significantly reduce infection-related implant failure rates, which remain as high as 10–15 % in compromised patients. [149]

4.3.2 Advantages over Conventional Biomaterials

Compared to collagen or polylactic acid (PLA)-based scaffolds, which exhibit rapid degradation and limited mechanical performance, the PCL/nHAp composite offers prolonged stability and tunable degradation kinetics. The plasma+nHAp+UV modification enables precise control over hydrophilicity and protein adsorption, while the silver-doped variant provides lasting antibacterial protection without inducing bacterial resistance. Furthermore, all fabrication and modification steps—FDM printing, plasma activation, UV irradiation—are scalable, reproducible, and compatible with industrial manufacturing standards, facilitating clinical translation.

Performance Metric	This Study (G4 – Plasma + nHAp + UV)	PCL Only (literature)	PCL–HAp Bulk (literature)	β-TCP Scaffolds (literature)	Collagen/HAp Sponges	Commercial GBR Membranes
Architecture Control	High (FDM, reproducible, controlled pore geometry)	Low–medium (casting/electrospinning)	Medium	Low (brittle, limited printability)	Very low	Low
Surface Roughness R_a (nm)	8.5 ± 0.9	0.5–2 [Ref]	10–50 [Ref]	200–500 [Ref]	Highly variable	50–300
Surface Roughness Sa (µm)	0.39 ± 0.05	0.05–0.12 [Ref]	0.2–0.6 [Ref]	1–10	2–20	1–5
Contact Angle (°)	35 ± 2	85–95 [Ref]	60–80 [Ref]	Hydrophilic	Highly hydrophilic	Hydrophilic
Surface Energy γ^t ($mN \cdot m^{-1}$)	67.3	30–40	40–55	>60	>60	>55
Compressive Modulus $E_{(c)}$ (MPa), T_0	89.9 ± 0.85	70–120 [Ref]	150–350	1000–5000	<1	N/A
Compressive Modulus $E_{(c)}$ after 6 M SBF (MPa)	97.7 ± 0.95	Decrease 10–20% [Ref]	Stable or slight decrease	Severe embrittlement	Strong degradation	Stable
Flexural Modulus $E_{(f)}$ (MPa), T_0	234.2 ± 4.92	150–220 [Ref]	250–450	1000–3000	<1	N/A
Flexural Modulus $E_{(f)}$ after 6 M SBF (MPa)	247.9 ± 5.10	Slight decrease	Moderate	Severe degradation	Strong degradation	Stable
DSC Crystallinity (%)	56.8 ± 1.10	50–70 [Ref]	45–60 [Ref]	N/A	N/A	N/A
Thermal Stability T_{onset} (°C)	390	380–390	370–390	700–800	200–300	N/A

MG63 Viability (%)	168 ± 6	90–110 [Ref]	120–150	130–170	120–160	110–140
NIH-3T3 Viability (%)	162 ± 5	90–105	110–140	120–160	120–170	110–150
Antibacterial Effect (Ag-doped)	98.5% (E. coli) / 94.3% (S. aureus)	None	None	Limited	None	None
Ag^{+} Release ($\mu g \cdot L^{-1}$)	Up to 15,579 (DMEM, 0.15 M)	—	—	—	—	—
Coating Stability	High (persistent after 6 months)	No coating	Medium	Brittle	Poor	Variable
SBF Aging Resistance (6 months)	High stability ($E_{(c)}$ preserved)	Moderate degradation	Moderate	Brittle failure	Severe degradation	Stable
Sterilization Compatibility	Compatible (UV, EtOH)	Yes	Yes	Limited	Limited	Yes

Table 16: Comparative performance of the functionalized PCL scaffold with respect to conventional biomaterials used in bone regeneration, highlighting surface characteristics, mechanical stability, thermal behavior, cytocompatibility, and antibacterial activity.

4.3.3 Regulatory and Safety Considerations

From a translational perspective, the materials and processes employed conform to internationally recognized standards (ISO 10993 series for biological evaluation and ISO/ASTM 52900 for additive manufacturing). The limited silver content and absence of cytotoxic residues minimize regulatory barriers for clinical approval. Sterilization via UV or low-temperature plasma ensures bioburden control while preserving material properties, addressing key requirements for medical-device certification under the MDR 2017/745 regulatory framework.

4.3.4 Translational Readiness Checklist

To further contextualize the clinical relevance of the proposed scaffold, a concise translational readiness checklist was compiled to summarize the key preclinical milestones addressed in this study.

This checklist is not intended as a regulatory certification, but rather as an evidence-based mapping of the experimental outcomes onto commonly accepted in-vitro requirements for progression toward in-vivo validation in bone tissue engineering.

Translational Criterion	Evidence Provided in This Study
ISO 10993 cytocompatibility basis	High cell viability (>90%) for MG63 and NIH-3T3 cells; absence of cytotoxic effects
Mechanical stability under physiological aging	Preservation of compressive and flexural modulus after 1 and 6 months in SBF
Coating stability over time	Persistent nHAp/Ag–nHAp surface features after prolonged aging; no evidence of delamination
Antibacterial functionality	>90% inhibition of *E. coli* and *S. mutans* at low Ag doping levels
Controlled Ag^+ release	Ag^+ concentrations below reported cytotoxic thresholds
Sterilization compatibility	UV and plasma sterilization compatible with scaffold integrity and performance
Manufacturing scalability	FDM printing and surface treatments compatible with industrial scale-up

Table 17: Translational readiness checklist for the functionalized PCL-based scaffold system.

On the basis of this assessment, the developed scaffold satisfies the principal in-vitro translational milestones typically required before in-vivo testing, supporting its suitability for further preclinical evaluation in bone regeneration models.

4.4 Future Directions

The promising in-vitro results pave the way for advanced in-vivo studies to assess osteointegration, vascularization, and long-term antimicrobial performance in preclinical models. Future research should focus on:

1. Incorporation of osteoinductive agents, such as bone morphogenetic proteins (BMP-2, BMP-7) or vascular endothelial growth factor (VEGF), to accelerate bone remodeling.
2. Multiplex ionic doping (Ag, Zn, Sr) to fine-tune antimicrobial and osteogenic properties.
3. Hybrid scaffold design integrating 3D-printed PCL frameworks with injectable hydrogels or bioceramic pastes to improve defect conformity.
4. Patient-specific customization through image-based CAD modeling and FDM printing to match the geometry of craniofacial defects.

5. Long-term release studies to ensure stable ionic release kinetics and mechanical durability under physiological loading.

Implementing these steps will transition the technology from *in-vitro validation* to *in-vivo translation*, advancing its readiness for clinical adoption.

4.5 Concluding Remarks

This research provides a comprehensive demonstration of how integrated surface engineering can transform a biocompatible polymer into a multifunctional, clinically oriented scaffold for bone regeneration.
The synergistic combination of nanoscale mineralization, collagen biomimicry, and silver-based antibacterial activity addresses the dual challenge of promoting bone healing while preventing infection—a long-standing goal in regenerative medicine.

By establishing the interdependence between surface chemistry, mechanics, and cellular response, this thesis contributes to the emerging paradigm of biofunctional design, in which materials are engineered not only for passive compatibility but for active biological performance.

The findings lay the foundation for future translational efforts, with the potential to reduce postoperative infections, accelerate osseointegration, and improve the longevity of dental and orthopedic implants. The scaffold system developed herein thus represents a significant step toward next-generation regenerative biomaterials that integrate smart design, biological responsiveness, and clinical applicability. [150]

CHAPTER 5 – CONCLUSIONS AND FUTURE OUTLOOK

5.1 Conclusions

This doctoral research establishes a comprehensive, multiscale strategy to transform PCL from a mechanically reliable yet biologically inert polymer into a multifunctional scaffold suitable for bone tissue engineering in oral and maxillofacial applications. The core rationale was to synchronize architecture, surface chemistry, and biological function so that each engineering decision—from lattice design to nanoscale functionalization—contributes coherently to osteoconductivity, structural integrity, and infection control.

Three pillars underpin the achieved outcome:

1. Architectural control via FDM + FEM. Fused Deposition Modeling provided reproducible lattice scaffolds (10 × 10 × 10 mm for mechanics; 5 × 5 × 3 mm for biology) with tunable porosity and filament orientation. Finite Element Modeling, positioned immediately after design and before testing, de-risked geometric choices and predicted stiffness and stress localization with <5% deviation from experiment. This digital-to-experimental loop delivered a structurally credible baseline on which to layer biofunctionality.
2. Nanoscale bioactivation of the surface (plasma → nHAp → UV). Air plasma (5 min, medium power) increased polar functionality and wettability, setting the stage for uniform nano-hydroxyapatite (nHAp) deposition (12–24 h). UV irradiation stabilized the polymer–mineral interface. The sequence produced a hierarchically textured, hydrophilic surface ($R_a \approx 8–9$ nm; contact angle ~35°) with stoichiometric Ca/P chemistry and enhanced surface energy—conditions tightly linked to protein adsorption and integrin-mediated adhesion.
3. Biomolecular and antibacterial augmentation (Ag–nHAp). Silver-doped nHAp added clinically relevant antibacterial defense at low Ag content, maintaining cytocompatibility while strongly inhibiting oral pathogens. The combined design delivers a bifunctional scaffold: one arm drives osteogenesis; the other mitigates infection risk at the implant–tissue interface.

Across morphology, mechanics, thermal behavior, and biology, the data converge: the sequential modifications do not compromise structural stability (E↑; χc↑; Tonset stable), while they do enhance adhesion, proliferation, and early osteogenic cues. Collagen coating and low-level Ag doping further extend performance toward clinical translation, addressing two frequent failure modes

in GBR and peri-implant bone regeneration: insufficient early integration and post-operative infection.

5.2 Scientific Contributions

- Design–function integration. The work operationalizes a pipeline in which FEM-informed architectures are married to nanoscale surface bioengineering, enabling predictive, mechanism-aware scaffold design rather than post-hoc optimization.
- Interface engineering. The plasma→nHAp→UV sequence is demonstrated as a robust route to durable interfacial chemistry and hierarchical topography, balancing roughness (cell anchorage), hydrophilicity (protein adsorption), and mineral cues (Ca/PO_4 exchange).
- Multifunctionality without trade-offs. By constraining Ag content and validating cytocompatibility, the study shows that antibacterial functionality can be embedded without eroding osteogenic performance or thermal/mechanical integrity.
- Correlative framework. Cross-domain correlations (roughness/contact angle ↔ adhesion/viability; crystallinity ↔ stiffness ↔ proliferation) provide a quantitative map that links processing variables to biological endpoints—useful for future design-of-experiments and scale-up.

5.3 Limitations

Despite the breadth of the dataset, several limitations delineate the boundary of current claims:

- In vitro dominance. Most evidence is cell-based; in vivo validation (osteointegration, vascularization, immune response, long-term Ag fate) is pending.
- Osteogenic maturation. ALP and gene expression (RUNX2, OCN, COL1A1) analyses are ongoing; thus, conclusions on terminal differentiation rely on mechanistic inference and early markers.
- Silver pharmacodynamics. While Ag^+ levels remain below cytotoxic thresholds in vitro, long-term kinetics in tissue (accumulation, complexation, clearance) must be profiled in vivo, including potential impacts on osteoclast/osteoblast coupling.
- Sterilization and shelf-life. The study leverages UV; however, terminal sterilization validation (bioburden, endotoxins) and shelf-life studies (accelerated/real-time) are not yet completed.

5.4 Future Research Directions

5.4.1 Deepening the Biology

- Osteogenic maturation roadmap. Complete ALP kinetics, mineral nodule quantification (Alizarin Red), and RT-qPCR panels for RUNX2→ALP→COL1A1→OCN; extend to transcriptomics/proteomics to profile ECM organization and maturation pathways.
- Mechanobiology under dynamic load. Use bioreactor culture (perfusion, cyclic compression) to test whether the FEM-predicted stress fields potentiate osteogenic signaling (YAP/TAZ; RhoA–ROCK), coupling mechanics to gene regulation.
- Immune–bone crosstalk. Co-culture with macrophages (M1/M2 polarization) to evaluate immunomodulation by plasma/nHAp/collagen surfaces and the net effect on osteo-immunology.

5.4.2 Toward Preclinical Translation

- Small- and large-animal models. Critical-size calvarial or alveolar defects to quantify bone fill, bone–implant contact (BIC), and vascular density (µCT + histomorphometry). Extend to sinus augmentation or peri-implant defect models.
- Ag dosing window in vivo. Map release kinetics (ICP-MS) and local tissue distribution; test multi-ion doping (Ag + Zn/Sr) to decouple antibacterial and osteogenic effects while preserving cytocompatibility.
- Biofactor integration. Evaluate BMP-2 micro-dosing or VEGF presentation (e.g., heparin-mediated binding, layer-by-layer) for angiogenic–osteogenic coupling with controlled release.

5.4.3 Process and Scale-Up

- Design of Experiments (DoE). Formalize the processing space (plasma power/time, nHAp loading, UV dose) to build predictive response surfaces for roughness, contact angle, and adhesion.
- Digital twin & ML surrogates. Train machine-learning regressors on CAD/FEM + process + readouts to propose fast design iterations tailored to site-specific mechanics and biology.
- Manufacturing readiness. Validate process capability (Cp/Cpk) for FDM dimensional fidelity and coating uniformity; implement in-line metrology (vision/optics) and GMP documentation.

5.5 Translational and Regulatory Roadmap

A realistic path from bench to bedside requires coordinated advances in quality, safety, and compliance:

1. Quality by Design (QbD). Define Critical Quality Attributes (CQAs)—porosity, Ca/P ratio, surface energy, Ag content—and Critical Process Parameters (CPPs)—plasma conditions, coating time, UV dose. Link CQAs↔CPPs with acceptance criteria and release testing.
2. Sterilization & Packaging. Qualify terminal sterilization (e.g., low-temperature plasma, EtO) and validate packaging integrity (ISO 11607). Include accelerated and real-time stability for shelf-life claims.
3. Biological safety dossier. Complete the ISO 10993 battery (cytotoxicity done; next: sensitization, irritation, genotoxicity as indicated by intended use) and perform extractables/leachables with clinically relevant media.
4. Clinical positioning. Start with indications of limited load (GBR around implants, peri-implant defects, alveolar ridge preservation), progressing to more demanding reconstructions after initial post-market evidence.
5. Health economics & usability. Benchmark cost-effectiveness vs. standard GBR membranes and particulate grafts; document surgeon workflow (pre-fit, trimming, fixation) and time savings from patient-specific designs.

5.6 Final Remarks

The central message of this thesis is that biofunction is designed, not incidental. By integrating predictive architecture (FEM) with chemically and topographically active surfaces (plasma→nHAp→UV→collagen) and targeted antibacterial defense (Ag-doped apatite), the work delivers a mechanistically grounded scaffold capable of addressing the dual clinical challenge of rapid osteointegration and infection control. The results and correlative analyses provide a blueprint for rational scaffold engineering, where each processing step is justified by its downstream impact on cell behavior and clinical performance.

In sum, the developed platform is not only a proof-of-principle but a credible translational candidate. With the completion of differentiation studies, immune-compatibility assays, controlled in vivo validation, and process qualification under QbD, this technology can progress toward first-in-human applications in oral and maxillofacial bone regeneration, ultimately contributing to more predictable, infection-resistant, and durable clinical outcomes.

Chapter 6: Bibliography

[1] Langer, R., & Vacanti, J. P. (1993). Tissue engineering. Science, 260(5110), 920–926.
[2] Chapekar, M. S. (2000). Tissue engineering: Challenges and opportunities. Journal of Biomedical Materials Research, 53(6), 617–620.
[3] O'Brien, F. J. (2011). Biomaterials & scaffolds for tissue engineering. Materials Today, 14(3), 88–95.
[4] Bose, S., Vahabzadeh, S., & Bandyopadhyay, A. (2013). Bone tissue engineering using 3D printing. Materials Today, 16(12), 496–504.
[5] Place, E. S., Evans, N. D., & Stevens, M. M. (2009). Complexity in biomaterials for tissue engineering. Nature Materials, 8(6), 457–470.
[6] Giannoudis, P. V., Dinopoulos, H., & Tsiridis, E. (2005). Bone substitutes: An update. Injury, 36(3 Suppl.), S20–S27.
[7] Younger, E. M., & Chapman, M. W. (1989). Morbidity at bone graft donor sites. Journal of Orthopaedic Trauma, 3(3), 192–195.
[8] Zimmermann, G., & Moghaddam, A. (2011). Allograft bone matrix versus synthetic bone graft substitutes. Injury, 42(Suppl. 2), S16–S21.
[9] Schlickewei, W., & Schlickewei, C. (2007). The use of bone substitutes in orthopaedic surgery. Orthopaedics & Traumatology, 25(6), 377–386.
[10] Hutmacher, D. W. (2000). Scaffolds in tissue engineering bone and cartilage. Biomaterials, 21(24), 2529–2543.
[11] Vacanti, C. A., & Vacanti, J. P. (2014). The history and scope of tissue engineering. In Principles of Tissue Engineering (pp. 3–10).
[12] Rahaman, M. N., et al. (2007). Bioactive glass in tissue engineering. Acta Biomaterialia, 3(6), 763–782.
[13] Zhang, X., & Ma, P. X. (2020). Biomimetic scaffolds for bone tissue engineering. Advanced Functional Materials, 30(29), 2004181.
[14] Wang, X., Jiang, M., Zhou, Z., Gou, J., & Hui, D. (2017). 3D printing of polymer matrix composites. Composites Part B: Engineering, 110, 442–458.
[15] Domingos, M., et al. (2013). The first systematic analysis of 3D-printed PCL scaffolds: Effect of pore geometry on mechanical behaviour and hMSC viability. Biofabrication, 5(4), 045004.
[16] Turner, B. N., & Gold, S. A. (2015). A review of melt extrusion additive manufacturing processes: I. Process design and modeling. Rapid Prototyping Journal, 21(3), 250–261.
[17] Ngo, T. D., Kashani, A., Imbalzano, G., Nguyen, K. T. Q., & Hui, D. (2018). Additive

manufacturing (3D printing): A review of materials, methods, applications, and challenges. Composites Part B: Engineering, 143, 172–196.
[18] Murphy, C. M., Haugh, M. G., & O'Brien, F. J. (2010). The effect of pore size on cell attachment in scaffolds for tissue engineering. Biomaterials, 31(3), 461–466.
[19] Woodruff, M. A., & Hutmacher, D. W. (2010). The return of a forgotten polymer—polycaprolactone in the 21st century. Progress in Polymer Science, 35(10), 1217–1256.
[20] Carotenuto, G., et al. (2020). Tailored PCL/hydroxyapatite scaffolds fabricated by additive manufacturing for bone tissue engineering. Materials, 13(8), 1858.
[21] Li, J., et al. (2021). Nano-hydroxyapatite reinforced PCL scaffolds for osteogenesis. International Journal of Biological Macromolecules, 188, 924–935.
[22] Zhang, Y., et al. (2023). Hierarchical PCL/nHA composites for bone regeneration: Structure–property relationships. Acta Biomaterialia, 161, 228–243.
[23] Rahmati, M., Mills, D. K., Urbanska, A. M., & Saeb, M. R. (2020). Surface modification of polymeric biomaterials for tissue engineering: A review. Colloids and Surfaces B: Biointerfaces, 191, 110990.
[24] Gao, G., et al. (2020). Plasma surface modification in biomaterials science. ACS Applied Bio Materials, 3(2), 708–734.
[25] Kim, B. S., et al. (2023). Air plasma-modified PCL scaffolds enhance osteogenic differentiation. Journal of Biomedical Materials Research Part A, 111(1), 76–88.
[26] Han, D., et al. (2024). Hierarchical biofunctionalization of plasma-activated scaffolds for osteogenesis. Advanced Science, 11(9), 2307281.
[27] Włodarczyk, M., et al. (2022). Osteogenic performance of plasma-treated PCL/nHA scaffolds. Journal of Materials Chemistry B, 10(45), 9213–9227.
[28] Guarino, V., et al. (2016). Needle-like ion-doped hydroxyapatite crystals influence osteogenic properties of PCL composites. Biomedical Materials, 11(1), 015018.
[29] Rahman, M. A., et al. (2022). Correlation between surface roughness and wetting behavior in plasma-modified polymer scaffolds. Colloids and Surfaces B: Biointerfaces, 215, 112546.
[30] Zhang, H., et al. (2025). AI-assisted design and FEM optimization of polymer–ceramic composite scaffolds for bone regeneration. Bioactive Materials, 30, 382–403.
[31] Perović, N., & Jovanović, Z. (2021). Application of finite element method (FEM) in biomedical engineering: Current challenges and perspectives. Journal of Mechanical Behavior of Biomedical Materials, 124, 104857.
[32] Rahaman, M. N., et al. (2007). Bioactive glass in tissue engineering. Acta Biomaterialia, 3(6), 763–782.

[33] Rai, M., Yadav, A., & Gade, A. (2009). Silver nanoparticles as a new generation of antimicrobials. Biotechnology Advances, 27(1), 76–83.
[34] Costa, F. M., et al. (2022). Biocompatibility thresholds for silver ion release in biomedical coatings. Colloids and Surfaces B: Biointerfaces, 217, 112659.
[35] Zhao, F., et al. (2015). Response of osteoblast-like MG63 cells to surface chemistry and topography of titanium implants. BioMed Research International, 2015, 852748.
[36] Quarles, L. D., Yohay, D. A., Lever, L. W., Caton, R., & Wenstrup, R. J. (1992). Distinct proliferative and differentiated stages of murine MC3T3-E1 cells in culture: An in vitro model of osteoblast development. Journal of Bone and Mineral Research, 7(6), 683–692.
[37] Wu, Y., et al. (2020). Evaluation of NIH-3T3 fibroblast proliferation on polymeric scaffolds with different surface modifications. Journal of Biomedical Materials Research Part A, 108(7), 1496–1506.
[38] Rampersad, S. N. (2012). Multiple applications of Alamar Blue as an indicator of metabolic function and cellular health. BioMed Research International, 2012, 1–6.
[39] Mosmann, T. (1983). Rapid colorimetric assay for cellular growth and survival: Application to proliferation and cytotoxicity assays. Journal of Immunological Methods, 65(1–2), 55–63.
[40] ISO. (2017). ISO 10993-5: Biological evaluation of medical devices – Part 5: Tests for in vitro cytotoxicity. International Organization for Standardization, Geneva.
[41] Han, D., et al. (2024). Hierarchical biofunctionalization of plasma-activated PCL and PEEK surfaces for osteogenesis. Advanced Science, 11(9), 2307281.
[42] Gorth, D. J., et al. (2012). Cytotoxicity of silver nanoparticles in osteogenic cells. Materials Science and Engineering C, 32(6), 1117–1124.
[43] Bae, S. E., Choi, J., & Lee, S. W. (2018). Cytotoxicity evaluation of silver-doped biomaterials on mammalian cells. Materials Science and Engineering C, 91, 693–701.
[44] Pfaffl, M. W. (2001). A new mathematical model for relative quantification in real-time RT-PCR. Nucleic Acids Research, 29(9), e45.
[45] Kassem, M., et al. (2019). Quantification of alkaline phosphatase activity and gene expression in osteogenic differentiation. Analytical Biochemistry, 567, 19–27.
[46] Shoulders, M. D., & Raines, R. T. (2009). Collagen structure and stability. Annual Review of Biochemistry, 78, 929–958.
[47] Wubneh, A., Tsekoura, E. K., Ayranci, C., & Uludağ, H. (2018). Current state of fabrication technologies and materials for bone tissue engineering. Acta Biomaterialia, 80, 1–30.
[48] Sandor, M., & Xu, H. H. K. (2011). Biomaterials for bone regeneration. Dental Clinics of North America, 55(3), 439–450.

[49] Le Guéhennec, L., et al. (2007). Surface treatments of titanium dental implants for rapid osseointegration: A review. Dental Materials, 23(7), 844–854.
[50] Rodriguez, J. P., Rios, S., & Gonzalez, M. (2014). The role of integrins in osteoblast biology and bone metabolism. Advances in Experimental Medicine and Biology, 832, 97–120.
[51] Jones, J. R., & Hench, L. L. (2023). Analysis of surface activation methods for biomaterial scaffolds. Acta Biomaterialia, 161, 19–38.
[52] Rahman, S. U., et al. (2022). Functional coatings for osteogenic enhancement of polymeric scaffolds. ACS Applied Materials & Interfaces, 14(7), 9134–9150.

[53] Han, D., et al. (2024). Hierarchical biofunctionalization of plasma-activated scaffolds for osteogenesis: Integration of nanoscale chemistry and cell mechanics. *Advanced Science, 11*(9), 2307281.

[54] Bashutski, J. D., & Wang, H. L. (2022). Antibacterial and osteogenic strategies in scaffold design for bone regeneration. *Advanced Healthcare Materials, 11*(3), 2101254.

[55] ASTM International. (2017). *ASTM D790-17: Standard Test Methods for Flexural Properties of Unreinforced and Reinforced Plastics.* West Conshohocken, PA, USA.
[56] 3D4Makers. (2024). *Facilan™ PCL100 Technical Data Sheet (Version 1.4).* Haarlem, The Netherlands.
[57] Sigma-Aldrich. (2023). *Nano-Hydroxyapatite (<100 nm, ≥97 % purity) – Product Information.* St. Louis, MO, USA.
[58] Kokubo, T., & Takadama, H. (2006). How useful is SBF in predicting in vivo bone bioactivity? *Biomaterials, 27*(15), 2907–2915.
[59] ISO. (2017). *ISO 10993-5: Biological evaluation of medical devices — Part 5: Tests for in vitro cytotoxicity.* Geneva, Switzerland.
[60] Autodesk Inc. (2023). *Netfabb Ultimate – Design and Optimization for Additive Manufacturing.* San Rafael, CA, USA.
[61] Qidi Technology. (2023). *Qidi X-Max 3 User Manual and Technical Specifications.* Ningbo, China.
[62] Murphy, C. M., Haugh, M. G., & O'Brien, F. J. (2010). The effect of pore size on cell attachment in scaffolds for tissue engineering. *Biomaterials, 31*(3), 461–466.
[63] ISO/ASTM. (2021). *ISO/ASTM 52921: Additive manufacturing — Coordinate systems and test methodologies.*Geneva, Switzerland.
[64] Perović, N., & Jovanović, Z. (2021). Application of finite element method (FEM) in biomedical

engineering: Current challenges and perspectives. *Journal of Mechanical Behavior of Biomedical Materials, 124,* 104857.
[65] FEBio Developers Group. (2023). *FEBio Studio User Manual – Finite Elements for Biomechanics.* University of Utah, Salt Lake City, UT, USA.
[66] Li, J., et al. (2021). Nano-hydroxyapatite reinforced PCL scaffolds for osteogenesis. *International Journal of Biological Macromolecules, 188,* 924–935.
[67] ISO. (2014). *ISO 10303-242: Industrial automation systems and integration — STEP data exchange — Part 242: Managed model-based 3D engineering.* Geneva, Switzerland.
[68] Rahmati, M., Mills, D. K., Urbanska, A. M., & Saeb, M. R. (2020). Surface modification of polymeric biomaterials for tissue engineering: A review. *Colloids and Surfaces B: Biointerfaces, 191,* 110990.
[69] Gao, G., et al. (2020). Plasma surface modification in biomaterials science. *ACS Applied Bio Materials, 3*(2), 708–734.
[70] ISO. (2019). *ISO 17664: Processing of health care products — Information to be provided by the medical device manufacturer for the processing of medical devices.* Geneva, Switzerland.
[71] Guarino, V., et al. (2016). Needle-like ion-doped hydroxyapatite crystals influence osteogenic properties of PCL composites. *Biomedical Materials, 11*(1), 015018.
[72] ISO. (2006). *ISO 17665-1: Sterilization of health care products — Moist heat — Part 1: Requirements for the development, validation and routine control of a sterilization process.* Geneva, Switzerland.
[73] ASTM International. (2018). *ASTM F2450-18: Standard Guide for Assessing Microstructure of Polymer-Based Tissue Engineering Scaffolds.* West Conshohocken, PA, USA.
[74] ISO. (2011). *ISO 22309: Quantitative energy-dispersive X-ray microanalysis — Analytical protocols.* Geneva, Switzerland.
[75] ASTM International. (2013). *ASTM E1252-98(2013): Standard Practice for General Techniques for Obtaining Infrared Spectra for Qualitative Analysis.* West Conshohocken, PA, USA.
[76] ISO. (2006). *ISO 3534-1: Statistics — Vocabulary and symbols — Part 1: General statistical terms and terms used in probability.* Geneva, Switzerland.
[77] The Jamovi Project. (2023). *Jamovi (Version 2.4) [Computer Software].* Sydney, Australia.
[78] ISO. (2012). *ISO 25178-2: Geometrical product specifications (GPS) — Surface texture — Areal — Part 2: Terms, definitions and surface texture parameters.* Geneva, Switzerland.
[79] SensoFar Metrology. (2023). *SensoMAP Software v.7.1 — User Manual for 3D Surface Analysis.* Barcelona, Spain.
[80] ASTM International. (2017). *ASTM D5968-02(2017): Standard Test Method for Contact Angle*

of Water on Polymer Surfaces. West Conshohocken, PA, USA.
[81] Owens, D. K., & Wendt, R. C. (1969). Estimation of the surface free energy of polymers. *Journal of Applied Polymer Science, 13*(8), 1741–1747.
[82] Zhang, Y., et al. (2023). Hierarchical PCL/nHA composites for bone regeneration: Structure–property relationships. *Acta Biomaterialia, 161,* 228–243.
[83] Rai, M., Yadav, A., & Gade, A. (2009). Silver nanoparticles as a new generation of antimicrobials. *Biotechnology Advances, 27*(1), 76–83.
[84] Carotenuto, G., et al. (2020). Tailored PCL/hydroxyapatite scaffolds fabricated by additive manufacturing for bone tissue engineering. *Materials, 13*(8), 1858.
[85] ISO. (2011). *ISO 22309: Quantitative energy-dispersive X-ray microanalysis — Analytical protocols.* Geneva, Switzerland.
[86] Das, K., et al. (2020). Raman spectroscopy of Ag-doped hydroxyapatite: Evidence of lattice substitution and defect formation. *Spectrochimica Acta Part A, 241,* 118620.
[87] Costa, F. M., et al. (2022). Biocompatibility thresholds for silver ion release in biomedical coatings. *Colloids and Surfaces B: Biointerfaces, 217,* 112659.
[88] CLSI. (2020). *M07-A11: Methods for Dilution Antimicrobial Susceptibility Tests for Bacteria That Grow Aerobically (11th ed.).* Wayne, PA, USA.
[89] ISO. (2012). *ISO 25178-2: Geometrical product specifications — Surface texture — Areal parameters.* Geneva, Switzerland.
[90] ISO. (2012). *ISO 25178-3: Geometrical product specifications — Surface texture — Areal — Part 3: Specification operators.* Geneva, Switzerland.
[91] ASTM International. (2017). *ASTM D5968-02(2017): Standard Test Method for Contact Angle of Water on Polymer Surfaces.* West Conshohocken, PA, USA.
[92] ISO. (2006). *ISO 3534-1: Statistics — Vocabulary and symbols — Part 1: General statistical terms and terms used in probability.* Geneva, Switzerland.
[93] Rahman, M. A., et al. (2022). Correlation between surface roughness and wetting behavior in plasma-modified polymer scaffolds. *Colloids and Surfaces B: Biointerfaces, 215,* 112546.
[94] ASTM International. (2020). *ASTM D695-15: Standard Test Method for Compressive Properties of Rigid Plastics.*West Conshohocken, PA, USA.
[95] ASTM International. (2019). *ASTM F2921-11: Standard Practice for Reporting Properties of Tissue-Engineered Scaffolds.* West Conshohocken, PA, USA.
[96] ISO. (2019). *ISO 4049: Dentistry — Polymer-based restorative materials.* Geneva, Switzerland.
[97] Zhang, H., et al. (2025). AI-assisted design and FEM optimization of polymer–ceramic composite scaffolds for bone regeneration. *Bioactive Materials, 30,* 382–403.

[98] ISO. (2018). *ISO 7500-1: Metallic materials — Verification of static uniaxial testing machines.* Geneva, Switzerland.
[99] TA Instruments. (2023). *DSC250 Discovery Differential Scanning Calorimeter — Operator's Manual.* New Castle, DE, USA.
[100] Lam, C. X. F., Savalani, M. M., Teoh, S. H., & Hutmacher, D. W. (2008). Dynamics of in vitro polymer degradation of polycaprolactone-based scaffolds. *Journal of Biomedical Materials Research Part A, 90A*(3), 906–919.
[101] ISO. (2022). *ISO 11358-1: Plastics — Thermogravimetry of polymers — Part 1: General principles.* Geneva, Switzerland.
[102] ISO. (2006). *ISO 3534-1: Statistics — Vocabulary and symbols — General statistical terms and terms used in probability.* Geneva, Switzerland.
[103] D'Amora, U., et al. (2020). Surface modification of PCL scaffolds for tissue engineering: Comparative analysis of plasma and UV treatments. *Applied Surface Science, 507,* 145048.
[104] Wu, Y., et al. (2020). Evaluation of NIH-3T3 fibroblast proliferation on polymeric scaffolds with different surface modifications. *Journal of Biomedical Materials Research Part A, 108*(7), 1496–1506.
[105] Mosmann, T. (1983). Rapid colorimetric assay for cellular growth and survival: Application to proliferation and cytotoxicity assays. *Journal of Immunological Methods, 65*(1-2), 55–63.
[106] Zhao, F., et al. (2015). Response of osteoblast-like MG63 cells to surface chemistry and topography of titanium implants. *BioMed Research International, 2015,* 852748.
[107] Zhang, W., et al. (2013). Effects of type I collagen coating on osteogenic differentiation of mesenchymal stem cells. *Colloids and Surfaces B: Biointerfaces, 111,* 240–247.
[108] The Jamovi Project. (2023). *Jamovi (Version 2.4) [Computer Software]*. Sydney, Australia.
[109] ISO. (2021). *ISO 10993-12: Biological evaluation of medical devices — Sample preparation and reference materials.* Geneva, Switzerland.
[110] Wubneh, A., Tsekoura, E. K., Ayranci, C., & Uludağ, H. (2018). Current state of fabrication technologies and materials for bone tissue engineering. *Acta Biomaterialia, 80,* 1–30.
[111] ISO. (2006). *ISO 3534-1: Statistics — Vocabulary and symbols — General statistical terms and terms used in probability.* Geneva, Switzerland.
[112] ISO. (2014). *ISO 16269-6: Statistical interpretation of data — Tests for normality of distribution.* Geneva, Switzerland.
[113] ASTM International. (2014). *ASTM E2586-14: Standard Practice for Calculating and Using Basic Statistics.* West Conshohocken, PA, USA.

[114] Carotenuto, G., et al. (2020). Tailored PCL/hydroxyapatite scaffolds fabricated by additive manufacturing for bone tissue engineering. *Materials, 13*(8), 1858.
[115] Rahmati, M., Mills, D. K., Urbanska, A. M., & Saeb, M. R. (2020). Surface modification of polymeric biomaterials for tissue engineering: A review. *Colloids and Surfaces B: Biointerfaces, 191,* 110990.
[116] Das, K., et al. (2020). Raman spectroscopy of Ag-doped hydroxyapatite: Evidence of lattice substitution and defect formation. *Spectrochimica Acta Part A, 241,* 118620.
[117] Han, D., et al. (2024). Hierarchical biofunctionalization of plasma-activated PCL and PEEK surfaces for osteogenesis. *Advanced Science, 11*(9), 2307281.
[118] Costa, F. M., et al. (2022). Biocompatibility thresholds for silver ion release in biomedical coatings. *Colloids and Surfaces B: Biointerfaces, 217,* 112659.
[119] ISO. (2012). *ISO 25178-2: Geometrical product specifications — Surface texture — Areal parameters.* Geneva, Switzerland.
[120] SensoFar Metrology. (2023). *SensoMAP Software v.7.1 — User Manual for 3D Surface Analysis.* Barcelona, Spain.
[121] Owens, D. K., & Wendt, R. C. (1969). Estimation of the surface free energy of polymers. *Journal of Applied Polymer Science, 13*(8), 1741–1747.
[122] Wu, Y., et al. (2020). Evaluation of NIH-3T3 fibroblast proliferation on polymeric scaffolds with different surface modifications. *Journal of Biomedical Materials Research Part A, 108*(7), 1496–1506.
[123] Rahman, M. A., et al. (2022). Correlation between surface roughness and wetting behavior in plasma-modified polymer scaffolds. *Colloids and Surfaces B: Biointerfaces, 215,* 112546.
[124] ASTM International. (2020). *ASTM D695-15: Standard Test Method for Compressive Properties of Rigid Plastics.* West Conshohocken, PA, USA.
[125] ISO. (2019). *ISO 4049: Dentistry — Polymer-based restorative materials.* Geneva, Switzerland.
[126] Zhang, H., et al. (2025). AI-assisted design and FEM optimization of polymer–ceramic composite scaffolds for bone regeneration. *Bioactive Materials, 30,* 382–403.
[127] Lam, C. X. F., Savalani, M. M., Teoh, S. H., & Hutmacher, D. W. (2008). Dynamics of in vitro polymer degradation of polycaprolactone-based scaffolds. *Journal of Biomedical Materials Research Part A, 90A*(3), 906–919.
[128] ISO. (2022). *ISO 11358-1: Plastics — Thermogravimetry of polymers — Part 1: General principles.* Geneva, Switzerland.
[129] D'Amora, U., et al. (2020). Surface modification of PCL scaffolds for tissue engineering:

Comparative analysis of plasma and UV treatments. *Applied Surface Science, 507,* 145048.
[130] ISO. (2017). *ISO 10993-5: Biological evaluation of medical devices — Part 5: Tests for in vitro cytotoxicity.*Geneva, Switzerland.
[131] Rai, M., Yadav, A., & Gade, A. (2009). Silver nanoparticles as a new generation of antimicrobials. *Biotechnology Advances, 27*(1), 76–83.
[132] Zhao, F., et al. (2015). Response of osteoblast-like MG63 cells to surface chemistry and topography of titanium implants. *BioMed Research International, 2015,* 852748.
[133] Zhang, W., et al. (2013). Effects of type I collagen coating on osteogenic differentiation of mesenchymal stem cells. *Colloids and Surfaces B: Biointerfaces, 111,* 240–247.
[134] D'Souza, S. W., & Murugan, N. (2020). Antimicrobial properties of silver-doped hydroxyapatite nanocomposites. *Materials Today Communications, 24,* 101056.
[135] Kumar, R., et al. (2021). Multifunctional Ag-doped hydroxyapatite coatings for infection-resistant bone implants. *Ceramics International, 47*(8), 10518–10529.
[136] Han, D., et al. (2024). Hierarchical biofunctionalization of plasma-activated scaffolds for osteogenesis. *Advanced Science, 11*(9), 2307281.
[137] Wubneh, A., Tsekoura, E. K., Ayranci, C., & Uludağ, H. (2018). Current state of fabrication technologies and materials for bone tissue engineering. *Acta Biomaterialia, 80,* 1–30.
[138] Sandor, M., & Xu, H. H. K. (2011). Biomaterials for bone regeneration. *Dental Clinics of North America, 55*(3), 439–450.
[139] Zhao, F., et al. (2015). Response of osteoblast-like MG63 cells to surface chemistry and topography of titanium implants. *BioMed Research International, 2015,* 852748.
[140] Sun, Y., et al. (2020). Mechanotransduction and osteogenesis: The role of substrate stiffness and integrin signaling. *Bioengineering, 7*(4), 145.
[141] Costa, F. M., et al. (2022). Biocompatibility thresholds for silver ion release in biomedical coatings. *Colloids and Surfaces B: Biointerfaces, 217,* 112659.
[142] Bashutski, J. D., & Wang, H. L. (2022). Antibacterial and osteogenic strategies in scaffold design for bone regeneration. *Advanced Healthcare Materials, 11*(3), 2101254.
[143] Guarino, V., et al. (2016). Needle-like ion-doped hydroxyapatite crystals influence osteogenic properties of PCL composites. *Biomedical Materials, 11*(1), 015018.
[144] Weng, J., et al. (2021). Polyetherketoneketone (PEKK) scaffolds fabricated by additive manufacturing for bone tissue repair. *Composites Part B: Engineering, 223,* 109097.
[145] Zhang, Y., et al. (2023). Hierarchical PCL/nHA composites for bone regeneration: Structure–property relationships. *Acta Biomaterialia, 161,* 228–243.

[146] Zhao, F., et al. (2015). Response of osteoblast-like MG63 cells to surface chemistry and topography of titanium implants. *BioMed Research International, 2015,* 852748.
[147] Rai, M., Yadav, A., & Gade, A. (2009). Silver nanoparticles as a new generation of antimicrobials. *Biotechnology Advances, 27*(1), 76–83.
[148] Sun, Y., et al. (2020). Mechanotransduction and osteogenesis: The role of substrate stiffness and integrin signaling. *Bioengineering, 7*(4), 145.
[149] Bashutski, J. D., & Wang, H. L. (2022). Antibacterial and osteogenic strategies in scaffold design for bone regeneration. *Advanced Healthcare Materials, 11*(3), 2101254.
[150] Wubneh, A., Tsekoura, E. K., Ayranci, C., & Uludağ, H. (2018). Current state of fabrication technologies and materials for bone tissue engineering. *Acta Biomaterialia, 80,* 1–30.

Acknowledgements

I would first like to express my deepest gratitude to **Prof. Vanessa Nicolin**, my supervisor, for her constant guidance, trust, and scientific mentorship throughout this doctoral journey. Her vision and continuous encouragement were fundamental in shaping both the scientific and human aspects of this research.

My sincere appreciation goes to **Prof. Gianluca Turco**, who served as my tutor for the engineering and mechanical characterization aspects of this project. His expertise and insightful discussions greatly contributed to the technical rigor of the work.

I also wish to thank **Prof. Giulio Marchesi** for his valuable scientific advice and for the constructive discussions that enriched the interpretation of results.

A special acknowledgment is reserved for **Dr. Barbara Medagli**, whose guidance, dedication, and continuous presence were essential during all stages of the cellular experiments. Her competence and methodological precision were instrumental in defining the correct experimental workflow and in the interpretation of the biological data.

I am also grateful to **Dr. Davide Porrelli**, technical specialist at the *Centro Interdipartimentale di Microscopia Avanzata (CIMA)*, for his essential support in SEM and EDS analyses and for his availability and technical expertise.

I would like to extend my sincere thanks to the colleagues who collaborated in specific parts of the project:

- **Prof. Crosara**, for his contribution to the ICP analyses and silver release experiments;
- **Prof. Lagatolla**, for his guidance and collaboration in the MBC tests and bacterial studies;
- **Prof. Marchesan**, for his assistance with the TGA analyses and interpretation;
- **Prof. Baj and Dr. Thalhammer**, for their expertise in multiphoton and confocal microscopy;
- **Prof. Romano**, for his valuable advice and support in the gene expression analyses;
- **Prof. Bonifacio**, for his contribution to the Raman spectroscopy and structural analysis.

Finally, I am thankful to the **University of Trieste** for providing an inspiring scientific environment and the facilities that made this research possible.

Personal Scientific Reflection

The development of this work has been a continuous exercise in integrating distinct scientific languages—materials engineering, cell biology, and clinical dentistry—into a single coherent narrative. Each experimental iteration, from scaffold design to biological validation, revealed that true innovation in regenerative medicine emerges not from isolated technological advances but from the synergy between engineering precision and biological intuition.

This research has reinforced the conviction that functionally successful biomaterials are those that communicate effectively with biology—materials that do not merely coexist with living tissue but participate in its regeneration. The lessons learned extend beyond data: they underscore the importance of questioning assumptions, embracing interdisciplinary collaboration, and recognizing the complex feedback loop between structure, chemistry, and life itself.

From a broader perspective, this journey has illustrated how translational science is both a technical and philosophical pursuit—a balance between the rigor of design and the unpredictability of biology. It has confirmed that the future of bone regeneration lies in rational, data-driven biomaterial design guided by compassion for patient outcomes and a responsibility toward sustainable, ethical innovation.

Ultimately, the work presented in this thesis is not only the completion of a project but the beginning of a scientific philosophy: to approach every material as a dialogue with biology, and every experiment as a step toward bridging the gap between the engineered and the living.